Spring 2002

Physical and chemical characterization of single atmospheric aerosols: Laboratory studies of interactions of acidic trace gases with sea -salt aerosols, and, Development efforts for an aerosol charging system using a corona discharge

Matthew Brigham Loomis
University of New Hampshire, Durham

INFORMATION TO USERS

This manuscript has been reproduced from the microfilm master. UMI films the text directly from the original or copy submitted. Thus, some thesis and dissertation copies are in typewriter face, while others may be from any type of computer printer.

The quality of this reproduction is dependent upon the quality of the copy submitted. Broken or indistinct print, colored or poor quality illustrations and photographs, print bleedthrough, substandard margins, and improper alignment can adversely affect reproduction.

In the unlikely event that the author did not send UMI a complete manuscript and there are missing pages, these will be noted. Also, if unauthorized copyright material had to be removed, a note will indicate the deletion.

Oversize materials (e.g., maps, drawings, charts) are reproduced by sectioning the original, beginning at the upper left-hand corner and continuing from left to right in equal sections with small overlaps.

Photographs included in the original manuscript have been reproduced xerographically in this copy. Higher quality 6" x 9" black and white photographic prints are available for any photographs or illustrations appearing in this copy for an additional charge. Contact UMI directly to order.

Bell & Howell Information and Learning
300 North Zeeb Road, Ann Arbor, MI 48106-1346 USA
800-521-0600

UMI®

PHYSICAL AND CHEMICAL CHARACTERIZATION OF SINGLE ATMOSPHERIC AEROSOLS: LABORATORY STUDIES OF INTERACTIONS OF ACIDIC TRACE GASES WITH SEA-SALT AEROSOLS

AND

DEVELOPMENT EFFORTS FOR AN AEROSOL CHARGING SYSTEM USING A CORONA DISCHARGE

By

Matthew B. Loomis
BS Physics, University of New Hampshire 1991
MS Physics, University of New Hampshire 1994

DISSERTATION

Submitted to the University of New Hampshire
In Partial Fulfillment of
The Requirements for the Degree of

Doctor of Philosophy
In
Earth Sciences

May 2002

ProQuest Information and Learning Company
300 North Zeeb Road
P.O. Box 1346
Ann Arbor, MI 48106-1346

This dissertation has been examined and approved.

Dissertation Director, Robert W. Talbot, Ph.D.
Research Professor of Earth Sciences

Karen L. Carleton, Ph.D.
Research Assistant Professor of Zoology

W. Terry Rawlins, Ph.D.
Research Scientist, Physical Sciences Inc.

Dave Bartlett, Ph.D.,
Research Professor,
Complex Systems Research Center

Jack Dibb, Ph.D.
Research Associate Professor of Earth Sciences

December 15, 2001

DEDICATION

This work is dedicated to the memory of my friends Tad and Robin.

"We tobogganed around the snow covered strip, gunning the engine to get through the turns, bumping along the taxiways with the stick full forward to keep the tail from dragging us down. Then with a surge of power from a motor that sounded like it was descended from a farm tractor, we were off and floating in the freezing air above snow covered fields and woods and lakes."

- Tad Ackman, February 1995

ACKNOWLEDGMENTS

I would like to thank the following people:

Bob Talbot for his financial support, direction, guidance and patience during the course of completing this work.

Karen Carleton for her inspiration, encouragement, advice and technical help, without which none of this would have happened.

Terry Rawlins, for his help and technical advice.

Jack Dibb for his company and advice during the SUCCESS flights and the Flytrap experiments.

Jack Mulhern for his stimulating, insightful conversations on the meaning and nature of science and for his friendship and encouragement.

Huckle, my cat, for being a loveable, fat, furry idiot.

Ken and Emily for their friendship, support and excellent cooking during the dark times.

Brett and Jennifer for opening their house and their woodshop to me when I needed it most.

Bob Lambert who taught me how to be flippant.

Tad Ackman and Robin Gorsky who taught me how to fly.

TABLE OF CONTENTS

LIST OF TABLES

LIST OF FIGURES

Figure Page

ABSTRACT

PHYSICAL AND CHEMICAL CHARACTERIZATION OF SINGLE ATMOSPHERIC AEROSOLS:
LABORATORY STUDIES OF INTERACTIONS OF ACIDIC TRACE GASES WITH SEA-SALT AEROSOLS

AND

DEVELOPMENT EFFORTS FOR AN AEROSOL CHARGING SYSTEM USING A CORONA DISCHARGE

By Matthew B. Loomis
University of New Hampshire, May 2002

There has long been an interest for *in situ* analysis of single atmospheric aerosols. To this end, the Flytrap instrument was developed under a NASA Phase I and Phase II Small Business Innovative Research Grant. The centerpiece of the instrument was a spherical void electrodynamic levitator that was used to suspend and optically characterize the physical and chemical properties of individual aerosols. Physical measurements of the aerosols were conducted with the aid of a Mie scattering system while chemical characterization was conducted with a Raman spectroscopy microprobe. A large effort focused on development of a system for charging and trapping atmospheric aerosols using a corona discharge. Testing of this charging device indicated that only aerosols larger than twenty microns in diameter could be successfully charged and trapped.

Once assembled, calibrated and tested, the Flytrap instrument was used to study the interaction between acidic trace gases and artificial sea-salt aerosols in a laboratory environment. The chamber housing the spherical void electrodynamic levitator was designed to simulate conditions found in a polluted marine boundary layer. The reactive uptake coefficient between nitric acid and sea-salt aerosols under a variety of relative humidity and alkalinity conditions was measured. The uptake coefficient varied strongly with changes in relative humidity, time and alkalinity. In addition, oxidation of sulfur dioxide to sulfate in sea-salt aerosols was studied under a variety of alkalinity conditions. It was found that these reaction rates also varied strongly with oxidant type, changes in relative humidity, time and alkalinity.

CHAPTER 1

THE FLYTRAP INSTRUMENT

1.1 Introduction

Aerosols play an important role in a wide range of chemical and physical processes, including those involved in air pollution, medicine, combustion, materials synthesis, and clean room technology. Research and development in these areas requires analytical methods that can monitor changes in aerosol particles as they grow or are transformed by condensation, evaporation or chemical reaction. This can be challenging because of the small mass and small size of the particles as well as the fact that the concentrations of minor components in the particle are often of considerable interest (Johnston and Wexler, 1995).

Particles in the atmosphere contribute to almost every air pollution problem. In the urban troposphere, aerosols have been implicated in increased morbidity and mortality. The effect is acute: increased particulate concentrations are directly correlated with increased incidence of health effects (Willeke and Baron, 1993). Aerosols are also thought to influence the global climate in two ways: by directly scattering short-wave solar radiation back into space and indirectly by changing the number density and size of cloud droplets which in turn affect the radiative properties of clouds (Charlson et al., 1987).

In addition to climate effects, aerosols can influence the chemistry and gaseous composition of the troposphere through heterogeneous chemical reactions. Aqueous aerosols have a tendency to scavenge soluble chemical species from the gas phase. Once in the aqueous phase, these scavenged species have the potential to undergo chemical reactions at rates sometimes orders of magnitude faster than in the gas phase (Chameides and Stelson, 1992).

Additionally, in the form of polar stratospheric clouds, particles are the storehouse for chlorine and nitrogen compounds that cause the austral spring ozone hole (Johnston and Wexler, 1995). Finally, aerosols contribute to the problem of acid deposition and visibility reduction over large portions of the globe.

Aerosols are created from both natural and anthropogenic sources. Wind blown dust from China and sub-Saharan Africa are one type of natural aerosol source. Other natural aerosol sources include emissions from volcanoes and wind blown sea-salt from oceans. Anthropogenic sources of aerosols include biomass burning, transportation, and industrial activities. In addition to these primary particles, secondary sources of aerosols are formed as a result of condensation, chemical reaction, and nucleation.

Atmospheric aerosols are composed of a wide variety of compounds that depend primarily on the source of the particles. Typical compound classes include crustal material, heavy metals, carbonaceous compounds, water and inorganic electrolytes. The crustal material can contain silicon dioxide and calcium salts. Heavy metals include lead, chromium, arsenic, vanadium and selenium. Carbonaceous aerosol material is composed of elemental carbon (soot) and many organic compounds that are larger than C_7. The inorganic electrolytes are usually acidic and very hygroscopic, resulting in aerosols that contain water even at very low relative humidity levels.

In order to understand the aerosol sources, environmental effects, and processing in the atmosphere, it is necessary to measure both the physics and chemistry of the collected particles. Bulk analyses can be made by collecting ambient atmospheric particles on a filter or in impactor devices that may segregate the particles by size. The bulk samples are then characterized by standard analytical techniques often hours or days after the initial collection has been conducted (Lee and Ramamurthi, 1993).

Numerous sources of error may influence the accuracy of bulk aerosol measurement techniques. Usually particle collection onto a filter must occur over an extended period of time, on the order of hours, before a sufficient sample is acquired. The result is an aerosol sample with limited temporal and spatial resolution. Additionally, the long collection time may allow particle reactions to proceed or condensation and evaporation of volatile compounds, including water, to occur on the substrate.

Particle-phase material lost by volatilization during or after collection may lead to a negative artifact. This has been well documented for the cases of NH_4NO_3, NH_4^+, Cl^- and NO_3^-. As an example, particulate samples collected on glass fiber filters are subject to enhanced loss of NH_4^+ due to filter alkalinity. In addition to negative artifacts, positive artifacts can also occur when filters are used for a bulk sample collection medium. Retention of gaseous HNO_3, SO_2 and organic C by sorption or reaction with the sampling medium and/or particulate matter on the filter can result in positive errors in determining corresponding aerosol-phase concentrations. Nitric acid is retained on many types of filters, on stages of impactors and by previously collected particles, leading to positive artifacts of particulate nitrate.

In addition to volatile chemical evaporation and condensation, chemical changes to aerosol constituents may occur both during and following collection, including neutralization of acidic species and oxidation of specific organic compounds. Collection of bulk aerosol samples usually implies that particle-to-particle variations in composition cannot be assessed (Johnston and Wexler, 1995).

Analysis of individual atmospheric particles has been performed with off-line microanalytical techniques such as electron probe microanalysis, particle-induced X-ray emission, secondary ion mass spectroscopy, and laser microprobe mass spectroscopy (Jambers et al., 1995). These methods give particle-to-particle variations in composition, but like the bulk sampling methods, are subject to poor temporal resolution, poor particle sizing capabilities, and

sampling artifacts. While the new real time capabilities of some of these techniques are a major improvement over previous techniques, quantitative interpretation of mass spectrometer patterns can be difficult. In addition most instruments detect only positive or negative ions and not both. This can limit compositional identification of negative ions that are monitored since the positive ions are not detected (Carleton et al., 1995)

The ideal method of aerosol sampling would have to analyze individual aerosols rapidly and in real time using instrumentation that is compact and robust enough for field measurements. A more versatile method for studying aerosols in situ in the atmosphere would be of great benefit in providing more accurate data for atmospheric modeling as well as data validation for satellite based global aerosol monitoring systems. To this end, over the past ten years, several groups have applied quadrupole traps to the study of single particles in the laboratory. This work has focused on measurement of particle transport properties (Davis, 1983), particle evaporation and condensation, particle light scattering (Hightower et al., 1988) and particle composition by Raman spectroscopy (Fung and Tang, 1989).

These quadrupole traps are based on the original designs of Paul and Langmuir, and can trap particles from 0.01 to 100 μm diameter. The quadrupole trap offers many intriguing possibilities for aerosol measurements. The trap acts like a wall-less container and can electrodynamicaly hold an aerosol as long as wanted. Because the particle does not contact any surfaces, contamination can be held to a minimum. While the particle is suspended several different techniques can be used concurrently to analyze the particle size, optical properties and chemical composition.

Under a Phase I and II SBIR program, a quadrupole trap similar to those used previously to suspend single aerosol was constructed at Physical Sciences Inc. (Carleton et al., 1995). The FLYTRAP instrument was conceived and developed to meet the demand for in situ, single particle analysis. It was originally developed as a field instrument for in situ characterization of

aerosols directly sampled from an aircraft or ground platform. While suspended in the trap, the particles would be probed optically to determine the particle size and chemical composition. Unfortunately all of the components of the instrument did not function as desired, namely the mechanism used to charge the aerosols before trapping. At the conclusion of the SBIR Phase II, the flytrap instrument was moved to University of New Hampshire to pursue studies of particle charging for field implementation. Aerosol charging still remains a daunting and unresolved issue. However considerable progress has been made to utilize the flytrap instrument as a laboratory platform for studying aerosol reactions. The next section describes the Flytrap instrument design, construction, calibration and final testing.

The development of this instrument was motivated by the need to measure aerosols in their natural habitat: characterizing the aerosols with minimal perturbations to their physical and chemical characteristics. In addition to characterizing aerosols with a minimum of artifacts, the Flytrap instrument will be a useful and novel method for determining properties of heterogeneous reactions. As an example, reactive uptake and mass accommodation coefficients are usually measured in the lab using thick, planar substrates (Lovejoy and Hanson, 1995) where the concentration gradients in the bulk solution may be large enough to result in a large measured uptake. The uptake in the atmosphere however, could be much slower due to a smaller concentration gradient in atmospheric particles because they are small and spherical. Therefore the coefficients measured in thick substrates in the lab may have to be modified to correctly predict reactions occurring in the atmosphere. Analysis of single suspended aerosols is an ideal way to measure uptake and mass accommodation coefficients of different gases upon condensed media found in the atmosphere. Additionally, this technique enables measurements of optical properties from real, multi-component aerosols to be made.

1.2 Flytrap Instrument Overview

Flytrap is an instrument used for aerosol optical characterization based on trapping individual aerosols in a quadrupole trap (Carleton et al., 1995). The laboratory version of the Flytrap instrument is composed of several key systems: the quadrupole trap, the Mie scattering system, the Raman spectroscopy system and several ancillary systems.

Aerosols are trapped using a spherical void electrodynamic levitator (the quadrupole trap) to confine electrically charged aerosols in a small region of space where they can be optically probed for chemical and physical characteristics. The Mie scattering system quantifies particle size and angular scattering patterns. It uses a HeNe laser to illuminate the suspended aerosol and a thermoelectrically cooled CCD camera to detect the scattered laser light. The scattering pattern is stored to disk for later analysis of particle radius. The scattered HeNe light is also detected by a TV camera zoom lens assembly to aid in particle diagnostics. The chemical composition of the suspended aerosol is obtained through the use of a Raman spectroscopy system. Ancillary systems include gas handling systems for controlling the relative humidity in the trap chamber, controlling the mixing ratio of nitric acid, ozone and sulfur dioxide to the trap chamber as well as a method for generating charged artificial aerosols. Each of these systems is described in the following sections in detail. A diagram of the optical layout of the flytrap instrument is shown in figure 1. The entire instrument is assembled on a laser table measuring 31 by 48 inches.

The flytrap instrument has proven optimal for characterizing particles in the 1 to 20 μm size range (diameter). The lower end of the size range is determined by the signal to noise ratio of the Raman spectroscopy system. The upper size range is determined by limitations of the Mie

sizing system. The details of the design of the key components on the final lab version of the instrument as well as the calibration and testing of these components are described in the sections that follow.

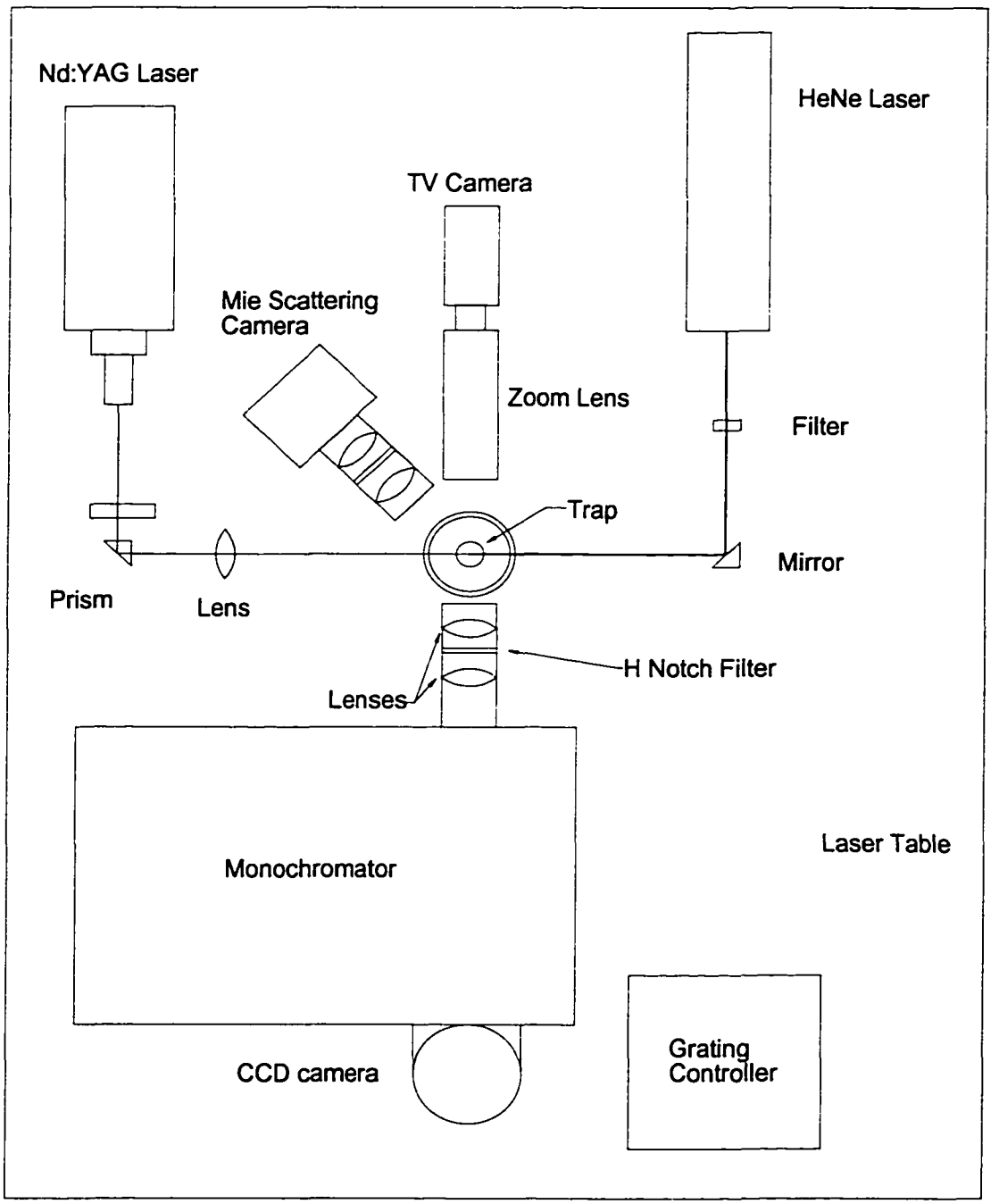

Figure 1.1: Optical access to the quadrupole trap. Only major components of the Flytrap instrument are shown.

1.3 The Quadrupole Trap

The centerpiece of the flytrap experiment is a spherical void electrodynamic levitator or "quadrupole trap". The trap consists of three electrodes: a central ring electrode, biased with an AC voltage and two endcap electrodes, biased with a DC voltage. The ring electrode, when biased with a 100 V – 1000 V AC signal, creates a saddle potential inside the spherical void of the trap such that a charged particle will be alternately confined in the axial (z) and radial (r) directions. The DC endcap electrodes provide an offset to the gravitational force on the particle. The geometry of the electrodes is shown below in figure 2. The AC ring electrode is machined in two sections, top and bottom. The electrodes, when placed together form a hollow sphere ½ inch in diameter. The parts were machined from aluminum using a ½ inch milling ball. The insides of the trap were polished to help reduce the effects of stray electrical fields that would perturb the trajectory of the charged particles.

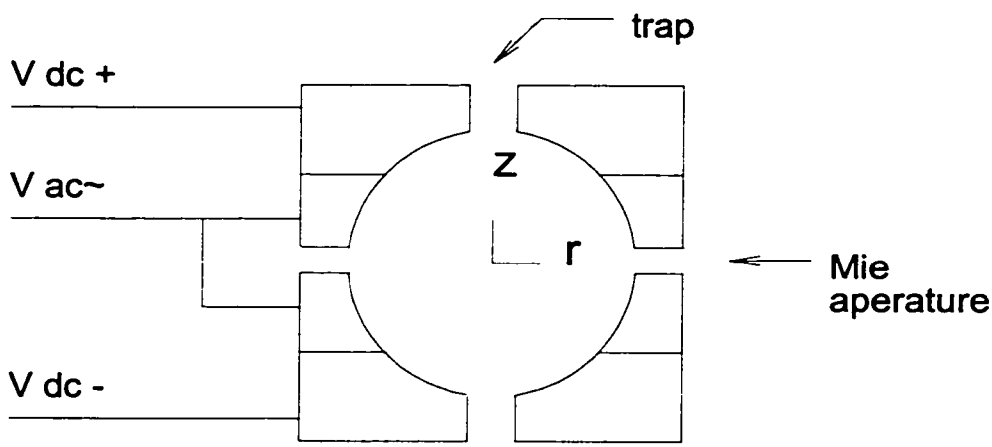

Figure 1.2 Cross-section of the quadrupole trap and associated electrode connections.

Each DC electrode is electrically isolated from the adjoining AC electrode by insulating sapphire rings. The sapphire spacers and electrodes are held together with non-conducting nylon screws. Four small optical access ports are machined into the ring electrodes to allow two laser

beams to enter and exit. The small size and symmetric placing of the optical access holes ensures that they do not disturb the electric field of the trap appreciably. Additionally, the two halves of the AC ring electrode are kept separated with two small metal washers that are 0.1 mm thick. This slit allows HeNe light scattering off the suspended aerosol to be angularly resolved for sizing purposes.

As mentioned before, the ring electrode confines the particle to the center of the trap using an AC potential. The power supply used for this is an Industrial Test Equipment Model 5900 variable AC power supply. Voltages used to trap particles are on the order of 100 - 1000 volts AC at a frequency of 93 Hz or slightly higher. A higher AC frequency sometimes helps confine the Brownian motion of some of the smaller particles.

The DC endcap electrodes are responsible for balancing the particle against gravitational force. A measure of the balance voltage can be used as an indicator of particle mass if the charge on the particle is known. (See equation 1.1 below). To accurately adjust the trap balance voltage, the suspended particle is monitored with a TV / microscope assembly. Ninety degrees to the direction of the laser illuminating the particle is a Burle model TC651EA video camera connected to a Leica Monozoom lens. The image appearing on the monitor is used to adjust the DC balance voltage.

$$\frac{q}{m} = \frac{g z_0}{C_0 V_{dc}} \qquad \text{Equation 1.1}$$

In equation 1.1, q/m represents the charge to mass ratio of the aerosol in the trap in coulombs per gram, z_0 is the trap void radius, C_0 is a dimensionless levitation constant based on trap geometry and V_{dc} is the voltage needed to balance the particle against gravity. For the flytrap geometry, Z_0 is 0.25 inches and C_0 is 0.908. Given a particle with a fixed charge in the trap, measuring the balance voltage is an ideal method for measuring particle mass. In a non-equilibrium environment, the dynamics of particle mass can be determined by plotting balance voltage as a

function of time: any change in particle mass will easily show up as a change in balance voltage. Alternatively, if the particle mass is known, the charge on the aerosol can be determined.

Rather than purchase a commercial power supply, needed for the dc endcap electrodes, one was constructed at UNH. This power supply was constructed to deliver 0 - 100 volts dc, to an accuracy of 0.01 volt to the endcap electrodes. The balance voltage is measured using a handheld multimeter. Using the coarse and fine DC electrode controls, with the TV camera for feedback, allowed for the determination of aerosol mass to a tenth of a nanogram. Calibration of this technique was carried out by tribiologicaly injecting latex spheres of known size and density into the trap.

1.4 The Raman System

Chemical information on the suspended aerosols in the quadrupole trap is obtained with the use of a Raman spectroscopy system. Raman spectroscopy is a powerful tool for obtaining compositional information on aqueous solutions and solids. The technique is similar to infrared spectroscopy in that it detects the presence of certain chemical moieties through their vibrational spectra. These spectra serve as chemical fingerprints for the presence of these chemical species. Spectra of compounds containing the same anion but different cations can also be distinguished (Fung and Tang, 1989). This technique can be used extensively for nitrates, sulfates and organic compounds and is therefore quite useful for identifying the composition of atmospheric aerosols. However, Raman spectroscopy is not useful for characterizing monatomic cations or anions such as Cl^-, H^+ or Na^+.

1.4.1 The Nature of Raman Spectroscopy

Raman spectroscopy is a powerful tool for obtaining compositional information on aqueous solutions and solids. Raman spectroscopy can be described classically or quantum mechanically. Classical models describe molecules as atoms held together by chemical bonds. The mass-spring systems have associated spring constants and resonant vibration frequencies. The normal modes of vibration of the mass-spring systems are excited through inelastic scattering of high intensity, fixed frequency light. The fact that the vibration modes are distinct, exhibiting narrow bands in vibration spectra is described quantum mechanically.

Raman spectra are taken by illuminating the compound of interest with a fixed frequency excitation laser and collecting the resultant scattered laser light (Van Duyne, 1979). Most of the scattered light will do so elastically, resulting in scattered light of the same wavelength. A small fraction of the photons will undergo a scattering process in which the photon energies are shifted relative to their initial energies (determined by the excitation laser frequency) by an amount equal to the vibrational frequencies of the molecule being probed. The Raman spectra are obtained by spectrally resolving this scattered light (Carleton et al, 1995).

Typical molecular vibrational frequencies are in the 1000 to 3600 cm^{-1} range. For excitation wavelengths of 532 nm, this corresponds to Raman emission at 560 to 660 nm. Therefore, the Raman technique has the advantage that both the excitation and scattering wavelengths can be chosen in the visible wavelength range. Lasers and detectors are readily available in this wavelength region. This wavelength range also avoids some of the infrared wavelength ranges where water is a strong absorber. As a result, Raman spectroscopy can easily be performed in aqueous solutions (Carleton et al., 1995)

Species must have Raman active modes in order to be able to identify them with Raman spectroscopy. The strongest Raman features result from anions which tend to have large polarizibilities such as $SO_4^{=}$ and NO_3^{-}. Other species which are Raman active include organic

compounds which have C=C double bonds, benzene rings, and C-H bonds. Water is also Raman active with several large features in the 3000 to 3600 cm^{-1} O-H stretching region.

1.4.2 Raman System Layout

The Raman spectroscopy system is composed of a diode pump doubled Nd:YAG excitation laser (532 nm wavelength), focusing optics, a fast optical system for signal collection, a 0.28 m monochromator and a high efficiency liquid nitrogen cooled CCD detector. The CCD detector system is controlled with a Dell 486 personal computer, which aids in spectrum acquisition and camera control.

There are several types of fixed frequency lasers that are used for Raman spectroscopy. These include ion lasers, solid-state lasers and diode lasers. Each type of laser has drawbacks and benefits. Some scientific considerations had to be made in choosing a Raman laser, including output wavelength and spectral purity. The cross section for Raman scattering is proportional to the laser frequency (v) to the fourth power. The implication is that shorter wavelengths have higher excitation efficiencies. For the flytrap instrument, a diode pumped solid-state (DPSS) Nd:YAG laser manufactured by Coherent was chosen for Raman spectroscopy work. The light produced by the laser is intercavity doubled, resulting in light with a 532 nanometer wavelength. The designed power output of the laser was intended to be a nominal 150 mW. After a failure in the laser cavity the laser had to be modified at the factory to output only 100 mW of power. The Coherent DPSS laser was more expensive than a higher power argon-ion laser. However, the DPSS laser is more electrically efficient and requires only air cooling as opposed to water cooling. This will prove to be beneficial when the time comes to use Flytrap as a field instrument.

One of the drawbacks of Raman spectroscopy is that the Raman interaction is a two photon scattering process, and as such is not a very efficient effect. Raman signals tend to be

somewhat weak. Typical values of Raman cross sections are on the order of 10^{-30} cm^2 sr^{-1}. Increasing the excitation laser photon fluence at the particle surface can maximize the Raman signal. This can be accomplished in one of two ways: increasing the laser power (expensive) or maximizing the overlap between the excitation laser beam and the particle.

If the excitation laser beam cross section is significantly larger than typical particle diameters, most of the laser power is thrown away. To avoid this, a series of optics is used to focus most of the laser light onto the particle suspended in the trap. The Raman laser can be focussed to a very narrow bean by first expanding the laser beam with an 8x beam expander and then using a 20 cm focal length achromatic lens to focus the beam down to a small waist size. The ideal beam waist (w_o) can be determined using Gaussian optics. The resulting beam waist can be described with

$$w_0 = \frac{f \cdot \lambda}{\pi \cdot w_i} \qquad \text{Equation 1.2}$$

where w_i is the initial beam size, λ is the laser wavelength, f is focal length of the focussing lens. The result that a larger incident beam will have a smaller beam waist is the reason for including a 8x beam expander in the beam path. Some laser power is lost at the optics interfaces, but the overall effect is to dramatically increase the beam fluence at the particle surface. (All of 100 mW of laser energy is focussed onto particle or at least onto a size of 40 μm). Ideally in our setup, the smallest beam waist we could achieve is approximately 40 microns.

As expected, aligning a 40 μm beam onto a particle 5 μm in diameter is not an easy task. This task is simplified by placing the focussing lens in a Newport XYZ positioning stage. This allows for extremely fine control of the beam waist placement.

Several problematic effects arise when illuminating small aerosol with high number of photons. These effects include thermophoresis, photophoresis, and particle ablation (especially with particles that are highly absorbent such as carbon). The thermophoresis and photophoresis

effects have a tendency to push particle out of the center of the trap, up the potential well and usually out of the beam waist as well. The result is a finicky problem in trying to align a small beam waist onto a small particle such that the scattered laser light is collected efficiently by the monochromator.

It is desirable to have fast collection optics (large collection solid angle) so that as much of the Raman signal as possible is collected by the monochromator. To efficiently couple light into the monochromator, it is necessary to f/match the monochromator's collection optics (Carleton et al., 1995). These two conditions are easily met with a two lens system (see figure 1.1). The first lens is a low f/# lens to collect as much light as possible. This collimates the light and directs it to the second lens that focuses the light into the entrance slit of the monochromator. Both of these lenses are high quality achromatics that are optimized to reduce spherical and chromatic aberrations. This ensures that light from the center and edges of the lenses focuses to the same point, as does light of different wavelengths (Carleton et al, 1995).

The key task of the Raman monochromator is to spectrally resolve the scattered laser light from the suspended aerosol. Since the elastically scattered laser is orders of magnitude stronger than the Raman signal, this can be difficult. The development of holographic notch filters with very sharp wavelength cutons and high optical densities at laser wavelengths simplifies the rejection of elastically scattered laser light. A holographic notch filter is placed between the two collection lenses to minimize the transmission of **elastically** scattered light. The notch filter selected is a Kaiser Optical HNPF-532-1.5, which has an outer diameter of 6.0 cm. The notch filter rejects almost all of the laser light at 532 nm and turns on at a Raman shift of approximately 600 cm^{-1}. It has approximately a 2.85-cm clear aperture. Because the light is collimated between the two collection lenses, locating the notch filter between them is ideal.

The key task of the Raman monochromator is to spectrally resolve the scattered laser light from the suspended aerosol. The monochromator for the Raman system is an Acton

SpectraPro 275. It has a 0.275-meter focal length, a triple grating mount and a microprocessor controller. Two different diffraction gratings were installed in the monochromator grating mount. The first is a grating with 1200 g/mm, used for high-resolution work. The second grating has 300 g/mm and is used for spectroscopy where a 4600 cm^{-1} span is needed.

The monochromator comes with a variable entrance slit that varies the system resolution. Larger slits yield lower resolution but greater light collection. A slit width of 200 microns seemed adequate to meet the needs of work done with the Flytrap instrument. A 200 μm slit width provided adequate light collection, adequate spectral resolution and minimal alignment problems.

The Raman system detector is key towards optimizing signal-to-noise ratios and achieving measurable signals from particles as small as possible. For the Flytrap instrument we used a liquid nitrogen cooled, thinned, back-illuminated CCD detector manufactured by Princeton Instruments. This detector has a high quantum efficiency (80%) and low dark noise. The detector is a 512x512-pixel format with 27x27 μm pixels. The detector chip is mounted in a liquid nitrogen dewar and can operate from –80°C to -140°C. This provides dark count rates of less than 0.00015 electrons/pixel/sec at -120°C. The liquid nitrogen hold times are on the order of eight hours. Because of the vacuum isolation of the liquid nitrogen dewar, the detector has several windows mounted in front of it that were anti-reflection coated to reduce light loss from reflection.

The chip in the CCD camera measures 512x512 pixels. The chip is mounted with its shift register perpendicular to the wavelength axis (the horizontal axis). This is the typical orientation used for spectroscopy. Each pixel in the chip has a full well capacity of 5×10^5 electrons. When several pixels are binned together, the full capacity is limited by the shift register at 1.5×10^6 electrons. This allowed binning of the vertical pixels into a single "super pixel". This method enables a higher signal level and a longer signal collection time prior to saturating the detector

electronics. A background subtracted "background" shows the actual noise variation of the CCD chip. Figure 1.3 below shows a spectrum of this type for an exposure time of 10 seconds.

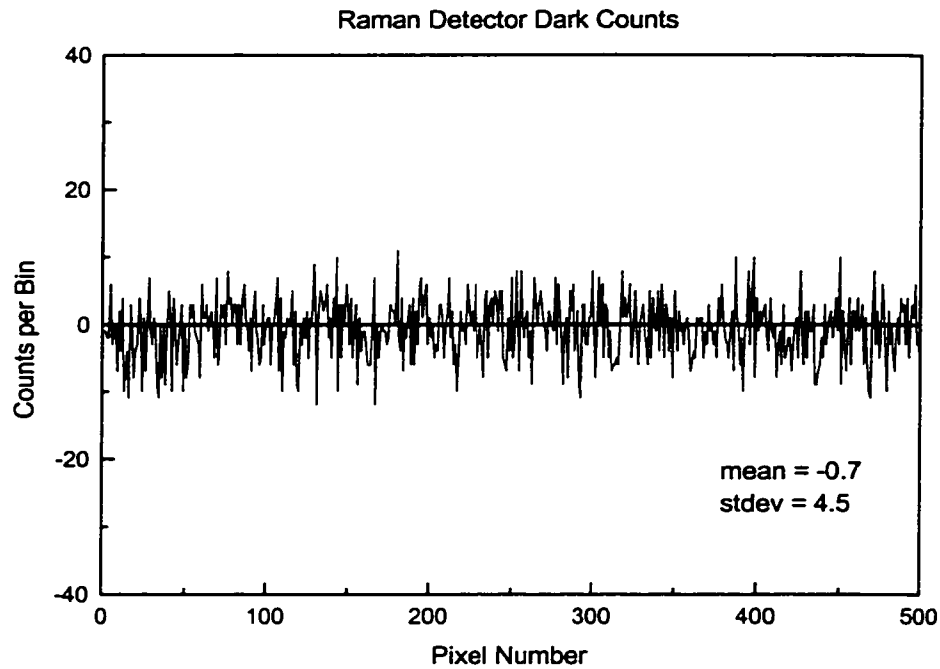

Figure 1.3 Raman dark counts. Two background spectra taken and subtracted from one another. This spectrum gives an idea of noise levels in the CCD detector system. The mean counts per bin for all 512 horizontal pixels was calculated to be –0.7 with a standard deviation of 4.5 counts per bin.

The CCD detector comes with a controller that provides the electronic and thermal control for the system. The controller also manipulates the mechanical shutter that mounts in front of the monochromator and sets the exposure time for the detector. Exposure times can be as short as 0.05 seconds or as long as many minutes. A short exposure time will lead to a small Raman signal whereas a long exposure can saturate the detector pixels with electrons. Long exposure times also lead to spikes in the spectra due to the interaction of cosmic rays with the CCD chip.

1.4.3 Raman System Calibrations

Prior to using the Raman system to identify various chemical compounds, the system was wavelength calibrated. This involved mapping each pixel in the CCD camera to a specific wavelength. The response of the monochromator is extremely linear with respect to wavelength, therefore the calibration was performed using only a mercury pen lamp and a HeNe laser to produce suitable peaks. Due to the large amounts of light produced by the pen lamp and laser, each calibration spectra was limited to a 0.05-second duration. A typical calibration spectrum is shown in figure 1.4 below.

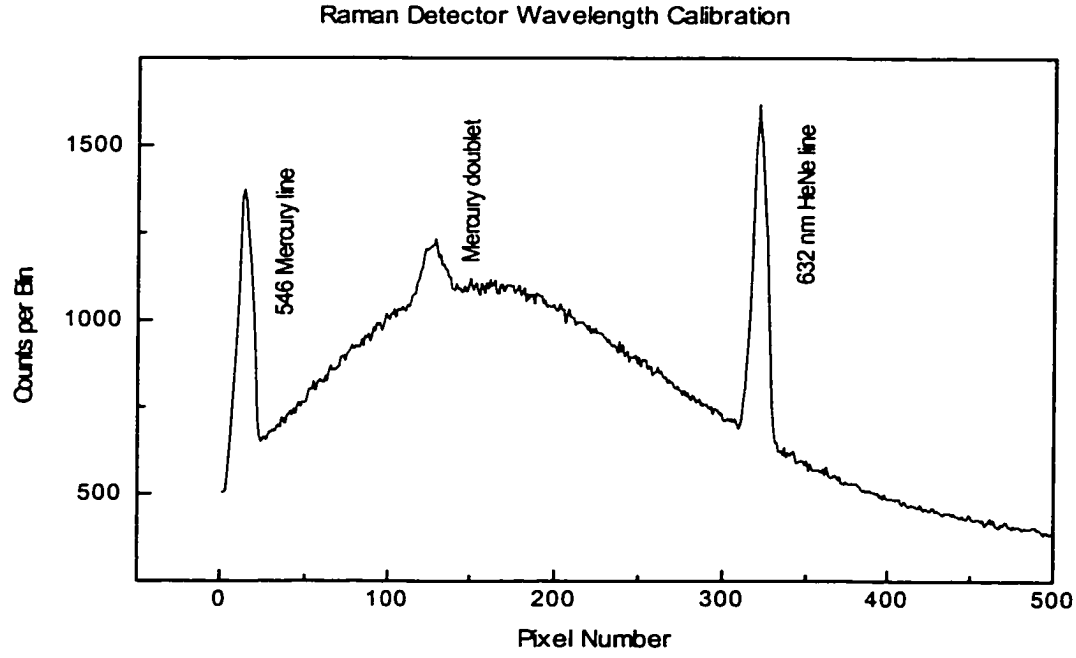

Figure 1.4 Experimental Raman system wavelength calibration. The calibration of the 300 g/mm grating was carried out using a HeNe laser to produce the 632-nm line and a mercury lamp to produce the doublet and 546-nm line.

One of the goals of the Raman spectra is to use them to determine particle composition. This includes identifying the primary components present in the particle but also estimating their concentration as well. The Raman system was first tested out using bulk solution samples placed

in quartz cuvette in lieu of the quadrupole trap. It was apparent from these tests that different compounds have unique, easily identifiable spectra. A list of observed Raman frequencies used to identify compounds is given in Table 1.1 below.

Observed Raman Frequencies (cm^{-1})

Species				
NH_3	3335	950	3414	1628
NH_4^+	3033	1685	3134	1397
H_2O	3652	3756	1640	2138
SO_2	1151	524	1361	*
$SO_4^=$	980	451	1104	613
$CO_3^=$	1015	879	1365	680
NO_3^-	1050	831	1390	720

Table 1.1 Observed Raman lines. The table lists the strongest features on the left and the weaker features to the right.

Figure 1.5, below illustrates a typical Raman spectrum of a $NaNO_3$ solution. The spectrum was taken using the 300 g/mm grating. The use of this grating spans approximately 4000 cm^{-1} and allows for the simultaneous identification of various nitrate peaks and water peaks. The predominate nitrate peak is located at 1050 cm^{-1} and is the result of a symmetric stretch. The resolution of the Raman frequencies can be increased by decreasing the size of the monochromator entrance slit, but at the cost of the overall signal strength. A balance of resolution and signal intensity was achieved by setting the slit aperture to 200 μm.

In contrast to the 300 g/mm grating, a spectrum of Na_2SO_4 taken with the 1200 g/mm grating is shown in figure 1.6. The predominant sulfate peak shows up at 980 cm^{-1} and is due to the symmetric SO_4^{2-} ion stretch. The resolution of the observed Raman frequencies is increased by using the 1200 g/mm grating, but the spectrum only spans approximately 1000 cm^{-1}.

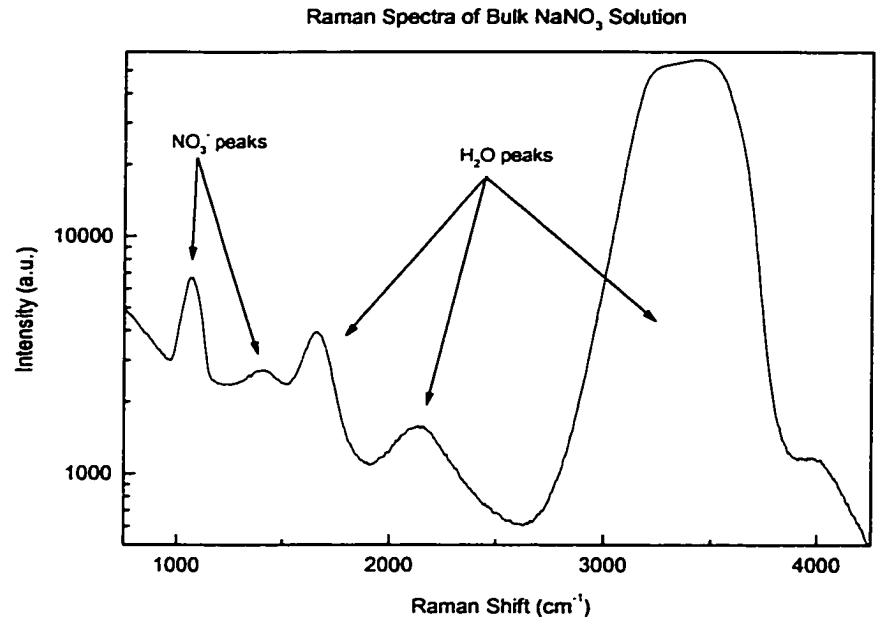

Figure 1.5 Raman spectrum of a bulk 2M $NaNO_3$ solution at 25 °C. The spectrum was taken using the 300 g/mm grating in the monochromator. Nitrate peaks are located at 1050 cm^{-1} and 1390 cm^{-1}. Water peaks are located at 1640 cm^{-1}, 2138 cm^{-1}, 3652 cm^{-1} and 3756 cm^{-1}. The last two water peaks show up as a single, convoluted peak.

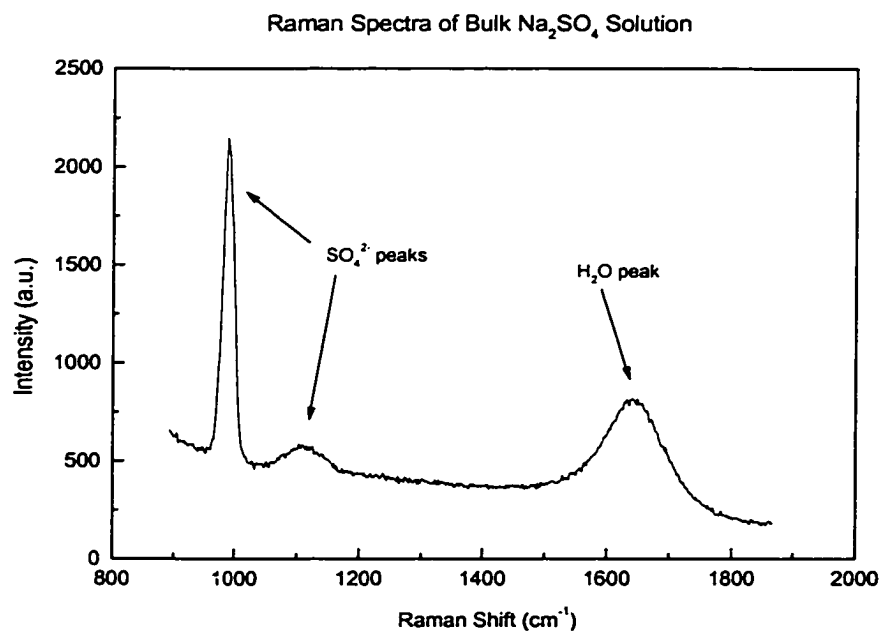

Figure 1.6 Raman spectrum of a bulk 2M Na_2SO_4 solution at 25 °C. The spectrum was taken using the 1200 g/mm grating in the monochromator. The Sulfate peaks are located at 980 cm^{-1} and 1104 cm^{-1}. The only observed water peak is located at 1640 cm^{-1}.

In order to determine composition from Raman spectra, it is important to be able to relate the Raman peak intensities to this composition. For a bulk solution excited by a fixed laser beam size, Raman peak intensities should be linearly proportional to concentration (Carleton et al, 1995). Experimental verification of this relationship was conducted for a number of atmospherically relevant substances. In examining suspended aerosols, however, this cannot be accomplished. For many suspended aerosols, the particle will wander in and out of the beam waist occasionally, making the peak Raman intensity dependant upon the time spent in the beam waist, as well as proportional to the concentration of the compound of interest. Trying to deconvolve the spectra in this manner proved to be a formidable task.

It is still possible however, to determine the concentration of aerosol components solely from Raman spectra. Instead of using absolute peak intensities, ratios of integrated peak intensities are used to determine concentrations of relevant species in the aerosol phase. As an example, nitrate concentration in an aqueous aerosol can be determined by calculating the ratio of area underneath the nitrate 1050 cm^{-1} peak to the area underneath the 3652 cm^{-1} water peak. This ratio is indicative of nitrate concentration in the droplet.

To get an exact one-to-one correspondence, a calibration curve of bulk solutions was generated. A well-characterized bulk solution on $NaNO_3$ was inserted into a cuvette and a Raman spectrum taken. The ratio of the area underneath the nitrate 1050 cm^{-1} peak to the water 3652 cm^{-1} peak area was calculated. This procedure was repeated several times with subsequent dilutions of the original solution until the nitrate peak was no longer detectable. The curve generated for the nitrate calibration is shown in figure 1.7 below.

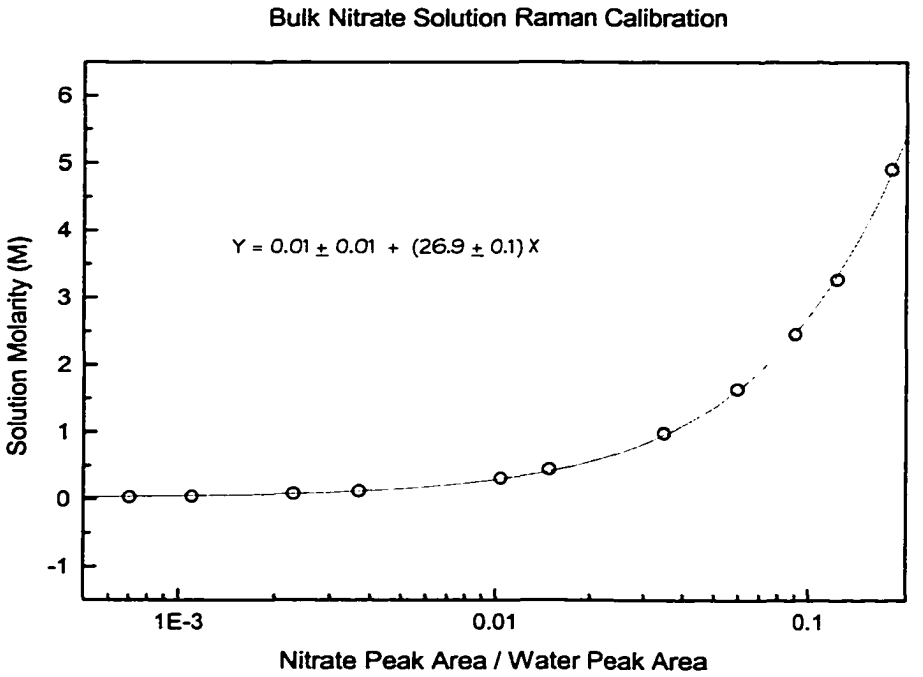

Figure 1.7 A calibration curve for bulk nitrate solution carried out with the Raman system. Circles represent the measured data points and the solid line represents the fitted curve.

The ratio of peak areas proved to be extremely linear with respect to solution molarity. The minimized chi-square fit to a straight line is inset in figure 1.6 ($r^2 = 0.99$). Once this curve was generated, it was an easy matter to determine nitrate concentrations in aqueous aerosols in the trap simply by measuring nitrate peak areas and water peak areas. Calibrations of this type were carried out for sulfate, nitrate, ammonium and bicarbonate.

Unlike Na_2SO_4 and $NaNO_3$, there are some species that do not completely dissociate in solution, or which have dissociation constants that are a function of temperature or solution concentration. Typical atmospheric compounds, which fall into this category, are H_2SO_4 and HNO_3. The effect of temperature and solution concentration of these compounds on the Raman calibrations are addressed in chapters 2 and 3.

1.5 The Mie Detector System

One of the key physical parameters measured with the flytrap instrument is the particle radius. To date several methods of sizing trapped aerosols have been investigated including springpointing, electron stepping, integrated light scattering and angularly resolved light scattering (Mie scattering). Some of these methods are briefly described below.

Springpointing involves the use of the voltage on AC ring electrode on the trap to cause the particle to oscillate in the z - plane. The AC voltage is increased until the trapped particle is forced out of the stability envelope, causing the particle to undergo a highly oscillatory motion. Making assumptions about the field strength parameter, and the particle aerodynamic drag parameter, it is possible to theoretically derive the particle radius. This technique worked well for highly charged particles in the quadrupole trap that were larger than twenty microns in diameter.

At the conclusion of the Phase II SBIR, the flytrap instrument used a one-element photo-detector in conjunction with the HeNe laser to determine the radius of a particle suspended in the trap. The laser light interacting with the suspended aerosol will scatter according to Mie theory. The integrated Mie signal, measured by the photo detector was directly related to the particle radius. This system was calibrated using polystyrene latex spheres of several different diameters. The method was quick but somewhat inaccurate. Poor size resolution as well as background problems with reflected laser light forced me to adopt a different sizing technique. I found the easiest, most accurate method of quickly determining particle radius is though the use of angularly resolved Mie scattering measurements. A description of this method is given below.

1.5.1 Mie Scattering Theory

Mie scattering theory is a complete, formal theory of the interaction of a plane electromagnetic wave with a dielectric sphere (a particle). The mathematical results of the theory, representing the angular distribution of scattered laser light, can be given in the form of

an infinite series (Van de Hulst, 1981). The derivation of the solution is a straightforward application of classical electrodynamics. Most of the work in using Mie scattering theory in physical applications is the calculation of the elements of the *amplitude scattering matrix* S_1, S_2, S_3 and S_4. Conveniently, when considering scattering off a homogeneous dielectric sphere (as I often did in flytrap applications), S_3 and S_4 vanish. S_1 and S_2 then are functions only of the scattering angle θ and can be easily calculated using the following expressions:

$$S_1(\theta) = \sum_{n=1}^{\infty} \frac{2n+1}{n(n+1)} \left[a_n \pi_n + b_n \tau_n \right] \qquad \text{Equation 1.3}$$

$$S_2(\theta) = \sum_{n=1}^{\infty} \frac{2n+1}{n(n+1)} \left[b_n \pi_n + a_n \tau_n \right] \qquad \text{Equation 1.4}$$

where

$$\pi_n = \frac{1}{\sin(\theta)} P_n^1(\cos\theta) \qquad \text{Equation 1.5}$$

$$\tau_n = \frac{1}{\sin(\theta)} \frac{d}{d\theta} P_n^1(\cos\theta) \qquad \text{Equation 1.6}$$

The expression denoted as P^1_n is an associated Legendre polynomial. These angle-dependent functions pose no severe computation problems and can be calculated via the upward recurrence relations given by

$$\pi_n = \frac{(2n-1)}{(n-1)} \mu \pi_{n-1} - \frac{n}{(n-1)} \pi_{n-2} \qquad \text{Equation 1.7}$$

and

$$\tau_n = n\mu\pi_n - (n+1)\pi_{n-1} \qquad \text{Equation 1.8}$$

where $\mu = \cos(\theta)$, $\pi_0 = 0$ and $\pi_1 = 1$.

The coefficients a_n and b_n above however, are a bit more complicated to calculate and are given by

$$a_n = \frac{\psi_n'(mx)\psi_n(x) - m\psi_n(mx)\psi_n'(x)}{\psi_n'(mx)\xi_n(x) - m\psi_n(mx)\xi_n'(x)} \quad \text{Equation 1.9}$$

$$b_n = \frac{m\psi_n'(mx)\psi_n(x) - \psi_n(mx)\psi_n'(x)}{m\psi_n'(mx)\xi_n(x) - \psi_n(mx)\xi_n'(x)} \quad \text{Equation 1.10}$$

where ψ and ξ are the Riccati-Bessel functions and defined by

$$\psi_n(x) = xj_n(x) \quad \text{Equation 1.11}$$

The j_n are spherical Bessel functions. The Riccati-Bessel functions are calculated with the use of the following recurrence relations

$$\psi_{n+1}(x) = \frac{2n+1}{x}\psi_n(x) - \psi_{n-1}(x) \quad \text{Equation 1.12}$$

$$\xi_{n+1}(x) = \frac{2n+1}{x}\xi_n(x) - \xi_{n-1}(x) \quad \text{Equation 1.13}$$

The first few Riccati-Bessel functions are know to be

$$\psi_{-1}(x) = \cos(x) \quad \text{Equation 1.14}$$

$$\psi_0(x) = \sin(x) \quad \text{Equation 1.15}$$

$$\xi_{-1}(x) = \cos(x) - i\sin(x) \quad \text{Equation 1.16}$$

$$\xi_0(x) = \sin(x) - i\cos(x) \quad \text{Equation 1.17}$$

Using the recurrence relations given above, the complete theoretical angular dependence of the amplitude scattering functions for a given complex index of refraction, wavelength of light and particle radius were calculated. Implicit in these calculations is the assumption that the particle is spherical. This assumption is valid for any aqueous droplet in the quadrupole trap. The results of these calculations are shown in Figure 1.8 and demonstrate how the oscillation

spacing in scattered light intensity is sensitive to particle radius at modest scattering angles (35 to 55 degrees). The software used to perform these calculations is given in appendix 1.

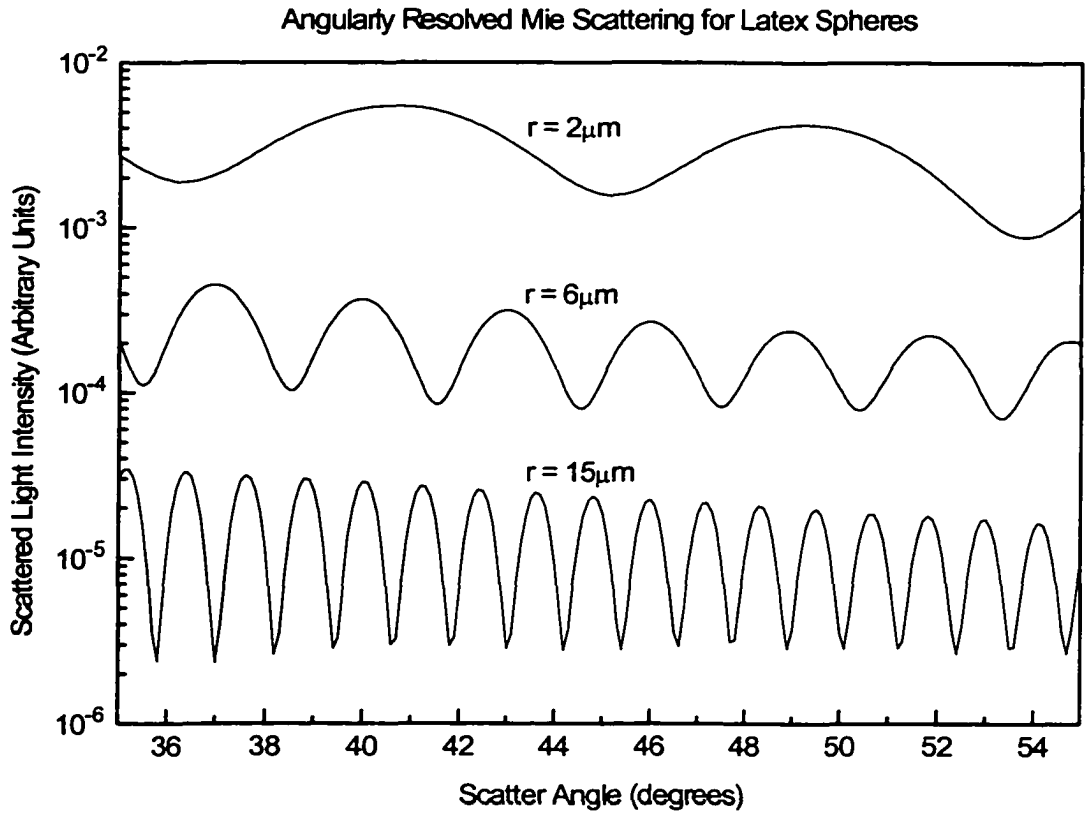

Figure 1.8 Angularly resolved Mie scattering for latex spheres of several different diameters. As the particle radius increases, oscillation spacing decreases. It should be noted that the three Light Intensity curves are not normalized.

While the forward scattering intensity is sensitive to both particle radius and complex index of refraction, the oscillation spacing (the number of degrees per single oscillation) of the angular Mie scattering is a quantitative indication of particle radius. Figure 1.9 below shows the number of degrees per oscillation is sensitive to particle radius and fairly insensitive to particle index of refraction. Measuring the angularly resolved scattered laser light can therefore be used for determining particle radius, independent of particle composition.

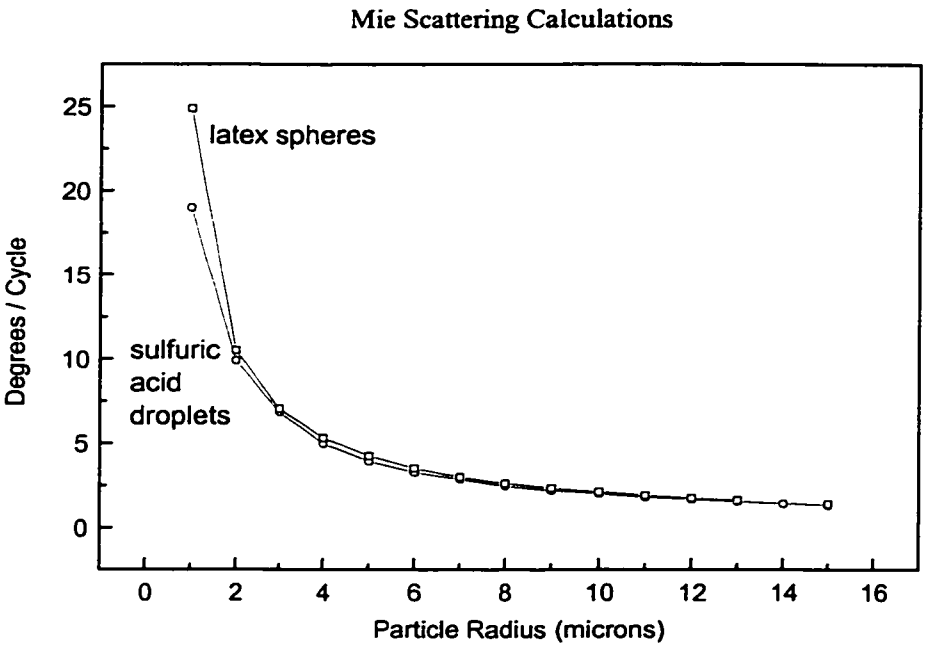

Figure 1.9 Degrees per oscillation in angularly resolved Mie scattering for particles of different composition (a) latex spheres (n = 1.575, k = 0.0033) and (b) 60 wt% sulfuric acid (n = 1.376, k = $2.3*10^{-8}$)

1.5.2 Mie Scattering System Calibration

To measure the radius of a particle in the trap is a fairly simple exercise using the Mie scattering system. The system is comprised of a HeNe laser that emits 632-nm wavelength light, two 6-cm achromatic collection lenses and a thermoelectrically cooled CCD camera manufactured by the Santa Barbara Instrument Group. The HeNe laser illuminates a particle in trap. The laser light is elastically scattered off of a suspended aerosol according to Mie theory and exits the trap through the optical access slot (see figure 1.2). The exiting scattered laser light is then collected and focussed onto the CCD chip by the two achromatic f6 lenses. Typical exposure times are usually 0.01 second in duration. The experimental geometry of the layout is shown in figure 1.1.

Figure 1.10 below is an image of HeNe light scattered off of a 13-μm latex sphere suspended in the quadrupole trap. The peaks in scattered light intensity are clearly visible. Once

an image is obtained, the digital photo is downloaded onto a laptop computer where the radius analysis is performed.

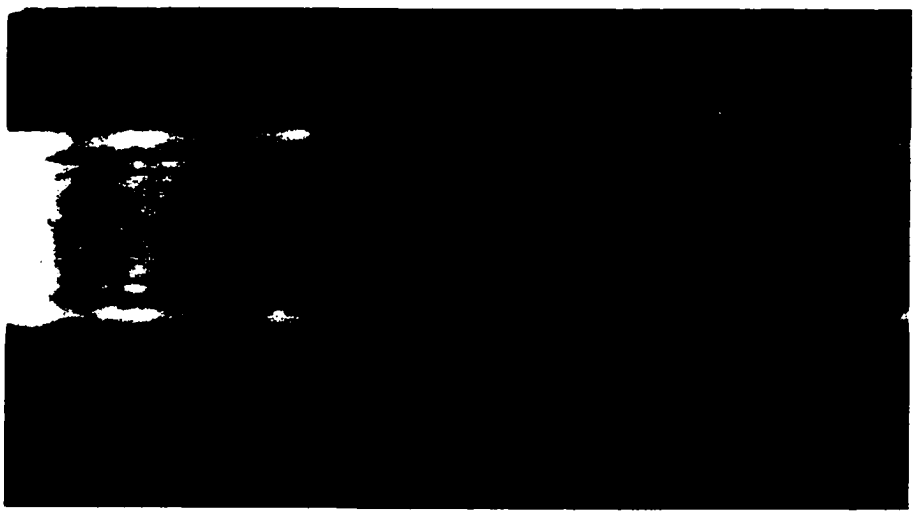

Figure 1.10 A CCD image of Mie scattered light from a 13 μm latex sphere.

The CCD chip in the Mie camera measures 200 pixels by 300 pixels, with each pixel having a 10 μm size. As with the Raman camera, the vertical pixels are binned into a single "super-pixel". Converting the horizontal pixel number to a scattering angle can be performed by examining the geometry of the experiment. Additionally, it should be noted that the bands of high intensity laser light do not extend from the lowest vertical pixel to highest vertical pixel. This is a result of the finite (and well-known) thickness of the spacers holding the two AC electrodes apart, from which the Mie scattered light escapes the trap. For each photo taken with the Mie camera, a plot of scatter angle versus superpixel counts was created.

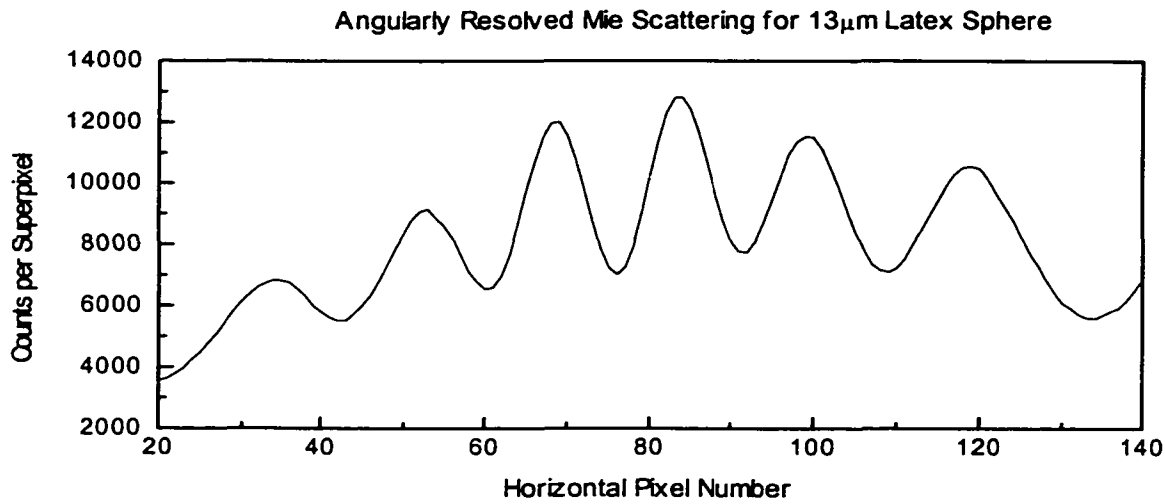

Figure 1.11 Angularly resolved Mie scattering for a 13μm latex sphere suspended in the quadrupole trap.

An analysis of these plots yields information on the particle radius. Because it is the oscillation spacing being quantified, any error in the absolute angle is unimportant in the data analysis. The number of degrees per oscillation obtained is then converted to particle radius by interpolation of the data shown in figure 1.9.

A careful examination of figure 1.11 shows intensity as a function of scatter angle. The width of the peaks varies and distance between intensity peaks varies. This is the result of a small distortion created by collection optics. The problem is easily corrected with a digital distortion filter written into the software used for the sizing analysis.

Calibration of the Mie scattering system was carried out with the use of PDVB latex spheres. Spheres suspended in a surfactant were purchased from Duke Scientific. Several sizes of spheres (10, 15 and 26 μm in radius, with an uncertainty of 10% as reported by the manufacturer) were dried and injected one at a time into the quadrupole trap, at which time a Mie photo was taken. Dozens of spheres of each size were analyzed for radius. Statistically, the data obtained with the Mie system agreed very well with the reported size distributions of the spheres by the manufacturer.

Using the Mie scattering system measurements of the radius of a particle in the trap to an accuracy of 5% can be made. The accuracy of the radius data can be determined by measuring a single particle several times with multiple exposures. There are limitations on the size of the particles in the trap that can be measured using this method as well. The diameter of the particles must be between 2 and 30 μm for this to be an accurate method. The radius data can be taken easily, quickly, accurately, reproducibly, cheaply and with a minimal perturbation to the particle.

1.6 The Particle Injector

The study of single aerosol chemistry and physics requires a method for generating and delivering individual particles to the quadrupole trap. Several methods of injecting charged aqueous aerosols into the trap were tried, none of which proved to be reliable or reproducible. These methods included using a nebulizer, a corona discharge and assorted devices involving radioactive materials (see chapter 4 for a complete description of these methods). What was eventually used was a Model 201 Single Particle Generator System manufactured by Uni-Photon Systems Inc. The single particle generator was able to meet experimental needs for injecting highly charged aqueous aerosols composed of a variety of compounds into the quadrupole trap.

The particle injector is akin to an ink jet printer head: fluid from reservoir occupies space between two piezoelectric crystals. A small voltage delivered from a controller causes the piezoelectric crystals to expand. When the crystals expand, the space between the crystals contracts causing fluid from the reservoir to be forced out through an orifice. The result is an artificially generated fast moving aerosol traveling downwards at about 1 meter per second. The particle is quickly slowed down by friction with the ambient air.

The particle generator is able to supply a single particle or a stream of particles composed of any number of aqueous solutions including various salts and acids. The size of the

initial droplets range from 50 μm to 30 μm depending on the type of orifice used at the injector head. If the droplets are composed of water, they will evaporate in a matter of seconds due to the decreased relative humidity in the room. If the solution in the reservoir contains nitric or sulfuric acid, the aerosols can last for hours, due to the low vapor pressure of these substances. Flooding the injector head reservoir with a salt solution can also create small resultant salt aerosols.

Droplets created with the particle generator can by charged by induction if the solution in the reservoir has some electrical (ionic) conductivity. A small charging ring is placed over the tip of the emitting orifice and biased with a voltage from -450 V to + 450V. As a droplet is formed, the induced voltage causes a charge separation within the droplet. When the drop exits the orifice, the result is an aerosol with a net positive or negative charge. The magnitude of the charge on the droplet is dependent on several variables including the induction voltage, the orifice diameter, the ionic activity of the solution and the ejection voltage.

The most effective method found for creating small, highly charged aerosols is to start with a very dilute solution of salt or acid, such as $NaNO_3$ or H_2SO_4. The injector head is placed over the entrance of the quadrupole trap. A large induction voltage ensures that the droplets charge effectively. When the ejected droplet is trapped and comes to equilibrium with the background relative humidity, the only thing left is a small, highly charged aerosol in the trap. One can crudely determine the final size of the trapped aerosol by changing the concentration of the initial salt or acid solution up or down, depending on whether you want a larger or smaller aerosol.

There are several drawbacks to using this method for generating aerosols. The single particle generator unit is somewhat expensive – on the order of five thousand dollars. The injector can be a very fussy instrument to use: it is very easy for the injector orifice to become clogged with dried salt or contaminants from the fluid reservoir. It is also very easy to get air

trapped in the space between the piezoelectric crystals. Instead of forcing fluid out the orifice, only the air is compressed. The only recourse was to disassemble the unit and purge it of air.

1.7 Ancillary Controls

Aqueous particles injected into the trap, like sea-salt aerosols injected into the atmosphere will quickly equilibrate with the background relative humidity. In order to study heterogeneous chemistry of aqueous aerosols, the relative humidity in the chamber surrounding the trap must be well controlled and well characterized. The easiest way to control the relative humidity was with a saturator system in which dry, contaminant-free air was mixed with air bubbled through a water saturator in a well-characterized ratio.

Several different saturator systems were tried. The first method involved drawing air through a felt cloth soaked with water. This method turned out to be less than ideal: the relative humidity was close to 100% but the felt cloth introduced far to many loose particles into the air stream. The most ideal method of raising the "saturated" air flow relative humidity to 100% involved heating the air to 55°C and then bubbling this air through the bubbler (gas scrubber). Heating the air before sending it through the bubbler enabled the air to pick up more water vapor. The large volume of water ensured that the air flowing through the saturator system was cooled to room temperature before entering the trap chamber. By measuring and adjusting the saturated and dry flow rates through the system was possible to control the relative humidity in the trap chamber from 0% to 93% with an accuracy of ± 3%. Figure 1.12 below illustrates the method used to control the relative humidity in the trap chamber. Flow rates as high as 200 cm^3 per minute have given very reasonable relative humidity equilibrium times in the trap chamber without inducing much aerodynamic drag on the particle in the trap. The systems used to generate and control the HNO_3, SO_2 and O_3 are described in later chapters.

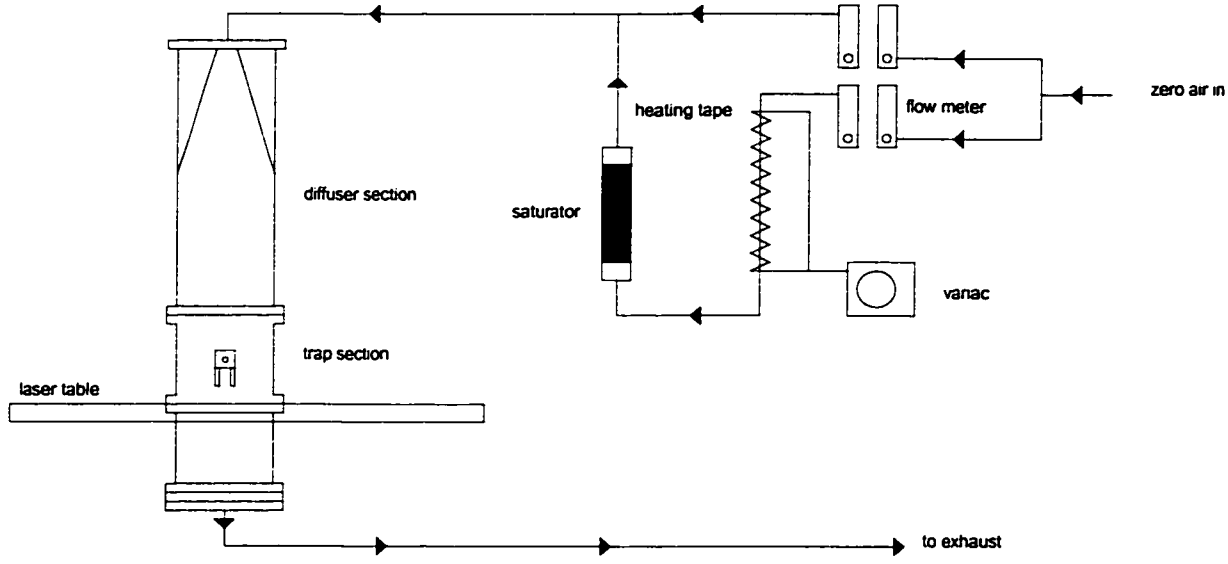

Figure 1.12 A diagram of the method used to control the relative humidity in the trap chamber. Air from a cylinder is split, part going through a flowmeter and then a saturator and part remaining dry. The two parts are then mixed in a desired ratio and delivered to the trap.

1.8 The $NaNO_3$ Droplet Test

The $NaNO_3$ droplet test was designed to be a complete, simultaneous test of all the Flytrap systems. The particle sizing method, the relative humidity system and the balance voltage measurement were tested in such a manner as to insure that these components could give meaningful experimental results. The main goal of this experiment however, was to test the quantitative methodology of the Raman spectroscopy system using two completely independent procedures.

The experiment was started by mixing a solution of NaCl, $NaNO_3$ and water (8 gm, 2 gm and 40 gm respectively). The solution was pipetted into the single particle injector head (the injector head was equipped with the 50 μm orifice tip). The injector head was placed over the trap entrance and a highly charged salt/nitrate aerosol was injected into the trap. The hydrating system was turned on to increase the relative humidity in the trap chamber from 40% (room relative humidity) to 93%.

The aerosol was allowed to come to equilibrium for thirty minutes, after which several measurements of the particle were made and relevant characteristics were obtained. These measurements included a Raman spectrum, a radius measurement and a balance voltage. Once these measurements were taken the relative humidity in the trap was lowered a bit and the process was repeated. This was repeated until the suspended NaCl / $NaNO_3$ droplet was completely dry (and spherical).

It should be pointed out that when a particle is injected into the trap, the RH of the room is usually well below the deliquescence point of the salt aerosol. The aerosol quickly dries as a result and the dry particle is usually very non-spherical in shape. If the RH is lowered slowly from 90% to 45% over the period of several hours, the resultant particle remains spherical. The outcome is that if the RH is lowered slowly, Mie scattering can be applied to the particle to get the dry particle radius.

The following data were obtained on a single $NaNO_3$ particle in the trap.

Run #	Relative Humidity	nitrate / water (ratio)	Radius (μm)	Balance Voltage (volts)
1	93% ± 5%	0.022 ± 0.002	10.0 ± 0.2	10.5 ± 0.2
2	78% ± 5%	0.022 ± 0.002	9.9 ± 0.2	9.9 ± 0.2
3	73% ± 5%	0.034 ± 0.002	9.8 ± 0.2	8.8 ± 0.2
4	65% ± 5%	0.032 ± 0.002	8.6 ± 0.2	9.0 ± 0.2
5	58% ± 5%	0.041 ± 0.002	7.9 ± 0.2	7.8 ± 0.2
6	52% ± 5%	0.053 ± 0.002	8.0 ± 0.2	6.0 ± 0.2
7	46% ± 5%	0.068 ± 0.002	7.6 ± 0.2	5.5 ± 0.2
8	35% ± 5%	1.018 ± 0.002	5.3 ± 0.2	3.9 ± 0.2

Table 1.2 Primary data taken for the $NaNO_3$ droplet test. The nitrate/water ratios were obtained from analysis of the Raman spectra.

The liquid water content of the particle is greatly affected by the ambient relative humidity as can be seen in figure 1.14. The area underneath the nitrate peak (near pixel number 50) remains somewhat constant while the water peak integrated counts varies from nearly 24k to nearly 800k. When the suspended aerosol is subjected to a relative humidity well below its deliquescent point, some water remains in the particle. The reason for this is that the particle

dries and solidifies from the outside in. The crystals of salt prevent the remaining water from evaporating by forming a solid shell. The salt in a solid state limits the diffusion of the remaining water. Experiments with other salt particles have had similar results. Depending on the size of the salt particle, the evacuation of all water from the particle can take anywhere from 15 to 30 hours.

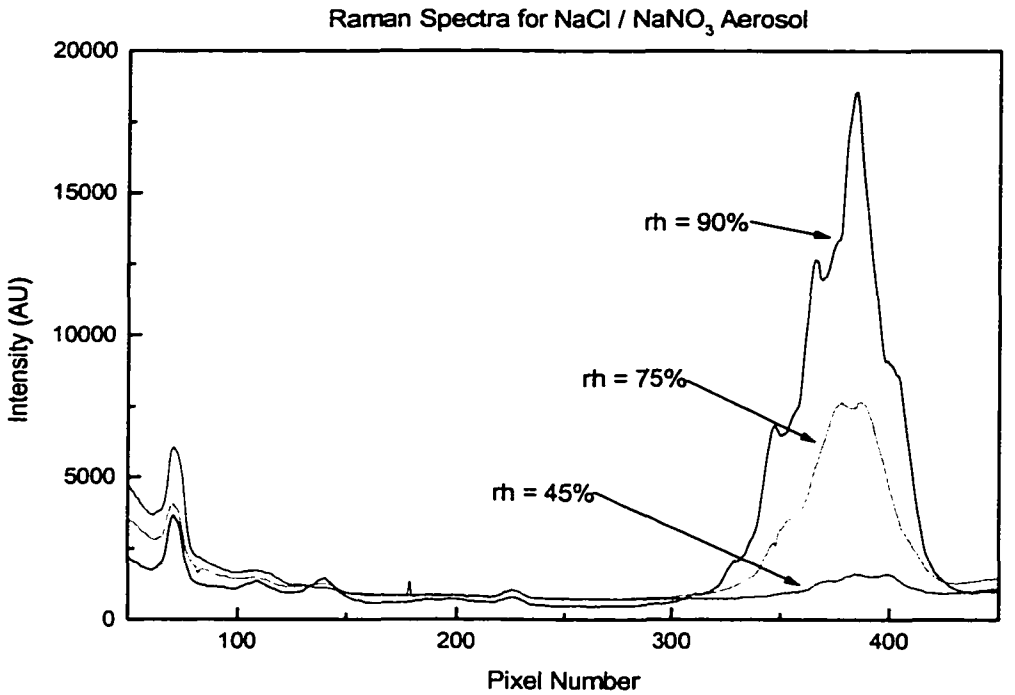

Figure 1.13 Raman spectra for a NaCl / $NaNO_3$ droplet suspended in the quadrupole trap. Illustrates the decreasing size of the water signal as the relative humidity of the trap chamber is slowly dropped from 90% to 45%. The nitrate peaks are located to the far left near pixel number 50.

One of the reasons for performing this experiment was to validate the technique of quantitative Raman spectroscopy by using a less direct method of determining particle composition. Utilizing measurements of balance voltage and radius, it was possible to estimate

the composition of the suspended aerosol for this particular experiment, independently of the Raman spectra.

It was assumed that the density of the dry aerosol was identical to that of the bulk NaCl / $NaNO_3$ mixture used to create the aerosol to begin with. From measurements of the balance voltage the charge to mass ratio for a suspended aerosol can be calculated. (See equation 1.1) When the radius and density of dry suspended aerosol are known, the mass can be calculated. The limiting factor is the uncertainty in the radius: about 0.2 μm in this experiment. From this, the initial charge on the particle can be determined. In this case of the dry NaCl / $NaNO_3$ aerosol, the charge was nearly 1.4×10^5 electrons. With the initial charge known, subsequent measurements of balance voltage yield a measurement of the particle mass.

In this specific experiment the charge and mass of **nitrate, sodium and chloride** were fixed, the only mass added to the aerosol is that of water. In either case, once the particle reaches the deliquescent relative humidity, the molarity can easily be measured: the number of moles of nitrate is known and the solution volume can be calculated from $V = 4/3\ \pi\ r^3$. This method of calculating / measuring the aerosol solution molarity is denoted as the "Mass Method" and can be compared to obtaining the molarity using Raman spectroscopy. A side-by-side comparison is give below.

Run	RH %	Radius microns	Volume solution Liter	Mass Method mole / liter	Raman Method Mole / liter
1	93	10.0 ± 0.2	4.19E-12	1.0 ± 0.2	0.82 ± 0.03
2	78	9.9 ± 0.2	4.06E-12	1.0 ± 0.2	0.83 ± 0.03
3	73	9.8 ± 0.2	3.94E-12	1.1 ± 0.2	1.24 ± 0.03
4	65	8.6 ± 0.2	2.66E-12	1.6 ± 0.3	1.17 ± 0.03
5	58	7.9 ± 0.2	2.07E-12	2.1 ± 0.4	1.48 ± 0.03
6	52	8.0 ± 0.2	2.15E-12	2.0 ± 0.4	1.92 ± 0.03
7	46	7.6 ± 0.2	1.84E-12	2.4 ± 0.5	2.44 ± 0.03

Table 1.3 A comparison of two different methods for determining the concentration of nitrate in a suspended, hydrated NaCl / $NaNO_3$ droplet in the quadrupole trap.

It should be noted that the Raman method for obtaining solution concentrations is more accurate. This is based solely on experimental uncertainties. Run number 8 was intentionally left out of this comparison. The aerosol in that state could not be characterized as a solution, but only as a dry shell with a semi-liquid interior. A bulk solution analysis would apply in this case due to a nonlinear response of the calibration curve for solutions with such a high concentration.

The conclusion one can draw from these series of experiments is that using the Raman system to obtain information of particle chemical composition is a fairly accurate, reliable and repeatable process.

CHAPTER 2

FLYTRAP EXPERIMENTS WITH NITRIC ACID AND SEA-SALT AEROSOLS

2.1 Introduction

Because the Flytrap instrument acts as a wall-less container, it is an ideal platform for obtaining information on chemical and physical characteristics of individual suspended aerosols. Flytrap has been shown to be an extremely versatile instrument, capable of analyzing individually levitated aerosols in an environment where the ambient conditions can be well controlled (Chapter 1 of this work). Calibration experiments have shown that the suspended aerosols can be maintained in a variety of conditions and studied for time intervals spanning several days. Several sets of heterogeneous chemical interactions were studied using Flytrap. The first set of experiments dealt with the nature of HNO_3 interactions with artificially produced sea-salt aerosols in a variety of conditions. The second set of experiments dealt with looking at the oxidation of SO_2 within artificial sea-salt aerosols when they were exposed to O_3 as well as H_2O_2.

When examining the nature and behavior of heterogeneous chemistry problems, it is convenient to deconvolve the reactions into several discrete steps for the purpose of analysis. These steps include: (1) gas phase diffusion to surface of the aerosol, (2) accommodation to the surface, (3) diffusion within the liquid, (4) reaction with substrate or dissolved reactant and (5) diffusion of resultant products to the surface and expulsion from aerosol (Hanson et al., 1994). Heterogeneous chemistry reactions are usually broken down in such a manner so that rate-limiting steps may be determined and the calculated reactive uptake coefficients applicable to the atmosphere can be estimated in the absence of direct measurements under precise atmospheric conditions (Hanson et al., 1994).

Reactive uptake coefficients are usually understood to be the fraction of gas/solid or gas/liquid collisions that lead to a chemical reaction. These uptake coefficients are seldom measured under atmospheric conditions (Hanson et al., 1994). When accommodation and reactive uptake coefficients are measured in the lab, they are typically done using bulk solutions or solids as substrates for the reaction process. A key question to be answered is how well do the laboratory uptake measurements performed over thick, bulky substrates apply to atmospheric aerosols that are on the order of a micron in diameter. When reactive uptake coefficients are measured in the laboratory on thick planar substrates, the concentration gradient in the bulk solution of the recent gas-phase species may be large enough to result in a large measured uptake coefficient. The atmospheric uptake coefficient could however be much smaller, due to a smaller concentration gradient.

Before the first series of heterogeneous chemistry experiments using Flytrap was started, several estimates of the deconvolved steps involving reactive uptake were calculated in order to ensure that the instrument would be capable of making effective and relevant measurements. The first estimate was that of the time scale for gas-phase diffusion to establish a steady state profile around an aerosol in the trap. If an aerosol with a radius R_p is introduced into an environment containing a uniform mixing ratio of species A, then the characteristic time for gas-phase diffusion to establish a steady state profile around an aerosol can be described by scaling the diffusion equation. This scaling gives a characteristic time of

$$\tau_{dg} \approx \frac{R_p^2}{4D_g} \qquad \text{Equation 2.1}$$

where R_p is the radius of the aerosol and D_g is gas phase diffusion constant. According to the kinetic theory of gases, the diffusion constant is a function of pressure and temperature in that

$$D_g = \frac{1}{3}\lambda\bar{c} \qquad \text{Equation 2.2}$$

where λ is the mean free path of species A at a specific pressure and temperature, and c is the mean molecular speed of species A. An aerosol having a radius of ten microns subject to a species with a gas phase diffusion constant of 0.1 cm^2/sec has characteristic time τ_{dg} of 2.5×10^{-6} seconds. In dealing with changes on the order of minutes and hours, one can safely ignore the millisecond transition times and assume that the mixing ratio of species A is always steady state (Seinfeld and Pandis, 1998).

The gas-aerosol interface offers a resistance for mass transfer (Seinfeld and Pandis, 1998). The next estimate made was that of the characteristic time scale associated with establishing phase equilibrium at this interface. The goal was to determine the characteristic time for saturation of the droplet as governed by interfacial transport. For gases with a low solubility, this timescale can be approximated by

$$\tau_p \approx \frac{R_p^2}{\pi^2 D_{aq}} \qquad \text{Equation 2.3}$$

where R_p is the radius if the particle and D_{aq} is the aqueous phase diffusion coefficient of the species of interest (Kumar, 1989). Estimates indicate that the establishment of Henry's law equilibrium at the interface is a rapid process for both insoluble and soluble species alike with accommodation coefficients above 0.1. The timescale for SO_2, O_3, HNO_3 and NH_3 were estimated to be less than 1 second for typical atmospheric conditions.

Once the gas phase species is accommodated across the surface of the aerosol, many water-soluble molecules dissociate into ions. For example: nitric acid dissociates through reaction 2.4, leading to a decrease in pH of the aerosol.

$$HNO_3 \Leftrightarrow H^+ + NO_3^- \qquad \text{Equation 2.4}$$

Results of previous estimates by Seinfeld and Pandis (1998) of the characteristic time to establish such equilibrium are virtually instantaneous, well below one μs. Their results also indicate the timescale to establish equilibrium depends only weakly on pH. Therefore, for the sake of the

Flytrap experiments it was assumed that ionization equilibrium is achieved virtually instantaneously upon absorption of SO_2 and HNO_3 onto the droplet.

Considering the unsteady-state diffusion of a dissolved species through an aqueous aerosol, initially free of solute when the surface concentration is abruptly raised. The characteristic time for aqueous-phase diffusion in a droplet can also be *estimated* by

$$\tau_{da} = \frac{R_p^2}{\pi^2 D_{aq}} \qquad \text{Equation 2.5}$$

The timescale for aqueous-phase diffusion is also proportional to the square of the droplet radius. For an aerosol with a radius of 100 μm, the timescale for NO_3^- diffusion through the aerosol was estimated to be on the order of 1 second. For an aerosol with a 10 μm radius, the timescale was estimated to be 0.1 second. The important result of this estimate was that if the characteristic aqueous-phase diffusion time were much less than the characteristic reaction time, then aqueous-phase diffusion would be able to maintain a uniform concentration profile inside the droplet.

2.2 Background Information on HNO_3 / Aerosol Interactions

Sea-salt aerosols generated by wind and wave action in the marine troposphere should have chemical compositions similar to that of seawater, primarily NaCl with smaller amounts of other species (Kester, 1967). The ratio of chlorine to sodium is often less in aerosols than in seawater (Keene et al., 1990) and appears to be related to the presence of oxides of nitrogen in the atmosphere, which is consistent with the finding of excess nitrates in the aerosols. While nitrate may not account for all of the "missing" chlorine, it does represent a significant fraction (Laux et al., 1994).

To date, no important source for coarse mode particle nitrate is known to exist. Many research groups have however reported atmospheric nitrate in the coarse mode size range. The

explanation for the existence of these aerosols is that the nitrate in these samples must have been formed in situ or attached to pre-existing coarse mode particles. Nitrate particles in this size range may also be formed when gaseous nitrogen species such as HNO_3 interact with coarse mode particles (Pakkanen, 1996). The most important gaseous precursor for the nitrate aerosol is NO_x emitted from the combustion of fossil fuel. A significant part of this NO_x is transformed to gaseous nitrous and nitric acid in the atmosphere. Inspection of individual coarse particles has shown that nitrate is frequently found as a surface coating of atmospheric NaCl particles (DeBock, 1994). The reaction between sea-salt and acidic nitrate is expected to liberate HCl gas to the atmosphere leaving the particles enriched in nitrate and depleted in chloride (Eriksson, 1959). Nitric acid adsorbed onto a solid NaCl particle has the potential for acidifying the aerosol through the following mechanism

$$HNO_3(g) + NaCl(s) \rightarrow NaNO_3(s) + HCl(g) \qquad \text{Equation 2.6}$$

This reaction will hypothetically occur when maritime and polluted continental air masses mix in the boundary layer. If the ambient relative humidity is high, this reaction may take place in the aqueous phase (Pakkanen, 1996). Thermodynamic calculations indicate that the coarse sodium nitrate is stable under most atmospheric conditions and therefore represents a permanent removal pathway for nitrate (Yoshizumi and Hoshi, 1985). Other postulated acidification schemes involving nitrogen species and sea-salt aerosols include

$$2NO_2(g) + NaCl(s) \rightarrow ClNO(g) + NaNO_3(s) \qquad \text{Equation 2.7}$$

$$N_2O_5 + NaCl(s) \rightarrow ClNO_2 + NaNO_3(s) \qquad \text{Equation 2.8}$$

$$ClONO_2(g) + NaCl(s) \rightarrow Cl_2(g) + NaNO_3(s) \qquad \text{Equation 2.9}$$

The last three reactions produce photo-chemically reactive products which quickly photolyze in the troposphere to atomic chlorine (Laux et al., 1994). This chlorine may play a role in the fate of tropospheric ozone. In addition, atomic chlorine can abstract hydrogen from alkanes even faster than OH, leading to the formation of O_3 in the presence of NO_x (Finlayson-Pitts and Pitts, 1986).

These reactions however are only of minor importance however, if considerable amounts of nitric acid are present (Pakkanen, 1996).

In addition to being a removal pathway for nitrate, reaction (2.6) represents an important, but poorly quantified source of reactive chlorine to the marine boundary layer. The acid-base desorption mechanism described in reaction (2.6) will generate HCl, which is generally unreactive. Modeling investigations by Singh and Kasting (1988) suggest however, that if ppb(v) levels of HCl are generated by any mechanism in the MBL, reaction with the hydroxyl radical can produce sufficient reactive chlorine to photo-oxidize a significant fraction (~ 40%) of non-methane alkanes.

A variety of experiments have shown that the fraction of sea-salt aerosol chlorine that is released is variable and is a function of aerosol size, ambient relative humidity and the degree of local pollution. In the San Francisco Bay area for example, reaction (2.6) has been observed to entirely deplete smaller sea-salt aerosols of chlorine (Pakkanen, 1996, Martens et al., 1973). It should be noted however, that experimental artifacts due to reactions between acidified aerosols and sea-salt aerosols on typical collection media has a tendency to enhance the emission of gaseous inorganic chlorine. The *flytrap* instrument seemed to be an ideal platform for investigating the heterogeneous chemistry involved in reaction (2.6) without the introduction of significant artifacts.

In terms of mass, the five largest components of atmospheric aerosol are mineral aerosols, sea-salt aerosols, sulfates, biomass burning products and organics (Keene et al., 1998). Sea-salt aerosols, produced by breaking waves on the ocean surface, before dehydration, are thought to have a pH similar to that of surface sea-water (pH ~ 8). These aerosols, when injected into the atmosphere rapidly equilibrate with ambient relative humidities, thereby significantly decreasing in size. The results are small coarse mode aerosols with high ionic strengths and increased pH levels (Keene et al., 1998).

Fresh aerosols undergo what is thought to be rapid chemical transformation involving the scavenging of gases, aqueous-phase reactions and volatilization of products. The nature and rates of these transformations are thought to be strongly pH dependent and therefore will vary as a function of chemical and physical environment to which the aerosol is exposed between injection and removal. (Keene et al., 1998)

The chemistry of halogens such as Cl and Br is very dependent on pH. Aqueous aerosols with a neutral pH are expected to be a sink for HCl(g) (Keene 1990). Strong acids with low vapor pressure relative to HCl, such as H_2SO_4 and HNO_3 when accumulated in aqueous sea-salt aerosols are thought to titrate the alkalinity in the aerosol. When the pH of the aerosol drops below four, HCl should be volatilized outwards (Brimblecomb, 1988). The result is that HCl displacement is thought to substantially alter (buffer) the pH of acidified sea-salt aerosols. Even under heavily polluted conditions in which 75% of sea-salt chlorine is volatilized as HCl gas by acid displacement reactions, the modeled aerosol pH does not fall below 2 (Keene et al 1998).

HCl(g) is not the only gas that can escape from acidified sea-salt aerosols. Highly reactive halogen gases such as Cl_2, HOCl, $ClNO_2$, Br_2 and BrCl may volatilize also. Photolysis of these gases can produce atomic Cl and Br during the daytime. This has profound implications for ozone, methane, alkanes and DMS mixing ratios in the troposphere (Keene et al., 1990). However, most Cl in the atmosphere will react with non-methane hydrocarbons to produce HCl(g) which is fairly unreactive (Keene et al., 1990).

The reaction kinetics of HNO_3 with sea-salt crystals have been investigated but discrepancies exist in reported reaction probabilities (Laux et al. 1994, Leu et al. 1995, Beichert 1996). Additionally, the phase partitioning of gaseous HNO_3 and particulate nitrate in MBL reveals persistent discrepancies between thermodynamic equilibrium and observations. For typical sea-salt concentrations in the MBL, models predict that virtually all the HNO_3 will be rapidly scavenged out of the gas phase and converted to coarse particulate nitrate (Sander and Crutzen, 1996). In contrast, measurements of HNO_3 in the remote MBL reveal substantial

mixing ratios ranging from 10 to 100 pmol/mol (Singh et al., 1996). Based on thermodynamic and chemical properties, the aerosol pH must be less than 2 to sustain this HNO_3 mixing ratio. If the pH were this low, virtually all the Cl^- in the aerosol would be volatilized (Sander and Crutzen, 1996). This is inconsistent with measured Cl^- deficits over the open ocean (Graedel and Keene, 1995). Possible reasons for this include artifacts in measuring HNO_3. Measurements of HNO_3 in the MBL may exhibit substantial positive bias. It is thought that widespread use of prefilters to remove aerosols from the bulk from air upstream of both mist chamber and impregnated-filter sampling contribute to the post collection acidification of sea-salt by fine sulfur aerosols. This may displace HNO_3 in an analogous manner as HCl, thereby causing a positive HNO_3 artifact and a negative bias in the particulate NO_3^- measurement (Xiaohong et al., 2001).

Another reason for discrepancy between observation and models is that the thermodynamic data used in the models may be biased. Kinetic controls or the presence of surface coatings on the aerosols that slow gas exchange may also contribute to the discrepancy. The possibility exists also for some unidentified mechanism to maintain significant phase disequilibria of oxidized N in the marine boundary layer.

2.3 Background Information on Sea-salt Aerosols

Sea-salt aerosols are produced by turbulence at the air-sea interface and cycle on a time scale of hours to a few days in the marine boundary layer (Blanchard and Woodcock, 1957). Aerosols in the marine boundary layer are typically comprised of two distinct aerosol types: primary sea-salt aerosols and secondary non-sea-salt sulfates including some organic species (O'Dowd et al 1996). Most sea-salt aerosols are produced by bursting bubbles during the erosion of a whitecap, however, at high wind speeds there is direct production of larger sea-salt particles from shearing wave crests (Monahan 1986).

The particle size distribution is log-normal around a mean that increases with sea-salt concentration and turbulence at the air-sea interface. The typical marine aerosol spectrum spans more than five orders of magnitude in both size and concentration from 0.05 μm to 150 μm (Fitzgerald, 1991). The sea-salt number and mass distributions are strongly dependent on wind speed, typically adhering to an exponential relationship in the form of

$$\log C = aU_{10} + b \qquad \text{Equation 2.10}$$

where C is the concentration and U_{10} is the ten-meter height wind speed. The measurement of the complete sea-salt size distribution as a function of wind speed is somewhat difficult due to the large range of aerosol sizes. The difficulty is further compounded by the fact that aerosols with a large radius have very low concentrations (O'Dowd et al., 1996). Despite the decline in aerosol concentration with increasing radius, the larger sea-salt aerosols are usually present in sufficient concentration to dominate the total particulate surface area with a mode centered around 7 μm. Aerosols in the super-micron range also dominate the volumetric and mass distributions (O'Dowd et al., 1996).

Sea-salt aerosols are important in the global cycles of S, N and Cl, thereby influencing climatic processes (Posfai et al. 1995). A significant portion of S is removed from the atmosphere through oxidation of SO_2 in the water associated with sea-salt aerosols (Sievering et al., 1991; Chameides and Stelson, 1992). In the marine atmosphere, nitrogen-bearing species such as HNO_3 and NO_2 are also available for reactions with sea-salt (Huebert et al., 1996). These chemical reactions have the potential for releasing Cl into the atmosphere. The generation of sea-salt by turbulence at the air-sea interface is thought to be the major source of Cl in the Earth's atmosphere (Graedel and Keene, 1995).

Due to the conservative nature of the ions found in seawater, one would expect that aqueous sea-salt aerosols would have a similar chemical composition. Table 2.1 below lists the major ions found in seawater that has a salinity of 35 parts per thousand. In seawater, the pH is

mostly in the range of 8.0 ± 0.2 and variations in the pH are controlled through the following series of reactions

$$CO_2(g) + H_2O \Leftrightarrow H_2CO_3 \Leftrightarrow H^+ + HCO_3^- \Leftrightarrow 2H^+ + CO_3^{2-} \qquad \text{Equation 2.11}$$

These reactions are very rapid and seawater can be assumed to have an equilibrium mixture of the three ions. The alkalinity in the seawater is thought to be controlled mostly by the boron and carbonate ions. Before dehydration, freshly injected sea-salt aerosols are expected to have a pH similar to that of surface seawater: about 8 (Butler, 1982). A low pH value will push reaction 2.11 to the left, while large pH values will push it to the right.

Composition of sea-water

Ion	g/kg of water
Chloride	19.344
Sodium	10.773
Sulfate	2.712
Magnesium	1.294
Calcium	0.412
Potassium	0.399
Bicarbonate	0.142
Bromide	0.067
Strontium	0.008
Boron	0.004
Fluoride	0.001

Table 2.1: Chemical Composition of Sea-water with 35 0/00 salinity (Libes, 1992)

Aerosols will rapidly equilibrate to the ambient relative humidity, resulting in decreasing size, increased ionic strength and increased pH. Because the relative humidity in the marine boundary layer is typically greater than the deliquescent point for NaCl (about 75%), sea-salt aerosols usually exist as concentrate droplets of ionized salts. Fresh aerosols will undergo chemical transformation involving the scavenging of gases, aqueous-phase reactions and the volatilization of products (Chamedies and Stelson, 1992; Sander and Crutzen, 1996). The nature and rates of many of these transformations are strongly pH dependent and therefore are thought to

vary as a function of the chemical and physical environment to which the aerosols are exposed (Keene et al., 1998).

2.4 Nitric Acid Vapor Delivery System

In order to examine the nature of coarse-mode nitrate formation in sea-salt aerosols, a system to deliver a well-characterized flow nitric acid vapor to the quadrupole trap was developed. The easiest and most effective method for doing so involved a simple system, which allowed "zero air" to flow through a temperature controlled oven that contained an HNO_3 permeation tube. An illustration of the final flow system used to deliver HNO_3 vapor to the trap is given below in figure 2.1.

Flow rate 1 (fr1) in the diagram below refers to the zero air flow through the permeation oven. For this series of nitric acid experiments, the flow rate was set at 150 cm^3 / min. The oven temperature was run at a nominal 35°C. It should be noted that all connectors downstream of the permeation oven were made of Teflon so that the loss of HNO_3 vapor would be minimized. The flow from the oven was then diluted with another zero air source, labeled "fr 2" below. This dilution air could be set anywhere from 0 to 4 liters per minute. This volume of air was far too great for an aerosol in the trap to withstand. As a result, most of this air was exhausted to a dump. A small portion of this air (usually 5 cm^3 / min, controlled with a Teflon valve) was mixed with air from the relative humidity system. The humidified, HNO_3 laden air was then directed to the entrance orifice of the trap, where it was free to interact with a suspended aerosol.

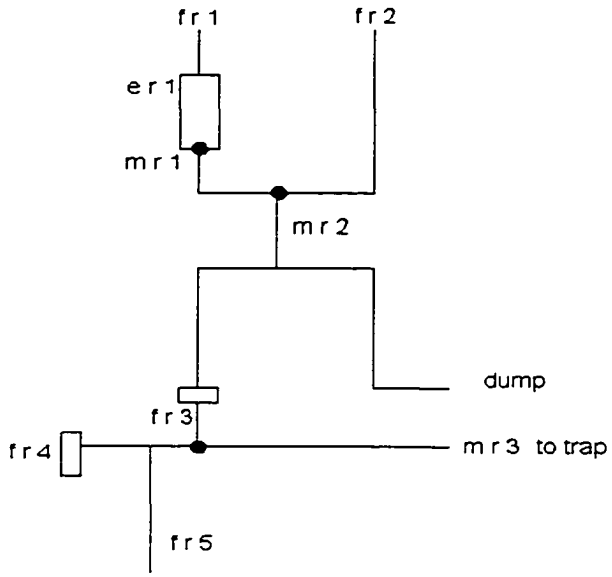

Figure 2.1 Flowchart of the HNO_3 and water vapor delivery system.

Kintecs provided the permeation tube used in this system. The certificate of calibration stated the emission rate of HNO_3 from the tube was 1490 nanograms per minute at a temperature of 40°. This emission rate proved to be too large for use in the flytrap experiments. As a result, the temperature of the oven was reduced to 35°C, with a subsequent reduction in the emission of HNO_3 from the tube. The emission rate (er 1) of the permeation tube for a given temperature was carefully calibrated with the use of nylasorb filters and a HPLC system. In a typical calibration run, a nylasorb filter was placed downstream of the oven for fifteen minutes. The filters were then removed and a nitrate extraction performed. The nitrate amounts were then quantified with a high-pressure liquid chromatography (HPLC) system. In addition to filters collecting HNO_3, many blank filters were also run. The mixing ratio of nitric acid at "fr3" was measured several times throughout the nitrate experiments.

Using this system, an air stream with a relative humidity between 10% and 90% and a HNO_3 mixing ratio between 20 and 200 ppb(v) could be directed to the trap orifice. The flow rates were large enough to minimize the loss of HNO_3 to the walls of the system, and small enough to ensure the aerosol was not pushed out of the trap through stokes forces or turbulence.

2.5 Dry NaCl Particle Experiments

An experiment was conducted to determine the magnitude of the reaction probability between HNO_3 vapor and a solid (dry) NaCl aerosol suspended in the quadrupole trap. Knowledge of the reaction probability is important; if the reaction is fast, it may overwhelm contributions of reactions 2.7, 2.8 and 2.9 and lessen the likelihood of chlorine atom production via these mechanisms (Laux et al., 1994).

To execute this experiment a solution consisting of 90.0 grams of ultra-pure, de-ionized water and 5.0 grams of NaCl was mixed. The solution was then pipetted into the tip of the microparticle injector. The subsequent aerosols were then charged via induction and stopped in the quadrupole trap. The voltages on the trap were adjusted such that only one aerosol remained.

The relative humidity in the trap chamber was raised above the deliquescent point to 90% at which point Raman spectra of the hydrated NaCl droplet was obtained to check for any prior HNO_3 contamination. The relative humidity in the chamber was then slowly brought down to 10% allowing the aerosol to dry slowly into a roughly spherical shape. The aerosol was allowed to "dry" for seventeen hours by subjecting it to a stream of zero air, ensuring that very little water was in or on the surface of the aerosol. A Raman spectrum of the dry aerosol was obtained to look for any residual trace of an H_2O peak in the spectrum. The size of the dry salt aerosol was then measured with the Mie scattering apparatus and determined to have a radius of 5.0±0.5 μm. The particle mass was determined be 2.3±0.4 nanograms by using the balance voltage method described earlier in chapter 1.

Once the initial mass and aerosol radius was obtained, the aerosol was subjected to a stream of zero air and nitric acid vapor at a mixing ratio of 36±6 ppb(v) at a temperature of 298K. The system for delivering this gas mixture to the trap is described above in section 2.4. The radius and balance voltages were measured every ten minutes for a total of five hours. During

this five-hour time interval, there was **no measurable mass change of the aerosol.** A Raman spectrum of the dry aerosol showed no detectable trace of nitrate or water. (This does not mean that nitrate was not present, the signal from a dry aerosol is very noisy and interpretation of the results is difficult to perform.) The aerosol was then hydrated above the deliquescent point for NaCl, and another Raman spectrum was obtained. A very small nitrate peak was observed at 1050 cm^{-1}, only slightly above Raman system detection limits. This spectrum is shown in figure 2.2 below. The measured nitrate molarity of the hydrated droplet was measured to be 0.024±0.008 M.

Once the molarity of the hydrated droplet was measured, the reaction probability between HNO_3 vapor and NaCl could be calculated using

$$\frac{d[NO_3^-]}{dt} = \phi A[G]\sqrt{\frac{RT}{2\pi M}} \qquad \text{Equation 2.12}$$

where ϕ is the reaction probability, A is the surface area of the aerosol, and G is the mixing ratio of the gas species with molecular weight M (Laux et al., 1994). Using the Raman spectra (shown if Figure 2.2) and the corresponding timing measurement, the time rate of change for the nitrate concentration was estimated. From Equation 2.12, the reaction probability between HNO_3 vapor and dry NaCl was estimated to be

$\phi = (2.5 \pm 0.8) \times 10^{-4}$

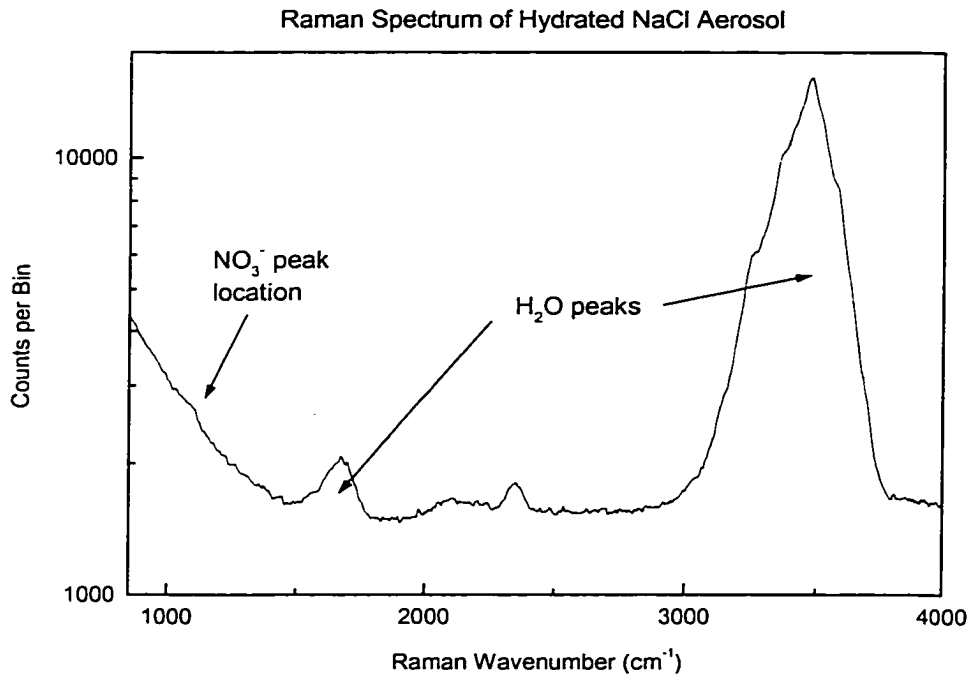

Figure 2.2 Raman spectrum of NaCl aerosol that, as a dry aerosol had been subjected to a stream of nitric acid vapor for 5 hours. The particle was re-hydrated in order to obtain a measurement of nitrate molarity.

The result reported above of the reaction probability between HNO_3 vapor and NaCl crystals should be treated as an upper limit estimate at best. When the experiment was repeated for time intervals of 2.5 and 1.0 hours, no detectable nitrate signals were observed. The uncertainty in the measurement was primarily the result of the sensitivity of the Raman system to the nitrate signal. Aside from a small measured nitrate signal after the salt aerosol was hydrated, no change to the aerosol during exposure to HNO_3 vapor (36 ppbv) was observed.

One of the conclusions drawn for the result of this experiment was that only the surface of the dry NaCl aerosol reacted with the HNO_3 vapor to produce a thin coating of solid $NaNO_3$. The diffusion of HNO_3 through solid aerosol was far too slow to react with much of the interior NaCl. If the chlorine ions in a dry NaCl aerosol (with a mass of 2.3±0.4 nanograms), were entirely replaced with NO_3^- ions, the mass should be observed to change to approximately 3.3

nanograms; something easily measurable using the balance voltage method described in Chapter 1. Because no such change in the balance voltage was measured during the course of the experiment, it was assumed that the mass change of the aerosol was below 0.4 nanograms. Another reason to treat this measurement as an upper limit on the reaction probability is that there was no convenient method for distinguishing between nitrate ions that were merely adsorbed onto the surface of the NaCl aerosol as part of the HNO_3 vapor, and those that participated in a reaction similar to that of equation 2.6.

Laux and Hemminger (1994) determined that the reaction probability for reaction 2.6 was $\phi = (4\pm2) \times 10^{-4}$ using an X-ray photoelectron spectroscopic technique. Their results were the first reported reaction probability measurement for reaction 2.6. It was found to be one to two orders of magnitude slower than the corresponding reaction involving N_2O_5. It was suspected that the reaction kinetics of 2.6 were extremely phase-dependent. In the marine boundary layer, the relative humidity is usually higher than the deliquescent point for NaCl aerosols. The diffusion of products and reactants involved in reactions 2.6 – 2.10 should proceed orders of magnitude faster though an aqueous phase than through a solid (Laux et al., 1994). As a result the reactive uptake of HNO_3 by deliquescent NaCl aerosols was investigated. These experiments are described and discussed in the next section.

2.6 Aqueous-Phase Aerosol Experiments

As mentioned previously, ozone mixing ratios in the troposphere are highly affected by NO_x and nitric acid (the main NOx reservoir species). This is because ozone is thought to be formed by a complex series of photochemical reactions involving nonlinear interactions with NO_x (Goodman et al., 2001), (Seinfeld and Pandis, 1998). Current atmospheric chemistry models cannot reconcile the difference between observed and predicted mixing ratios of HNO_3 and NO_x. The models tend to overestimate the HNO_3 to NO_x ratio by a factor of 5-10 (Goodman et al, 2001). A possible reason for this discrepancy is thought to be that the HNO_3 mixing ratios are over-predicted in atmospheric chemistry models. The discrepancy may also be potentially due to an important and yet unknown chemical pathway involving the heterogeneous removal of HNO_3 from the atmosphere (Singh et al., 1996), (Thakur et al., 1999).

When interactions between nitric acid vapor and aerosols are not limited to the surface of the aerosol, the potential to remove vast quantities of nitric acid from the vapor phase may be substantial. Several studies on the heterogeneous removal of HNO_3 on cirrus clouds, aerosol surfaces, sulfate and soot have been performed. Modeling indicates that these removal processes are not significant enough to reduce the HNO_3/ NO_x ratio when included in global chemistry models (Tabazadeh et al., 1998, 1998; Wang et al., 1998). Heterogeneous pathways may provide significant nitric acid vapor removal, especially if the nitric acid is not limited to the surface of the aerosol. This has the potential to substantially alter (reduce) the HNO_3/Nox ratio in the atmosphere. To this end, the flytrap was used to investigate the heterogeneous removal of HNO_3 by sea-salt aerosols in an aqueous phase with varying amounts of initial alkalinity.

2.6.1 Calibration and Experimental Setup

To determine the concentration of NO_3^- ions in hydrated sea-salt aerosols, a bulk calibration curve was created. This procedure is very similar to that described in chapter 1. Mixed solutions of varying concentration of $NaNO_3$ were placed in a cuvette and Raman system

response was measured. For each mixture, the counts underneath the water and nitrate peaks were measured using a strict numerical counting method. The procedure for finding nitrate concentration in droplets was treated exactly in the same manner as for the calibration curve. The nitrate feature used was the 1050 cm^{-1} line and the water features were the peaks located between 3000 and 4000 cm^{-1}. The curve shown below in figure 2.3 was the result of the calibration. A linear regression to the data showed that the relationship between peak counts ratio to concentration was

$$y = (26.9 \pm 0.1)\, x + (0.01 \pm 0.01) \qquad \text{Equation 2.14}$$

with a correlation coefficient of 0.99. It should be noted here that making continuous radius (hence volume) measurements was much easier than making continuous mass measurements. Therefore, the nitrate calibration was done using molarity concentration units and not molality.

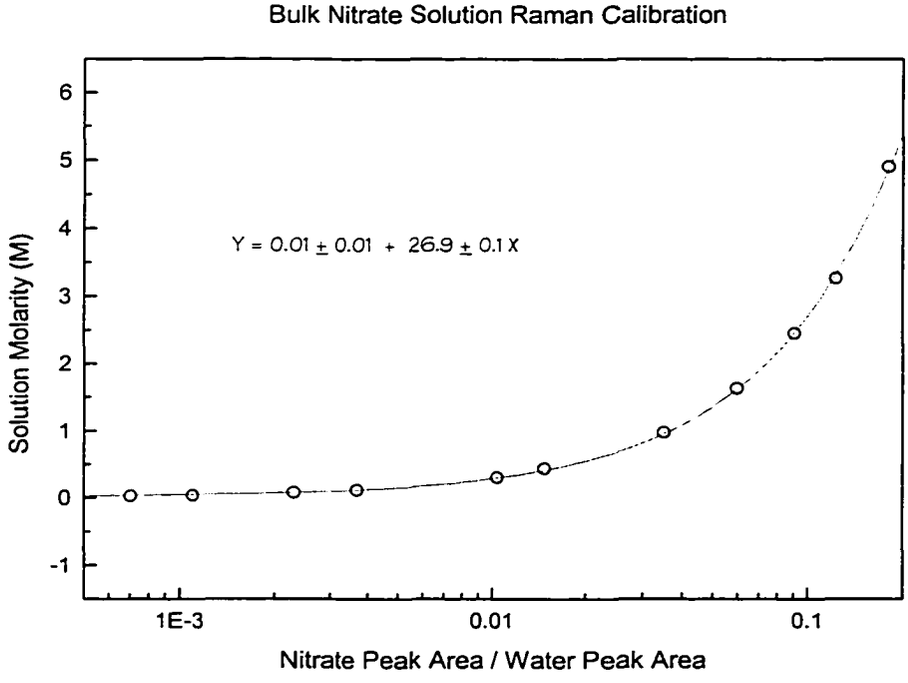

Figure 2.3 Bulk calibration curve for nitrate ions. $NaNO_3$ was used as source of nitrate ions. The regression coefficient was determined to 0.99.

Similar calibrations were attempted using nitric acid as a nitrate source. The results were extremely similar for acid concentrations less than 5 M. Above this level, the relationship between peak areas and solution concentration became non-linear. Peaks other that those for NO_3^- started to appear in the spectrum. (Specifically the H – NO_3 1390 cm^{-1} peak appeared and was dependent on the pH of the solution). This Raman feature could prove to be potentially valuable in determining droplet pH levels.

The experimental setup used in the aqueous phase experiments was very similar to that described in section 2.5. The only difference was the relative humidity system was set to keep the trap chamber at 90% RH instead of 0% RH.

2.6.2 Obtaining the Data

One of the first heterogeneous chemistry experiments performed involved determining if the conversion of HNO_3 to $NaNO_3$ in an aqueous-phase aerosol was a permanent removal pathway for nitrate (see reaction 2.6). To this end a solution of 80 gm pure water with 5 gm $NaNO_3$ was prepared. The solution was pipetted into the microparticle injector fluid reservoir. The induction ring was attached and a charged droplet was then injected into the trap. The chamber was held at a relative humidity of 90% and Raman spectra of the droplet were obtained to verify the presence of nitrate. The chamber relative humidity was then slowly brought down to 10 %, well below the deliquescent point for $NaNO_3$. The particle was left overnight to dry thoroughly. After seventeen hours, the particle was re-hydrated at 90 % RH and a Raman spectrum obtained. The size, mass and radius of the re-hydrated aerosol were the same as the previous day (within experimental error). The concentration of nitrate was also the same, verifying that $NaNO_3$ is not a volatile substance, and the conversion of HNO_3 to $NaNO_3$ is a permanent removal pathway for nitrogen in the atmosphere.

The next series of flytrap experiments dealt with hydrating sea-salt aerosols and examining the time rate of change of the nitrate concentration when they were subjected to a large mixing ratio of nitric acid vapor. Developing protocols for this type of experiments proved to be difficult and time consuming. Methods were needed for injecting, hydrating and immobilizing aerosols under conditions that simulated the marine boundary layer.

It was determined by trial and error that the amount of NaCl in preparing the solution pipetted into injector controls the ultimate size of the hydrated aerosol. Large concentrations of NaCl in the bulk solution usually yielded aerosols that had large diameters in the trap when the relative humidity was increased from 25% to 90%. As a result of the hygroscopic behavior of NaCl, the masses of the aerosols injected into the trap usually increased by a factor of two to four after being hydrated to a RH of 90%. The initial charge needed for trapping the aerosols before they were hydrated were enormous, usually on the order of 250,000 electron units of charge. This was not an easy task, even for the microparticle injector induction ring.

In order to keep the aerosols hydrated, the tube supplying the air and nitric acid vapor had to be positioned directly over the orifice of the trap. Large voltages on the trap AC ring had to be maintained (~600 volts) in order to keep the more massive hydrated aerosols balanced, especially when humid air and nitric acid vapor were flowing over the surface giving rise to large Stoke forces. These large voltages on the trap implied a need to keep the trap immaculate, and free of salt residue. Otherwise, salt particles (from previous injection attempts) became charged and would sometimes fly into the center of the trap, colliding with trapped particles. Failed attempts to trap a particle after few seconds of injector time required that the trap be removed, disassembled, cleaned and polished with methanol and de-ionized water, dried and reassembled.

While aerosols (usually latex spheres and dry salt particles) have been kept in the trap for periods of days, running the relative humidity system for this period required constant attention. While the aerosol was being hydrated or dehydrated, the balance voltage was constantly adjusted

so the trap endcap electrodes didn't pull it out of the potential well. The upper time limit on this type of particle management was 6-8 hours at most.

When emitted from the microparticle injector, the aerosols were fully hydrated. They quickly equilibrated to the relative humidity found in the lab, meaning a large portion of the aerosol evaporated in a matter of seconds. The charge on the aerosol was however a conserved quantity. If the electrical driving force on the small aerosol was too great to keep it in trap: the shrinking aerosol was quickly and violently flung out of the trap center. Trying to trap an ideal particle sometimes lasted all day. Once a suitable aerosol was injected, it was allowed to "dry" for twelve to twenty-four hours, such that the radius and balance measurement yielded a correct NaCl mass.

Once hydrated, the larger aerosols were subjected to significant thermophoresis and photophoresis effects, moving the aerosol sometimes close to 500 microns from the center of the trap and out of alignment with the Raman system optics. This required that the Raman system optics be realigned every several hours of operation and again with every new particle injected into the trap. One solution to the thermophoresis problem was to open the slit width to the Raman monochromator to 300 microns. The spectral resolution of the instrument then was reduced to an unacceptable level.

Trapping suitable NaCl aerosols for heterogeneous chemistry experiments proved to be a difficult task. When the small (~3 um), dry, highly charged NaCl aerosols were subjected to relative humidities near 90%, they became more massive with larger radii (~10 μm). A goal was then to pick an HNO_3 mixing ratio bracket such that a time-interval of less than six hours gave a detectable nitrate signal in as small an aerosol as possible. The nitric acid delivery system and humidified air were mixed in such a way as to deliver the flow right over the center of the trap, simulating an "open" system. Recirculating the air throughout the trap chamber proved to be inadequate for experimental needs. The aerosols took far too long to rehydrate and the nitric acid stuck to the walls of the trap as well as the trap chamber, making the mixing ratio measurements

uncertain. The flow of gases was adjusted by lowering the flow tube carrying these gases slowly downwards until the increased Stokes forces pushed the particle in the trap gently downwards. This method of addition gas delivery made continuous balance voltage measurements very difficult: not only were gravitational forces to be countered, but the aerodynamic Stokes forces as well. The mixing ratio of nitric acid that gave a detectable nitrate signal in less than six hours was experimentally determined to be 36 ppb(v).

The first aerosol used for heterogeneous kinetic nitric acid uptake studies was created from a mix of 5 grams pure NaCl with 80 grams of water. The solution was pipetted into the microparticle injector. It was then possible to inject a highly charged aerosol into the quadrupole trap. When charged and dry, the resultant NaCl aerosol was not too small (~7 μm). When the aerosol was hydrated at an RH of 90% it was not too large. Once the particle was well ensconced in the trap, the RH was lowered from 90% to 10% slowly. This allowed the aerosol to dry into a spherical shape, from which a Mie spectrum could be obtained. The radius and balance voltage were observed and thereby the aerosol charge and mass were estimated. The aerosol was then hydrated to 90% where the radius and mass were measured again. The aerosol (dry) radius was measured to be 6.3±0.8 μm with a dry mass of (3.0±0.5) nanograms. The charge on the aerosol was determined to be 220,000 excess electrons. At this point in the experiment, the aerosol just consisted of NaCl and water, but the aerosol was very well characterized. The radius, salt mass, water mass, salt volume, water volume and total aerosol charge were known. A characteristic MathCad worksheet detailing the methods of these calculations is given in the appendix.

The aerosol was then subjected to a nitric acid mixing ratio of 200±20 ppb(v) of HNO_3. Periodic Raman measurements were made with exposure time of two minutes each. Periodic radius measurements were made with the Mie scattering camera. Several of the Raman spectra are shown in figure 2.4 below.

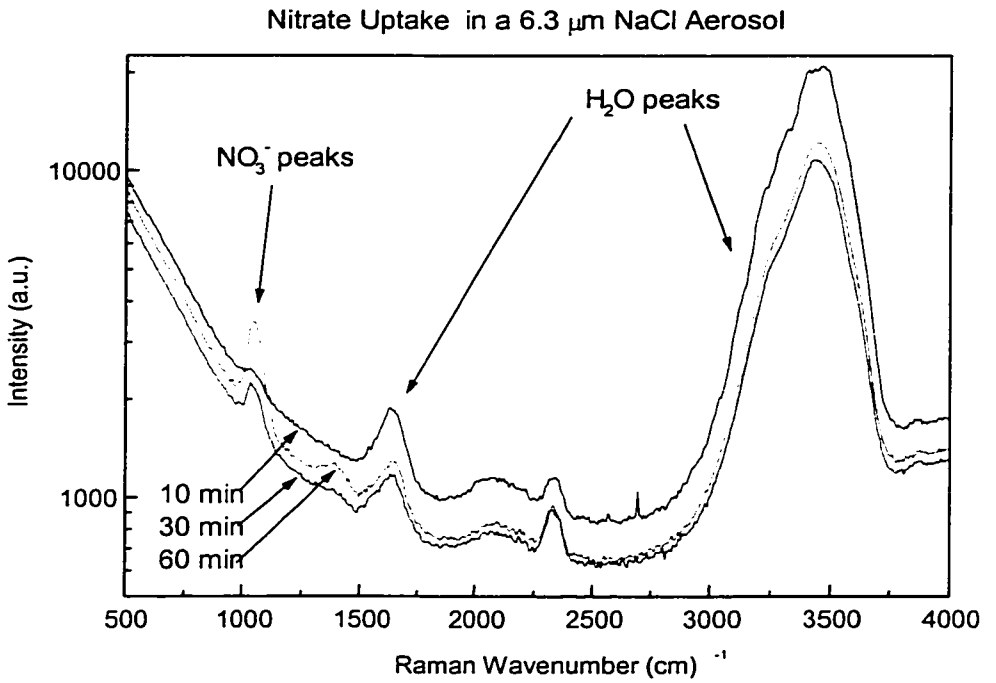

Figure 2.4 Time evolution of Raman spectra for NaCl aerosol subjected to HNO_3 vapor for 1 hour. Clearly visible are the growth of nitrate peaks at 1050 cm-1, and a decrease in size of absolute intensity for water peak.

Several things are apparent from this plot, the first being the obvious and easily identifiable growth in the nitrate peak at 1050 cm^{-1}. The second and not so obvious result was the decrease in the water signal as a function of time. This behavior had been observed with many test aerosols before this one. From the Mie scattering data, a measure of the particle radius, there is an obvious decrease in the radius of the aerosol as more nitrate is adsorbed. The explanation of this decrease lies in the fact that $NaNO_3$ is much less hygroscopic than NaCl. As the nitrate ion displaces the chlorine, the thermodynamics of the system necessitates the release of H_2O vapor to maintain equilibrium. An analysis of the thirteen Raman and Mie spectra obtained during this experiment yielded the following results. The number of moles needed to saturate the aqueous aerosol was calculated from the amount of water (measured) and the mixing ratio of nitric acid (set to be 200 ppb(v)). Knowledge of the radius of the aerosol and the molarity of nitrate in

solution yielded the amount of nitrate in the aerosol. The initial amount of chlorine in the aerosol was measured from the mass of the NaCl in the dry aerosol. An example of the MathCad worksheet used for these calculations is given in the appendix. It should be noted here that making continuous radius (hence volume) measurements was much easier than making continuous mass measurements. Therefore, the nitrate calibration was done using molarity and not molality.

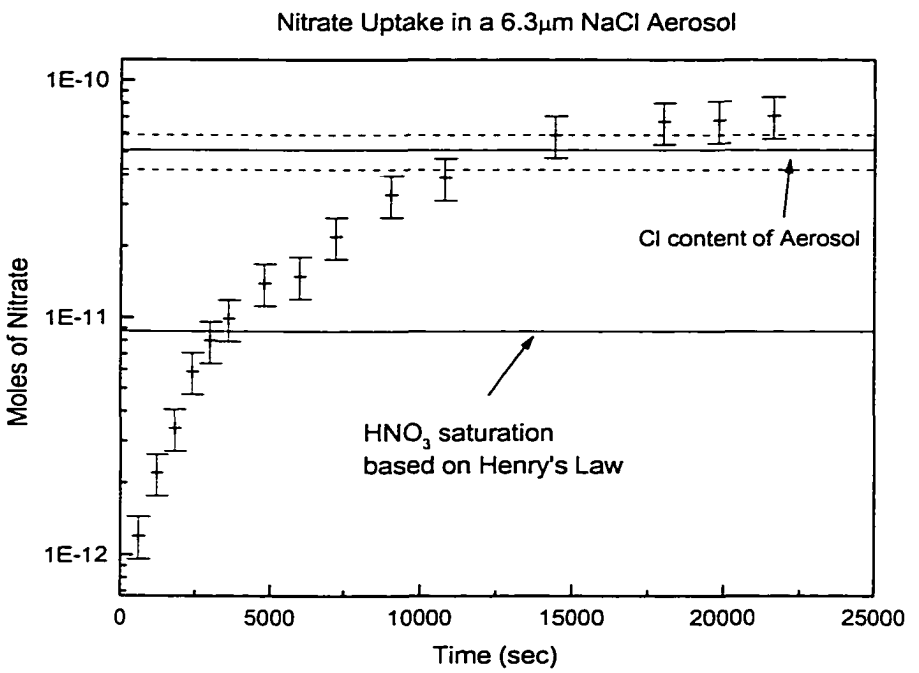

Figure 2.5 Nitrate uptake by a large sea-salt aerosol. Raman spectra from 6 hours of data were analyzed for this plot. The HNO_3 mixing ratio was set at 200 ppbv.

It is obvious from figure 2.5 that the hydrated NaCl aerosol quickly reaches the saturation level as calculated from the application of Henry's Law. It took nearly four hours of exposure to nitric acid vapor to reach nitrate levels that would be expected to completely deplete the aerosol of chlorine. The rate of nitrate uptake slows as the concentration reaches the original level of chlorine concentration in the aerosol.

A more complete discussion of the dechlorination mechanism kinetics is presented in section 2.8, following a detailed analysis of the data. Briefly, however, it is proposed that the H^+ ions from the dissolution on HNO_3 are combining with Cl^- ions present from NaCl dissolution. The created HCl(aq) in the aerosol quickly diffuses to the droplet interface and escapes as HCl(g) into the surrounding air due to the partial pressure of HCl(g). The effect is to remove H^+ ions from solution, thereby raising the pH of the droplet that allows a bit more HNO_3 to be accommodated at the aerosol surface.

This type of experiment was repeated several times (but with the HNO_3 mixing ratio reduced to 36 ppb(v)) for aerosols of several different sizes. Again, nitrate signals as functions of time were measured with the Raman system and radius were measured with the Mie scattering CCD camera. While the results of only four aerosol experiments are reported, thousands of attempts at injecting and trapping "ideal" particles were made. Hundreds of these aerosols were trapped. Many of these aerosols "fell out" due to management problems during hydration or they collided with other particles in the trap. (A good indicator of a problem such as this was the inexplicable change in the aerosol balance voltage). Many other aerosols would vanish during the course of taking a Raman spectrum, while others would be pushed out of the trap due to large thermophoresis effects.

The goal of this experiment was to obtain information on the reactive uptake coefficient for nitric acid on aqueous sea-salt aerosols. The two parameters to vary to determine this were the aerosol radius and the nitric acid mixing ratio. For this experiment, it was easier to keep the nitric acid mixing ratio constant and allow aerosol diameter to vary from particle to particle (as it would anyway – trying to get aerosols of identical diameters on demand proved to be nearly impossible.) The results of the experiments are shown graphically in figures 2.6, 2.7 and 2.8 on the following pages.

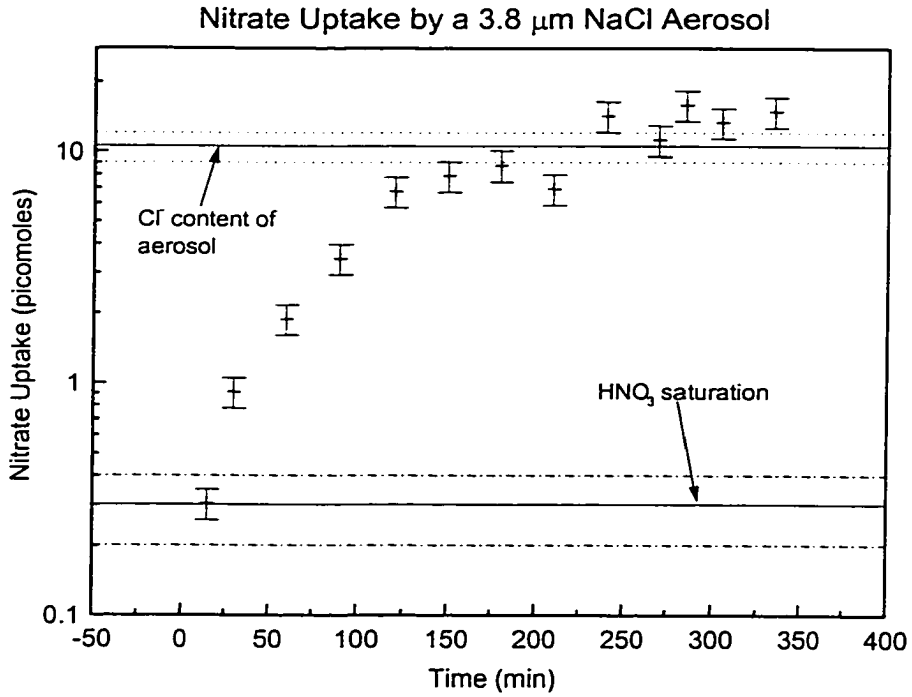

Figure 2.6 Nitrate uptake by a small (3.6 μm) hydrated NaCl aerosol. Raman spectra from 6 hours of data were analyzed for this plot. The HNO_3 mixing ratio was set at 36 ppbv while the relative humidity of the trap chamber was at 87%. The HNO_3 saturation level based on Henrys Law is given for comparison.

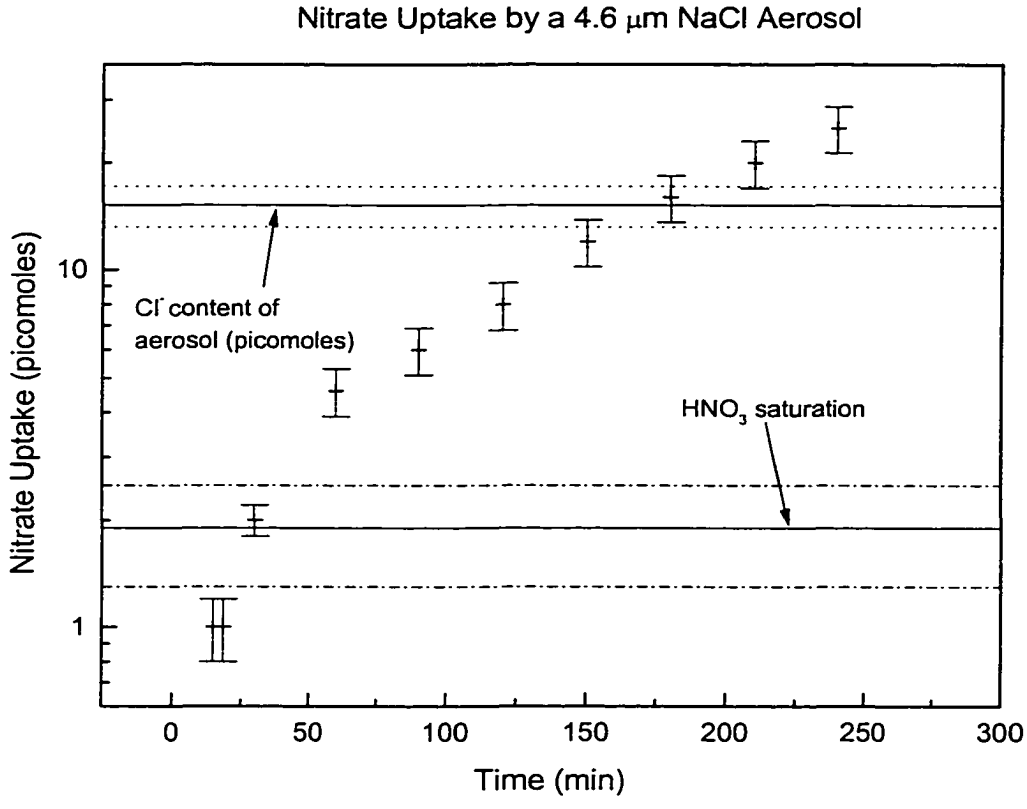

Figure 2.7 Nitrate uptake by a 4.6 μm hydrated NaCl aerosol. Raman spectra from 4 hours of data were analyzed for this plot. The HNO_3 mixing ratio was set at 36 ppbv while the relative humidity of the trap chamber was at 87%.

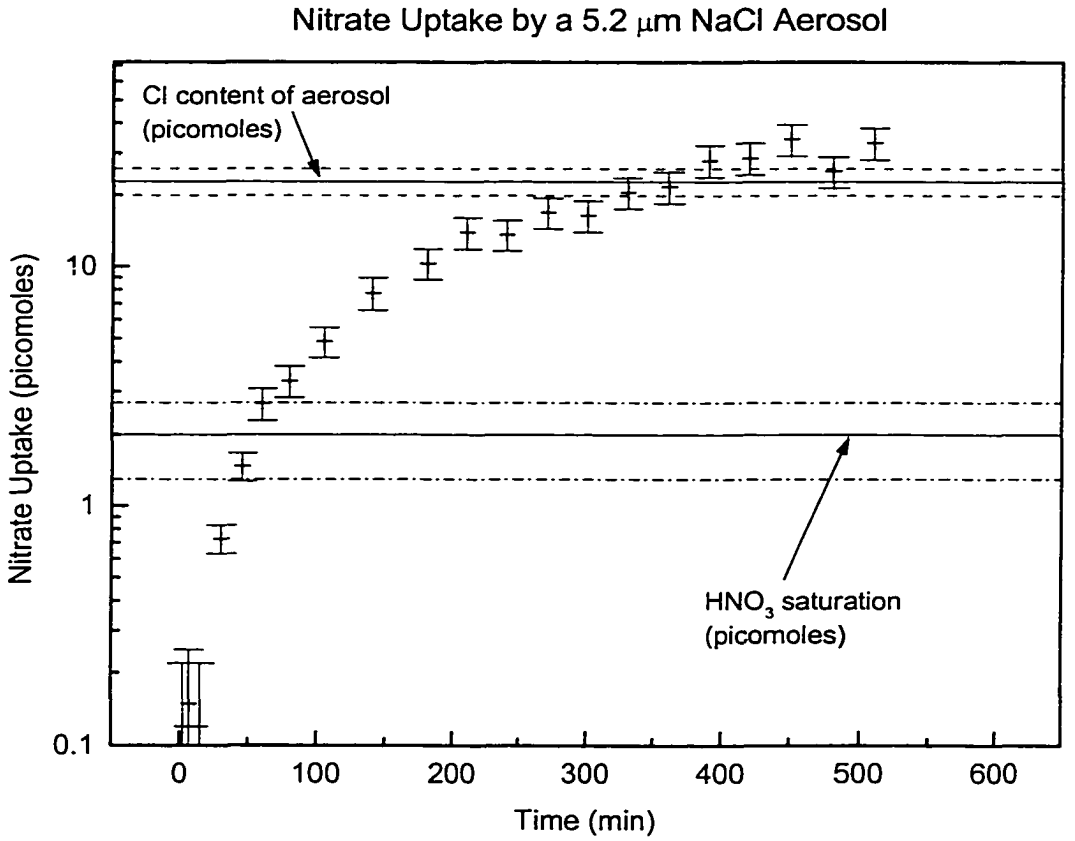

Figure 2.8 Nitrate uptake by a large (5.2 μm) hydrated NaCl aerosol. Raman spectra from 8 hours of data were analyzed for this plot. The HNO_3 mixing ratio was set at 36 ppbv while the relative humidity of the trap chamber was at 87%.

It is obvious from figures 2.6, 2.7 and 2.8 that the hydrated NaCl aerosols quickly reach the saturation level as calculated from the application of Henry's Law. It took nearly four to six hours of exposure to nitric acid vapor to reach nitrate levels that would be expected to completely deplete the aerosols of chlorine. The rate of nitrate uptake in each aerosol slows as the concentration reaches the original level of chlorine concentration. The nitrate amount (in picomoles) is displayed on a $\log_{10}$ axis due to the large variation in nitrate concentrations (nearly three orders of magnitude).

The nitrate amount (in picomoles) was calculated from measurements of nitrate concentration (M) and aerosol radius. In this series of applications it was much easier to measure the aerosol radius than it was the aerosol mass. The error bars on the nitrate moles were calculated by propagating the uncertainty in the aerosol radius through the concentration calculation. This had the unfortunate effect of placing larger nitrate amount uncertainties on aerosols with a larger nitrate concentration, even though the nitrate Raman signal was more prominent in these aerosols. Further analyses of these results were performed. A discussion of this effort is provided below.

2.6.3 Reactive Uptake Coefficient Calculations

For heterogeneous reactions, the uptake of a gas on a solid is most often expressed in terms of an uptake coefficient or a reaction probability γ. The reaction probability can be defined as

$$\gamma = \frac{\frac{dNO_3}{dt}}{Flux \times Area} \qquad \text{Equation 2.15}$$

where the numerator represents the observed time rate of change of nitrate in or on the surface (or volume) of the aerosol, and the denominator represents the flux of nitric acid vapor to the surface of the aerosol. The flux of nitric acid to the aerosol surface can be estimated with the following expression according to kinetic gas theory:

$$Flux = \frac{PN}{\sqrt{2\pi MRT}} \qquad \text{Equation 2.16}$$

where P is the partial pressure of HNO_3, N is Avogadro's number, M is the molecular weight of nitric acid, R is the gas constant and T is the temperature of the gas. From the data of nitrate uptake as a function of time, it was a straightforward task to compute (dNO_3 / dt) for each data point. The flux of nitric acid was dependent only on the mixing ratio of nitric acid and the

surface area of the aerosol. The reactive uptake coefficient was calculated as a function of time for each aerosol. The results of the 6.3 μm NaCl aerosol are shown in figure 2.9 below. The average reactive uptake coefficient γ, was (2.5±0.7) x 10^{-3}, nearly an order of magnitude higher than that found for a **dry** NaCl aerosol. The time dependence of γ was a surprise. Each of the four aerosols examined in this series of experiments displayed exactly the same time of behavior for γ(t). The uptake coefficients were small at the start, reached a maximum and then as the nitrate reached a maximum (or chlorine depleted as it were) the value for γ decreased to a minimum, usually zero within experimental error.

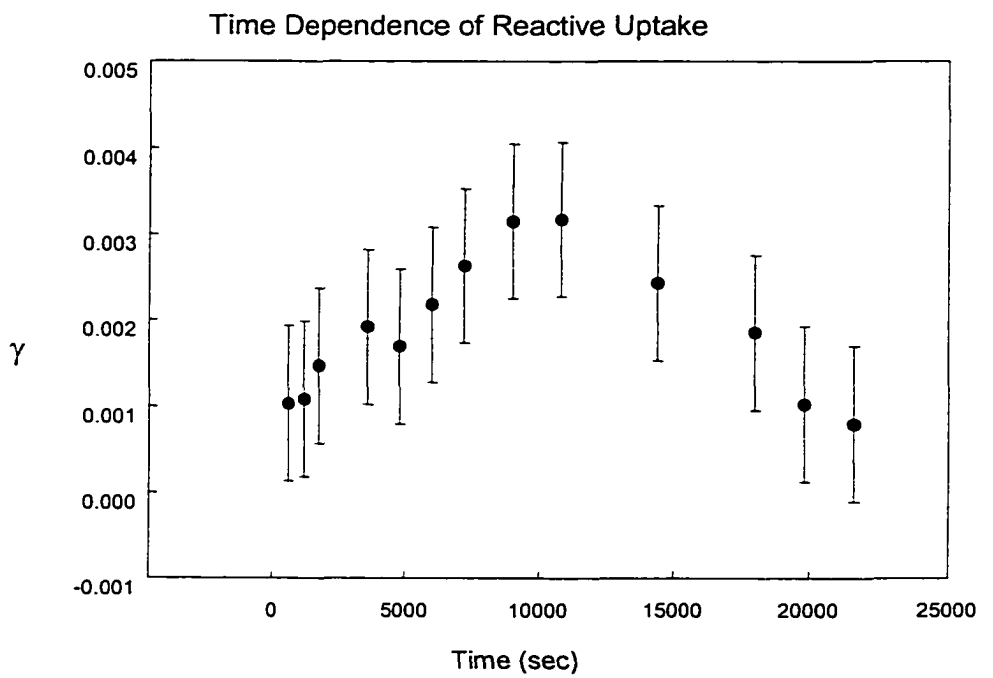

Figure 2.9: Determination of γ as function of time for the 6.3 μm NaCl aerosol.

A plot of γ(t) vs. nitrate concentration (also a function of time) was created from the same data set. The curve is shown in figure 2.10 below. It was thought that displaying γ as a parametric function of another droplet property would shed some understanding on the γ time

dependence. Ideally, a plot of γ as a function of droplet pH and Cl content would be more illuminating. Several nitrate and sulfate properties displayed in the Raman spectra are pH dependent and were seen in the bulk phase experiments. For example, in bulk phase experiments the ratio of the 1390 cm^{-1} peak height to the 1050 cm^{-1} peak height increased as the pH of the solution decreased. Unfortunately the pH characteristics of the aerosols were unable to be measured in this manner due to a low 1390 cm^{-1} signal.

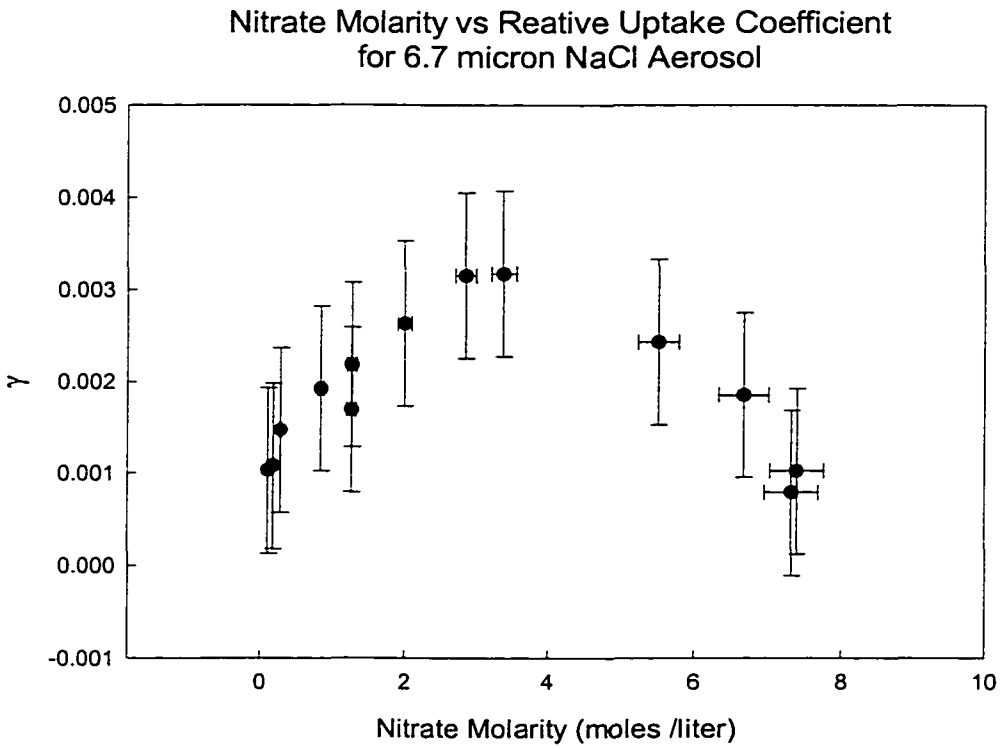

Figure 2.10: γ as a function of droplet nitrate concentration (M). This data was derived from the experiment involving a 6.7 μm aerosol when the nitric acid vapor mixing ratio was set at 36 ppbv.

The data generated from the different aerosols was examined collectively to illuminate the effect of radius on the reactive uptake parameter. The data from the first four hours of each aerosol data was plotted and the slope of the NO_3^- (moles) vs. time plot was found with a

minimized chi-square fit to a straight line. This slope was then used in the calculation of the time-averaged γ value for each aerosol according to equations 2.15 and 2.16. An example of the fit is shown below in figure 2.11.

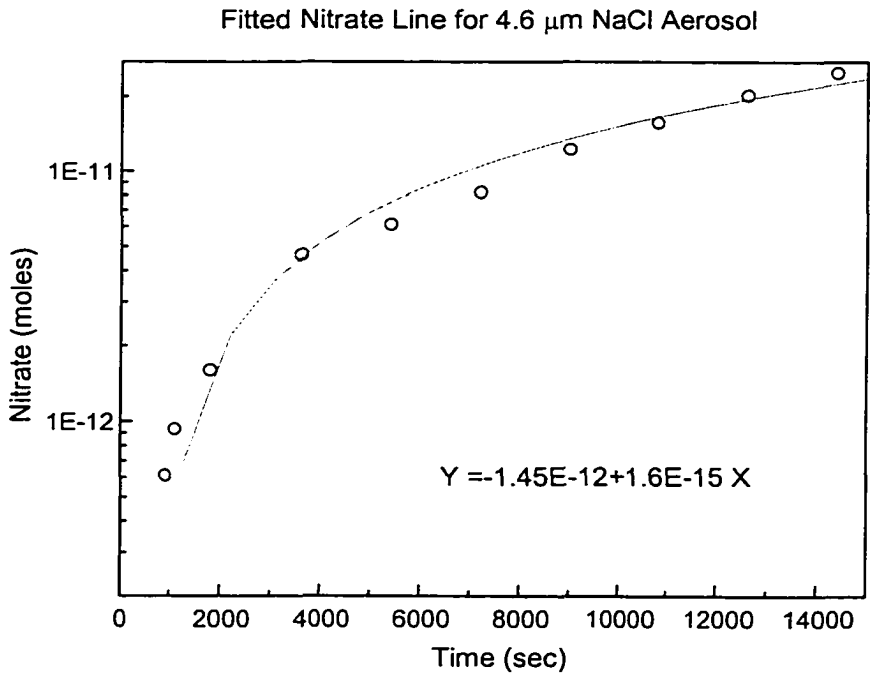

*Figure 2.11 Nitrate uptake by a 4.6μm hydrated NaCl aerosol. The curve is a straight line fit (minimized chi-square) to the first **four** hours of data for this experiment.*

The time-averaged γ values, as well as other relevant parameters for each aerosol are given in table 2.2 below. Only the first four hours of data were used for each aerosol. (The shortest data set was only four hours long). The time-average γ values were then plotted as a function of aerosol radius (hydrated). The result that small NaCl aerosols have large uptake coefficients, but large aerosols have small uptake values was unexpected and somewhat counter-intuitive. These results are discussed further in section 2.7 of this chapter.

Observations and Calculated Reactive Uptake Coefficients in Artificial Sea-salt Aerosols

Radius (dry) μm	Radius (hydrated) μm	Surface Area (cm^2)	Nitrate Uptake Rate (moles /sec)	Nitric Acid Flux (collision / cm^2 s)	γ average
3.8 ± 0.5	7.6 ± 0.5	(7.3±1) x 10^{-6}	(8.5±0.4) x 10^{-16}	(7.1 ± 1.5) x 10^{15}	(9.9±1.5) x 10^{-3}
4.6 ± 0.5	11.4 ± 0.6	(1.6±0.2) x 10^{-5}	(1.66±0.8) x 10^{-15}	(7.1 ± 1.5) x 10^{15}	(8.6±2.2) x 10^{-3}
5.2 ± 0.5	13 ± 0.9	(2.1±0.3) x 10^{-5}	(1.039±0.1) x 10^{-15}	(7.1 ± 1.5) x 10^{15}	(4.1±1.1) x 10^{-3}
6.7 ± 0.5	14 ± 0.7	(2.5±0.2) x 10^{-5}	(4.01±0.2) x 10^{-15}	(3.9 ±1) x 10^{16}	(2.5±0.7) x 10^{-3}

Table 2.2 Calculation results of time averaged reactive uptake coefficients for artificial sea-salt aerosols.

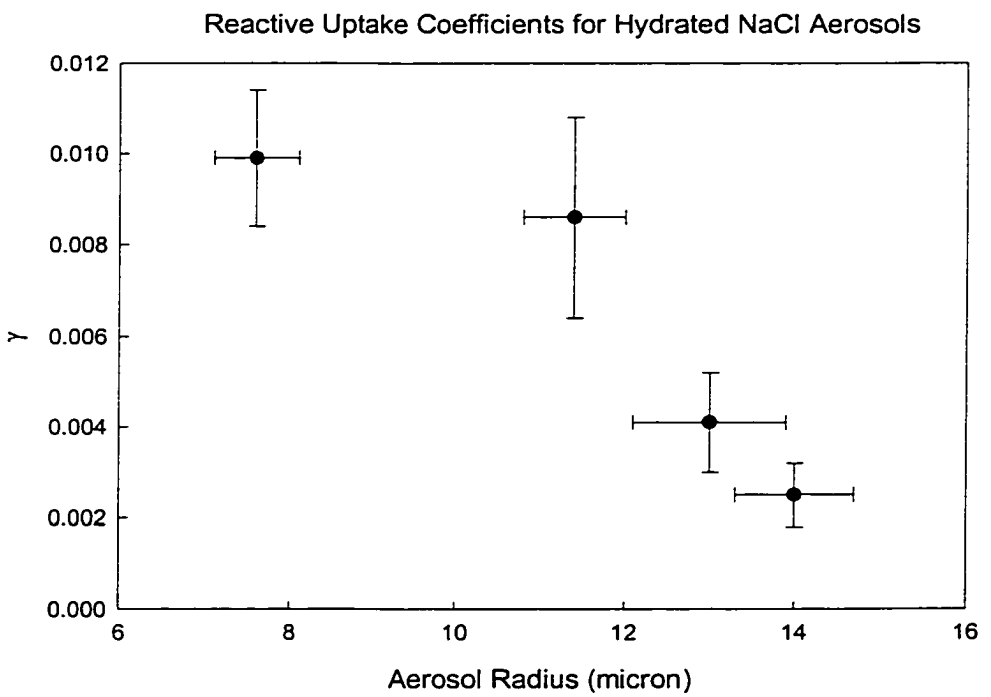

Figure 2.12: Radius dependence for γ in hydrated sea-salt aerosols subjected to dilute nitric acid vapor. This type of behavior would not be seen in bulk substrates.

The kinetic data presented here is interesting and certainly not the type of information available with experiments using bulk substrates or crystals for γ measurements. While noise in kinetic data is unsettling, most uncertainty in γ is caused not by chemistry measurements but by the radius measurement of the aerosol. To improve measurements of γ, clearly better accuracy and precision is needed in aerosol radius measurements. Several types of instruments are available to perform these measurements including linear diode arrays. This avenue was not pursued due to time and budget constraints. Instrumentation such as an FTIR spectrometer would be useful for making improvements in chemical measurements, and possibly would allow for the measurement of H+ ions, thereby allowing estimates of aerosol pH. It was hypothesized that the reactive uptake coefficients would be dependent on aerosol pH. The next series of experiments dealt with introducing ammonia and bicarbonate alkalinity into the NaCl aerosol and examining the nature of the uptake coefficients.

2.7 $NaHCO_3$ Alkalinity Experiments in Sea-Salt Aerosols

It is thought that the alkalinity in a sea-salt aerosol will buffer the aerosol against changes in pH due to uptake of acid gaseous species such as H_2SO_4 and HNO_3. To this end, a series of experiments involving $NaHCO_3$, HNO_3 and sea-salt aerosols was planned and conducted. As listed in table 2.1, bicarbonate is the largest source of alkalinity in sea-salt aerosols. The aerosol pH is buffered according to following reactions

$$CO_2(g) + H_2O \Leftrightarrow H_2CO_3 \Leftrightarrow H^+ + HCO_3^- \Leftrightarrow 2H^+ + CO_3^{2-} \qquad \text{Equation 2.12}$$

Any environmental change that would cause the pH of the droplet to decrease should release $CO_2(g)$ to the atmosphere.

The first task in this set of experiments was to determine if the Raman system could detect lines due to HCO_3^- and if the solution concentration could be calibrated in the bulk phase. The two best candidate HCO_3^- lines were located at 1050 cm^{-1} and 1365 cm^{-1}. The Raman

monochromator was set such that the high-resolution diffraction grating was used. A spectrum for a bulk solution of $NaHCO_3$ and de-ionized water is shown below in figure 2.13. A large concern was the potential to overlap the carbonate line at 1015 cm^{-1} with the nitrate line at 1050 cm^{-1}. (This was the reason for using the high-resolution diffraction grating). Very obvious in this spectrum are the lines due to bicarbonate as well as the 1640 cm^{-1} line due to water.

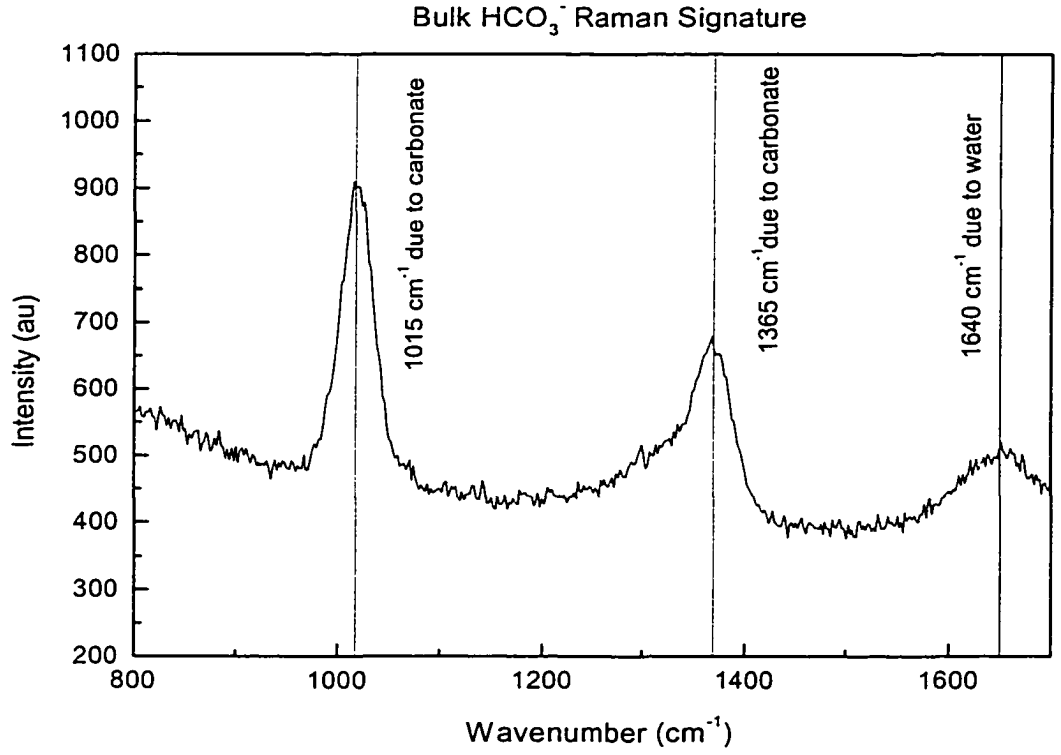

Figure 2.13 Bulk Raman spectra of water and $NaHCO_3$. The Raman monochromator was using the high-resolution diffraction grating for this spectrum.

A considerable amount of time was spent trying to determine if the NO_3 line at 1050 cm^{-1} could be "mathematically" separated from the 1015 cm^{-1} line of HCO_3^- in the spectrum. The two lines are close in wavenumber but separation of these two lines could be accomplished by using an elaborate curve-fitting program written in MATLAB. A sample spectrum and a result of the

curve-fitting program is shown in figures 2.14 and 2.15 below for a solution of $NaHCO_3$, HNO_3 and de-ionized water.

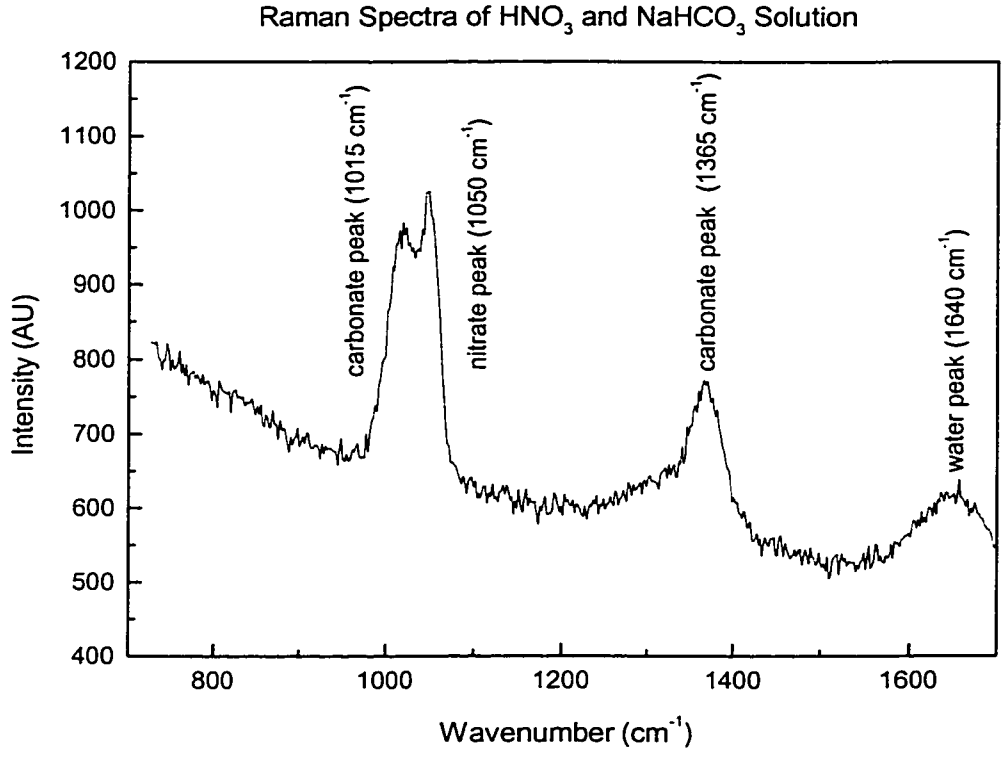

Figure 2.14 Raman spectra of a bulk solution of NaCl, H_2O and $NaHCO_3$. The spectrum was obtained with a high-resolution diffraction grating.

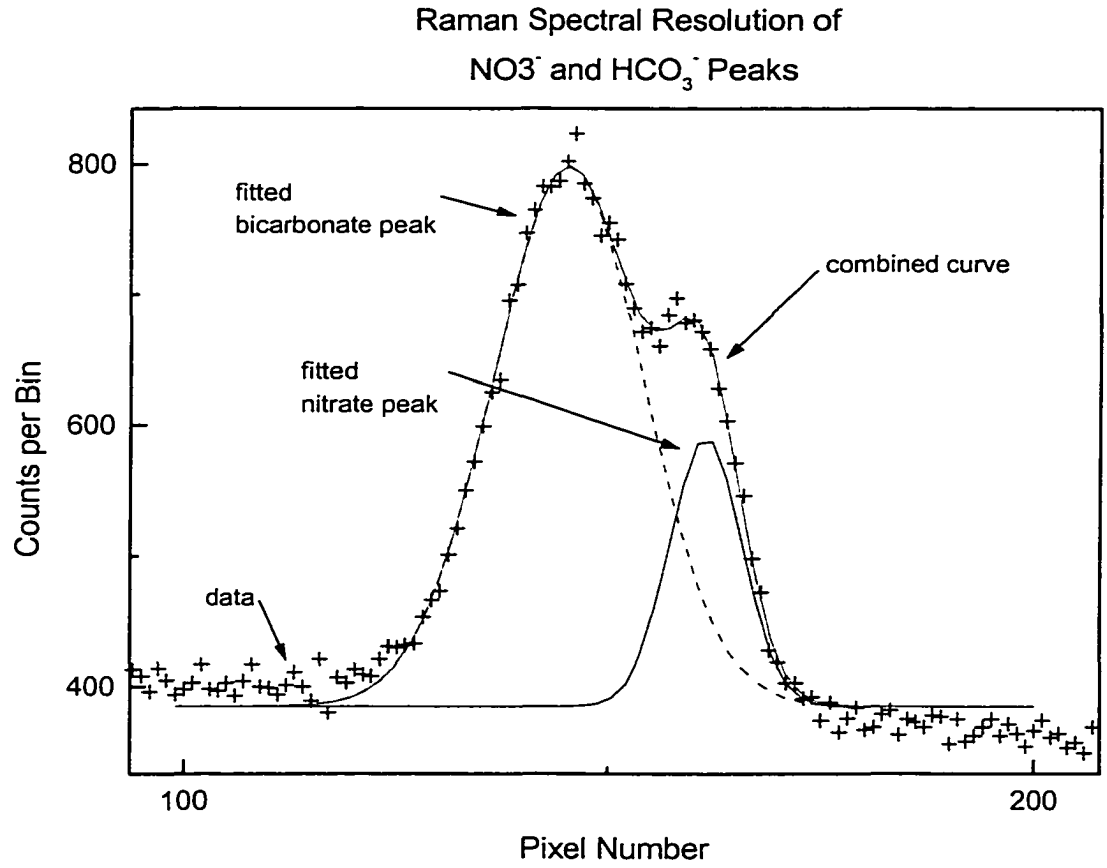

Figure 2.15: Raman spectra of NO_3 and HCO_3 lines at 1015 cm^{-1} and 1050 cm^{-1} using the high resolution diffraction grating in the Raman system.

The chemistry involving nitric acid, water and sodium bicarbonate is fairly straightforward. The following set of reactions (2.13, 2.14 and 2.15) was examined with the flytrap Raman system in a bulk phase. The reactions, as expected, proceeded rapidly and the effects were easily observed by the Raman system in the bulk phase.

$$HNO_3 \Leftrightarrow H^+ + NO_3^- \qquad \text{Equation 2.13}$$

$$HCO_3^- + H^+ \Leftrightarrow H_2O + (CO_2)_{aq} \qquad \text{Equation 2.14}$$

$$(CO_2)_{aq} \Leftrightarrow (CO_2)_g \qquad \text{Equation 2.15}$$

The results of the bulk titration experiments are summarized in figure 2.16 below. The data points were fitted to a hyperbola solely for the determination of an empirical relationship between the ratio of area underneath the HCO_3^- and NO_3^- peaks, and the amount of HNO_3 added to the $NaHCO_3$ solution.

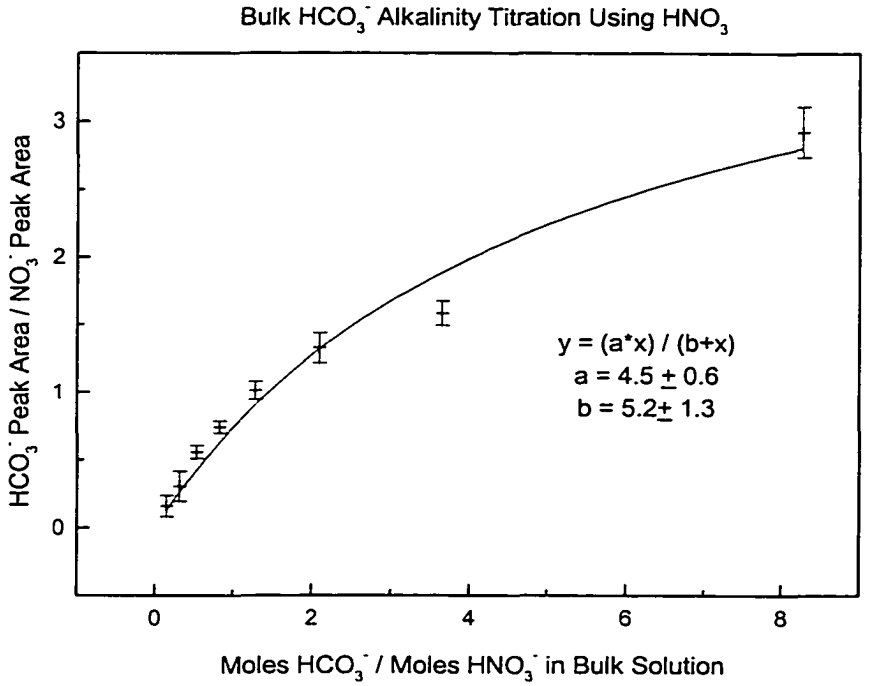

Figure 2.16: Titration of HCO_3 by nitric acid. The signal is nonlinear due to the removal of HCO_3 according to equations 2.13- 2.15.

Deconvolving nitrate and bicarbonate peaks, and the titration experiments worked well in the bulk experiments. The first aerosol experiment however was not so successful. In keeping with the previous aerosol / nitrate experiments, the diffraction grating was set on the low-resolution mode. Separation of the 1015 cm^{-1} and 1050 cm^{-1} lines was not possible with this grating. An attempt to measure the reactive uptake coefficient (of nitric acid) was made for several aerosols with carbonate alkalinity introduced. Previous work in the lab suggested that the carbonate peaks would disappear very quickly (within 15 minutes). It was thought that this

would show up in an increase of measured γ for the first 15 minutes of HNO_3 vapor exposure to the aerosol.

A solution of 5.19 grams NaCl, 0.98 grams $NaHCO_3$ and 110 grams of H_2O was mixed and pipetted into the micro particle injector. An aerosol of this composition was then injected into the quadrupole trap. The dried aerosol had a radius of (6.0 ± 0.5) μm. When hydrated the radius of the aerosol increased substantially and the resultant mass was near 5.0 nanograms, similar to other purely NaCl aerosols injected into the trap. After initial mass and radius measurements were made the aerosol was then subjected to a mixing ratio of 36 ± 5 ppb(v) nitric acid vapor. Raman and Mie scattering measurements were made to obtain information on the aerosol physics and chemistry in a manner similar to that described earlier. A plot of nitrate uptake as a function of time for this aerosol is shown below in figure 2.17.

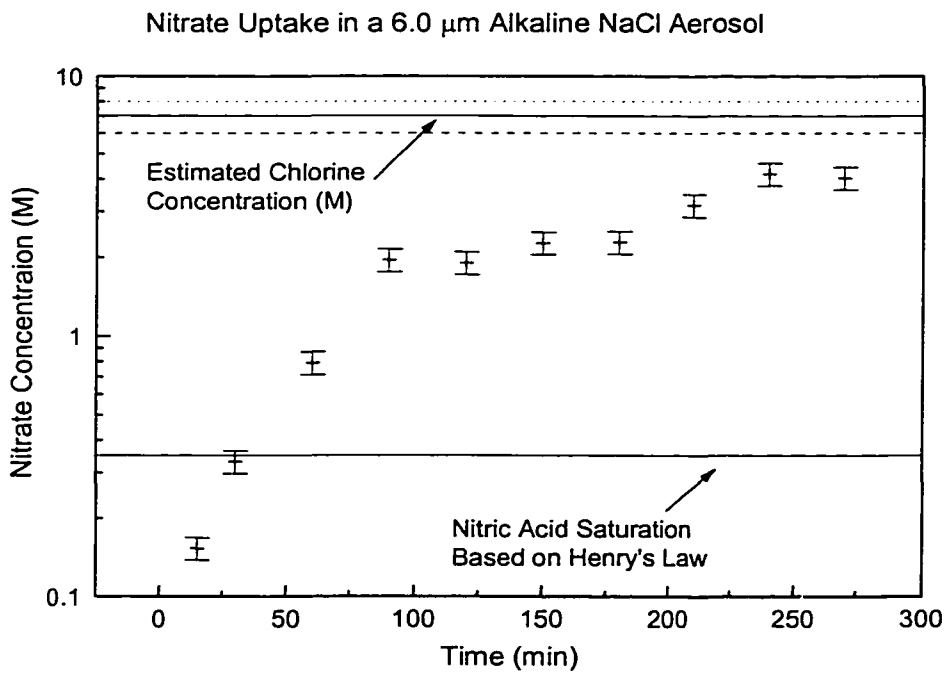

Figure 2.17: Uptake of nitrate in a 6.0 μm aerosol with a large (20%) carbonate alkalinity content. The Raman spectra were obtained with the low-resolution diffraction grating.

The results of this experiment provide no conclusive information about an increase of the average reactive uptake coefficient for aerosols doped with alkalinity. Early on in the experiment however, the aerosol radius decreased from 10 μm to 7.2 μm, coinciding with what was thought to be a release of CO_2 gas from the aerosol.

Based on this information it was decided to repeat the experiment using the high-resolution diffraction grating in the Raman system. The first order of business was to calibrate the Raman detector for nitrate and carbonate signals using the high-resolution diffraction grating. The procedure for this is very similar to that described earlier in the chapter. The results of the calibration are shown below in figure 2.18. As with the other diffraction grating, the response of the Raman system is highly linear with respect to the nitrate and carbonate signals as a function of compound concentration.

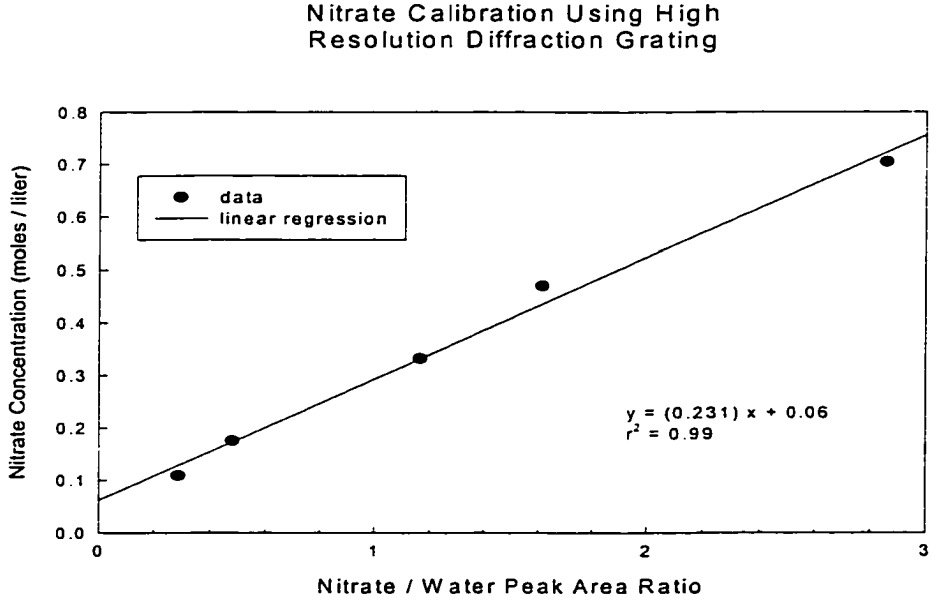

Figure 2.18 Calibration results of Raman system for the nitrate ion. The results of the linear fit are given in the plot above, along with the correlation coefficient.

A solution of 5.0 grams NaCl, 1 gram $NaHCO_3$ and 90 grams of H_20 was mixed and pipetted into the micro particle injector. An aerosol of this composition was then injected into the

quadrupole trap. The dried aerosol had a diameter of (5.2 ± 1.0) μm. When hydrated the radius of the aerosol and the mass increased substantially. After initial mass and radius measurements were made the aerosol was then subjected to a mixing ratio of 36 ± 5 ppb(v) nitric acid vapor. Raman and Mie scattering measurements were made to obtain information on the aerosol physics and chemistry in a manner similar to that described earlier. A plot of nitrate uptake as a function of time for this aerosol is shown below in figure 2.19.

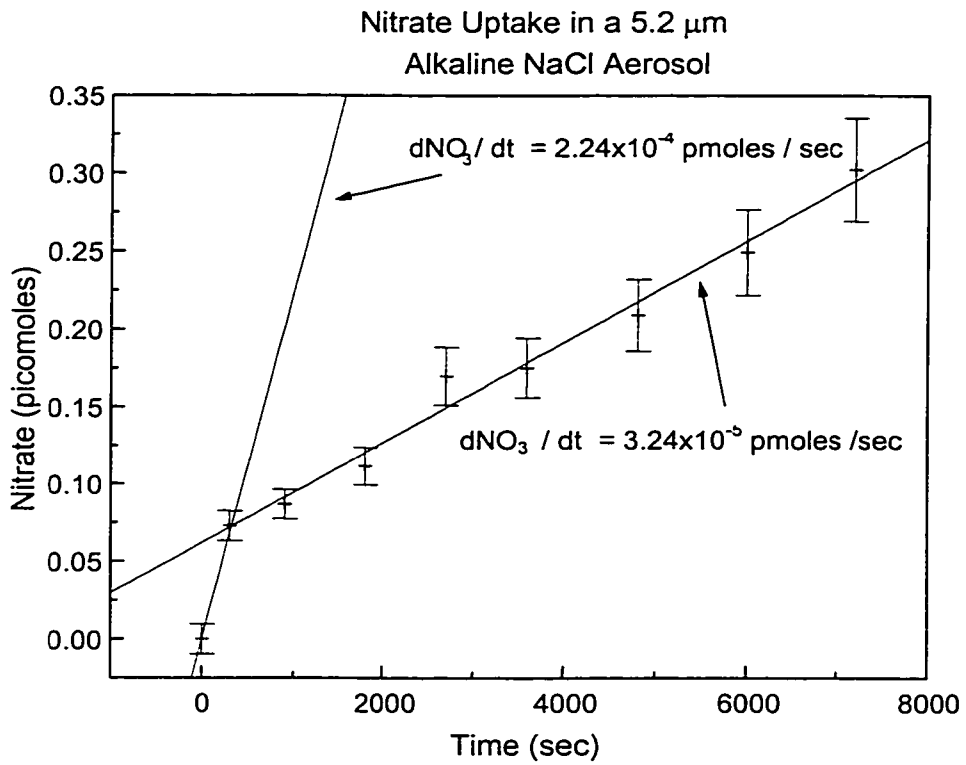

Figure 2.19: Result of alkalinity experiment. The slope of dNO_3^- as a function of time is fitted to two lines: one for the first 15 minutes of the HNO_3 vapor exposure and the second for the duration of the experiment.

The presence of bicarbonate was evident in the Raman spectra for this aerosol for the first several minutes of nitric acid vapor exposure. The HCO_3^- peak at 1015 cm^{-1} was evident only for the first 30 minutes of the experiment. After that, the counts for the HCO_3^- peak in the CCD detector went to zero quite rapidly. The radius of the aerosol also decreased from 13.2 μm to

12.0μm during this time period, synonymous with a mass loss (thought to be CO_2(g) release). When the slopes for (dNO_3^- / dt) were found, the subsequent values for γ could be calculated. For the first 15 minutes, γ was calculated to be $(7.0 \pm 0.9) \times 10^{-4}$. For the subsequent data points the γ value was calculated to be $(1.0 \pm 0.9) \times 10^{-4}$, nearly an order of magnitude smaller than when the carbonate alkalinity was present in the NaCl aerosol. Similar types of alkalinity experiments were conducted with gas phase NH_3 introduced to the trap chamber. Due to a lack of a strong enough Raman signal from ammonia and ammonium, even in the bulk phase, these experiments did not provide any additional information on the kinetics of nitrate uptake by the NaCl aerosol.

2.8 Summary and Discussion

The flytrap instrument proved to be a useful device to explore the nature of coarse mode nitrate formation in sea-salt aerosols. Uptake rates of nitric acid for aerosols of various sizes, nitric acid vapor mixing ratios and (assumed) pH values as a function of time were examined. The effect of bicarbonate alkalinity on the reactive uptake rates of nitric acid in sea-salt aerosols was also observed. Two separate relative humidity values (0% and 90%) were used in the measurements of uptake rates. It was also demonstrated that $NaNO_3$ in a sea-salt aerosol is a permanent removal pathway for nitrate in the atmosphere.

Comparison of measurements of γ made with the flytrap instrument to results obtained by Laux et al. [1994] for the 0% RH measurements were made and found to agree within experimental uncertainty. Using the flytrap instrument, the reactive uptake coefficient γ, of nitric acid on dry NaCl at 298K was measured to be **(2.5±0.8) x 10^{-4}**. Laux et al. using an X-ray photoelectron spectroscopy technique, under similar pressure and temperature conditions, measured the reaction probability to be $(4+2) \times 10^{-4}$. Clearly, using the flytrap to measure the reactive uptake coefficient for nitric acid vapor on a dry NaCl crystal yields a more accurate result. The two results however agree to within experimental uncertainty.

Under conditions found in the marine boundary layer, the measured reactive uptake coefficient for a dry NaCl aerosol is a lower limit. It is expected that changing the mixing ratio of nitric acid won't change the γ result. A higher HNO_3 mixing ratio will lead to additional molecular collisions with the surface of the aerosol, resulting in a higher proportion of $NaNO_3$ formation leaving the γ value unchanged. Increasing the water content of the NaCl aerosol then is one way to increase the value of γ. The upper limit on the reactive uptake coefficient γ, then is the accommodation coefficient α, of HNO_3 on a pure water droplet.

The difference between accommodation coefficient and reactive uptake coefficient is found be examining the following equation (Seinfeld and Pandis, 1998):

$$\frac{1}{\gamma} = \frac{R_p c_a}{4D_g} + \frac{1}{\alpha} + \frac{c_a}{4RTH_A\sqrt{kD_{aq}}} \qquad \text{Equation 2.16}$$

where

γ = reactive uptake coefficient

α = mass accommodation coefficient

R_p = radius of the particle

D_g = the diffusivity of gas in air

R = gas constant

T = temperature

H_a = **effective** Henrys law constant (described by equation 2.8)

k = Boltzmans' constant

D_{aq} = aqueous phase diffusion constant

c_a = mean speed of molecules

The terms on the right hand side of equation 2.16 show the three contributions to overall resistance to uptake: (1) gas phase diffusion, (2) mass accommodation at the surface, (3) and interfacial transport/aqueous phase diffusion. The reactive uptake coefficient γ is equal to the

mass accommodation coefficient only if the other resistances are negligible. In experimental evaluations, γ is measured, all other quantities in 2.16 are known and α is calculated. Van Doren et. al (1990) performed studies leading to an α value for nitric acid vapor on pure water droplets. At a temperature of 295 K these values were estimated to be between 0.05 – 0.07. The accommodation coefficient of HNO_3 on a water droplet then is an upper limit to the reactive uptake coefficient on wetted particle surfaces.

When aqueous NaCl aerosols are injected into the trap, they quickly equilibrate to ambient relative humidity. The RH in the trap chamber can easily be brought above the NaCl deliquescent point (usually near 65%), at which point the NaCl rapidly dissociates forming a solution of high ionic strength. The ionic strength of the aerosol can be estimated with

$$I = \frac{1}{2}\sum_{i=1}^{n} m_i z_i^2 \qquad \text{Equation 2.17}$$

where n = number of species, m_i = molality (solute concentration in mol /kg of solvent) and the number of ion charges of ion I respectively. Estimates of NaCl aerosols suspended in the trap at 90% RH yield ionic strengths of approximately (4.3±0.5 m). For comparison, estimates of the ionic strength of seawater have been measured to be near 0.8 m (Libes, 1992).

When nitric acid vapor is introduced to the trap chamber, chemical reactions in the aerosol start to occur. Based on laboratory experiments (this set) a simplified illustration of the processes occurring in the NaCl aerosol is shown below in figure 2.20.

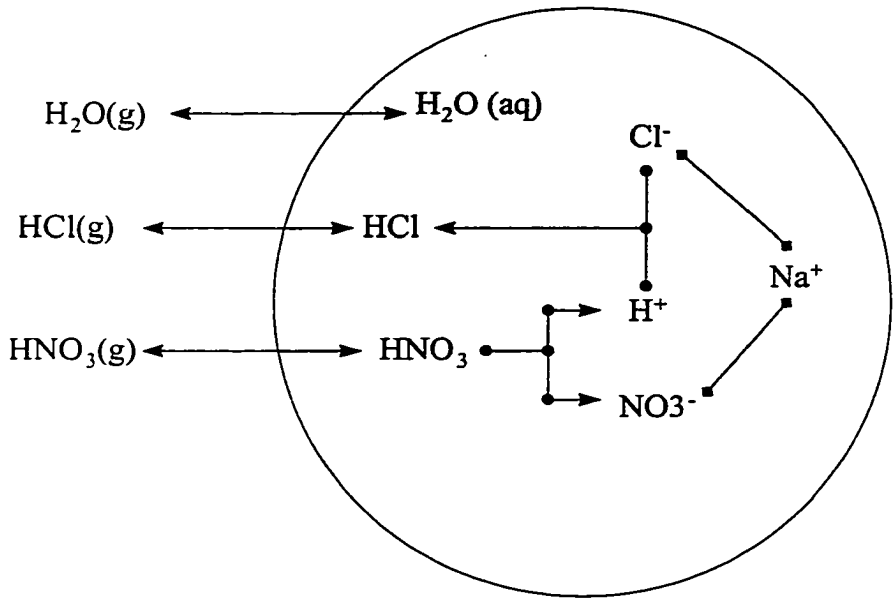

Figure 2.20: Simplified pictorial representation of physical and chemical behavior of processes occurring in a sea-salt aerosol subjected to nitric acid vapor.

When nitric acid vapor is introduced to the trap chamber, some of the gas quickly diffuses to the surface of the aerosol where the adsorption of HNO_3 is governed in accordance with Henry's law. The effective Henry's law constant for this reaction is highly pH dependent. The dissolved nitric acid quickly dissociates into NO_3^- and H^+ ions at which point the ions are free to diffuse through the droplet. The diffusion can be described by using equation 2.5. The H^+ ions are free to interact with the Cl^- ions initially present in the sea-salt aerosol. When the free hydrogen and chlorine ions combine to form HCl, the pH of the aerosol is expected to rise somewhat, allowing for a larger amount of HNO_3 to be dissolved in solution. The effective Henry's Law constant (in moles per atmosphere) is pH dependent and be described with the following equation

$$H^{\bullet}_{HNO3} \approx H_{HNO3} \frac{K_{n1}}{[H^+]} \approx \frac{3.2 \times 10^6}{[H^+]} \qquad \text{Equation 2.8}$$

where H_{HNO3} is the Henry's Law coefficient, [H+] is the hydrogen ion concentration and K_{n1} describes the dissociation concentration for nitric acid.

As with HNO_3, HCl is subject to Henry's law. At a temperature of 298K, HNO_3 and HCl have Henry's law constants of 2.1×10^5 M atm^{-1} and 727 M atm^{-1} respectively. Desorption of the less soluble HCl from the liquid phase then buffers the aerosol against large changes in pH while chlorine is present in the aerosol. Experimental evidence from this study indicates that nitric acid vapor will be taken up until the sea-salt aerosol is completely depleted of chlorine. It is clear that the H^+ ion plays a central and pivotal role in regulating the uptake of nitric acid in the sea-salt aerosols.

The reactive uptake coefficients measured in this set of experiments exhibited some rather unusual and unexpected time and radius dependence. The time dependant behavior of γ can be seen in figure 2.9. At this time no explanation for the initial low experimental assessments of γ can be offered other than it may take up to an hour for the H^+ - Cl^- reaction to reach a maximum based solely on the concentration of H^+ in the aqueous aerosol. Clearly further experimentation is needed to elucidate this behavior. The subsequent decrease of γ can be explained by decreased concentrations of Cl^- in the aerosols. The time rate of change (formation) of HCl is proportional to $[Cl^-]$. With a decrease in HCl formation, more H^+ ions are available to decrease the aerosol pH, leading to a lower effective Henry's rate constant and therefore a lower value for γ. The conclusion that can be drawn from this set of experiments is the value for γ is highly dependent on aerosol pH.

Due to their large surface area to volume ratio, it is expected that scavenging of gas-phase acids decreases the pH of large particles more slowly than that of small particles (Keene et al., 1998). In the case for nitric acid uptake on sea-salt aerosols, it is easily observable in figure 2.12 that larger NaCl aerosol have small reactive uptake coefficients. Surprisingly, there is scant information on the direct measurement of pH of size-segregated aerosols in the natural atmosphere (Keene et al., 1998). The size dependence of chloride depletion has been studied by various researchers (Xiaohong, 2001). Most results show that the percentage of chloride

depletion decreases with increasing particle size. The thermodynamics and kinetics of HCl phase partitioning, the dynamics of the surface reaction such as HNO_3 on the sea salt particles, and in-cloud processes have been used to explain the size dependence of chloride depletion in sea salt aerosols (Xiaohong, 2001).

Introduction of alkalinity to the aerosol initially has a profound impact on the reactive uptake of acidic gases. This was experimentally verified as part of the nitric acid study performed here. Figure 2.21 below illustrates the complexity of the chemical reactions occurring in a sea-salt aerosol when carbonate alkalinity is introduced. With the carbonate alkalinity, the dissolved nitric acid quickly adsorbed and dissociated (pH dependant). The hydrogen ions thermodynamically prefer to react with the bicarbonate ions, ultimately forming CO_2, which based on the Henry's Law coefficient escapes the sea-salt aerosol much more quickly than HCl produced in the aerosol. Both the Henry's Law coefficients for CO_2 and HCl are temperature dependent. It is expected that any change in the ambient temperature will ultimately affect the uptake of nitric acid by an NaCl aerosol. These studies could be easily conducted in the future using the flytrap instrument with only minor modifications.

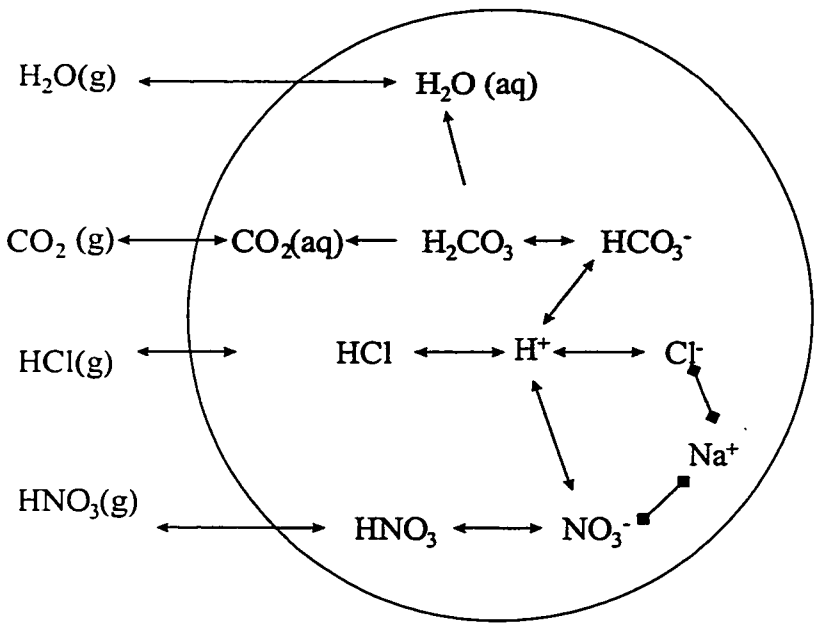

Figure 2.21: Pictorial representation of physical and chemical behavior of processes occurring in a sea-salt aerosol containing bicarbonate alkalinity subjected to nitric acid vapor. The H^+ ion plays a pivotal and central role in regulating the uptake of nitric acid.

One set of experiments suggested but not pursued in this study is the effect of systematically changing the mixing ratio of HNO_3 introduced to the trap chamber. It is expected that changing the mixing ratio of nitric acid will lead to an increased number of collisions of these molecules with the aerosol surface. This will ultimately lead to a proportionately higher rate of HCl or CO_2 molecules leaving the aerosol volume per unit time. As such, the reactive uptake coefficient should remain unchanged. It would be an easy exercise to test this hypothesis with the current Flytrap instrument setup, but is left for a future experiment.

One must use caution when applying the results from these experiments to conditions found in the atmosphere. Several important differences exist between conditions found in the lab setting and the marine boundary layer, one of which is the existence of organic coatings on the

aerosols. It is hypothesized that these coatings would interfere drastically with the estimates for γ by reducing the number of molecules diffusing into the volume of the aerosol.

The relative humidity found in the atmosphere is not usually 90%. The values for γ varied between 2.5×10^{-4} and 0.01 when the relative humidity was varied between 0% and 90%. With humidities lower than 90%, the ionic strength of the aerosol increased greatly, leading to changes in the chemical behavior of the aerosol constituents, namely a higher rate of HCl formation between free H^+ and Cl^- ions.

In addition to these differences, the behavior of nitric acid interactions with sea-salt aerosols in the open atmosphere cannot be treated as an open system. The mixing ratio of HNO_3 will decrease as more of the vapor is taken up by the aerosol distribution. The dynamic behavior of nitric acid was beyond the scope of these experiments. In addition to nitric acid, other gases present in the natural atmosphere will also profoundly affect the nature and rate of uptake of HNO_3 by NaCl aerosols. The next chapter in this work deals with the interactions between SO_2, $SO_4^=$, NH_3, O_3 and H_2O_2 and NaCl aerosols and NaCl aerosols spiked with bicarbonate alkalinity.

Several atmospheric implications can be drawn from these laboratory measurements however. First, it was shown that the physiochemical properties of NaCl aerosols change with reaction with water and nitric acid vapor. The morphology changes, the surface area changes and increased water adsorption change. These all have important implications for the processing of aerosols in the atmosphere that contain NaCl. This includes changes in optical properties of the aerosols due to shape and composition changes. The second important issue that can be addressed by this study is whether HNO_3 removal by NaCl aerosols could be significant enough to reduce the HNO_3 / NO_x ratios when included in the global chemistry models. This laboratory study showed that the reaction of HNO_3 with NaCl is not limited to the surface of the aerosol but can react with the bulk of the aerosol in the presence of H_2O vapor. Because the relative humidity of the marine boundary layer is often near 90%, it is possible that this reaction, as well

as that with calcium carbonate mineral aerosols will provide a large sink for HNO_3, as indicated by the modeling studies of Tabazadeh et al. [1998]. Recent box-model calculations show that reactive uptake coefficients as small as $1x10^{-5}$ are sufficient to significantly reduce HNO_3 mixing ratios in the atmosphere (Underwood et al., 2000).

CHAPTER 3

SULFATE PRODUCTION IN SEA-SALT AEROSOLS

3.1 Introduction

The concern that air pollution may grow to the global scale is real. There is good evidence that many tropospheric gases, active either chemically or radiatively, have grown in abundance since the pre-industrial era. Among the chemically reactive species, long-term increases in CH_4 and tropospheric O_3 are well known (IPCC, 1990). For NOx, current anthropogenic emissions are thought to be comparable to or larger than global natural sources (IPCC, 1990; WMO, 1991). The first major global concern is that an increase in these gases, some of which are strong infrared absorbers, may change the radiative balance of the atmosphere, possibly resulting in climate change. The combined radiative effect of all of these gases is about double that of carbon dioxide alone. Additional climate perturbations may come from aerosols, formed when some compounds such as sulfur dioxide and dimethyl sulfide (CH3-S-CH_3, or DMS) react in the troposphere to form H_2SO_4, which can lead to the formation of sulfate aerosols. These aerosols can absorb and scatter light, and, if appropriate in size, can also function as cloud condensation nuclei (CCN), changing the size distribution of cloud droplets and affecting cloud reflectivity (Charlson et al., 1987).

Our understanding of elementary reaction kinetics and reaction mechanisms involving atmospheric sulfur compounds is crucial to improving current models of the global sulfur cycle as well as parameterization of important atmospheric processes such as cloud formation and albedo effects in global climate models. The goal of this series of lab experiments was to understand the

formation of non sea-salt sulfate in deliquescent aerosols under conditions found in a marine boundary region.

The oxidation of naturally occurring and anthropogenic sulfur emissions may result in H_2SO_4, which is a major cause of acid rain. Sulfuric acid particles can also act as cloud condensation nuclei and thus can alter the albedo of the planet. It has been suggested that this mechanism could be an important negative feedback to global warming (Charlson et al., 1987). While chemical reactions involving sulfur species that occur in clouds and in rainwater have been studied in detail, very little is known of the aqueous-phase chemical reactions that occur in deliquescent aerosols (Chameides and Stelson, 1992).

Below-cloud models of Chameides and Stelson (1992) predict a significant removal mechanism for $SO_2(g)$ from the scavenging of S(IV) gases by deliquescent sea-salt particles with subsequent oxidation to sulfate by $O_3(g)$. The extent of reaction is predicted to be dependent upon the sea-salt particle alkalinity. Since coarse sea-salt particles are removed fairly quickly from the lower atmosphere, this could represent a fast removal mechanism for $SO_2(g)$ and newly formed particulate sulfate and potentially a large mass flux of sulfate (McInnes et al., 1994). The basic mechanism of the reaction occurs as follows

$$SO_2(g) \leftrightarrow SO_2(aq) \qquad \text{Equation 3.1}$$

$$SO_2(aq) + H_2O \leftrightarrow HSO_3^- + H^+ \qquad \text{Equation 3.2}$$

$$HSO_3^- \leftrightarrow SO_3^{2-} + H^+ \qquad \text{Equation 3.3}$$

The conversion of sulfurous acid to sulfuric acid involves further oxidation from state (IV) to state (VI) that requires an oxidizing agent such as O_3 or H_2O_2.

Like its nitric acid counterpart, the reaction between sea-salt and acidic sulfate is expected to liberate HCl gas to the atmosphere leaving the particles enriched in nss sulfate and depleted in chloride (Eriksson, 1959).

$$H_2SO_4(g) + 2NaCl(s) \rightarrow 2HCl(g) + Na_2SO_4(s) \qquad \text{Equation 3.4}$$

Freshly produced sea-salt aerosols are alkaline in contrast to most liquid water environments in the remote atmosphere (which tend to be acidic). Because of the sizable buffering capacity of these aerosols (see Chapter 2, this work), they are capable of absorbing significant amounts of acid before experiencing a drop in pH (Chameides and Stelson, 1992).

In large part because of the buffering capacity of sea-salt, sea-salt aerosols appear to represent an ideal medium for the oxidation of atmospheric SO_2 by O_3 and thus for facilitating the removal of S from the atmosphere. The calculations of Chameides and Stelson (1992) indicate that the rate of removal of SO_2 by sea-salt is quite significant and is roughly equal to the rate of DMS emission from the ocean. It is thus possible that much of the SO_2 produced from DMS oxidation is removed by sea-salt and returned to the ocean before it has had a chance to be converted to CCN sulfate particles. Chameides and Stelson claim that due to the highly simplified nature of their model, the uncertainties in the kinetic and thermodynamic data used in the model, and limited set of atmospheric observations used to evaluate the model, their results should be viewed as preliminary and their conclusions viewed as speculative. It was with these statements in mind that the following set of experiments was undertaken.

3.2 Background on Sulfur Dioxide, Ozone and Hydrogen Peroxide

Because the following series of experiments involve the interaction of sulfur dioxide, ozone and hydrogen peroxide, a brief background on these gases is provided. Sulfur dioxide is the predominant anthropogenic sulfur-containing air pollutant (Seinfeld and Pandis, 1998). Mixing ratios of SO_2 in the continental background atmosphere range from 20 ppt(v) to over 1 ppb(v) ; urban SO_2 mixing ratios can attain values of several hundred parts per billion. Large amounts of SO_2 enter the atmosphere each year from anthropogenic sources, mainly the combustion of fossil fuels and the smelting of metals (Warneck, 1988). Known sources of natural SO_2 to the atmosphere have been well known for years and include volcanic emissions and emanation of reduced sulfur compounds from the biosphere such as DMS (Warneck, 1988).

DMS is rapidly oxidized in the atmosphere and the associated sulfur is thought to be quickly returned to the Earth's surface. A thorough description of the global sulfur chemistry cycle and its atmosphere component is extremely complicated and is outside the scope of this work. The interested reader is referred to the excellent treatise by Seinfeld and Pandis (1998) on this topic.

Hydrogen peroxide is the dominant oxidant in clouds, fogs or rain in the atmosphere (Seinfeld and Pandis, 1998). Photochemical activity largely dominates the diurnal, seasonal, and latitudinal variations of H_2O_2 mixing ratios (Sakugawa, 1990). The principal mechanisms for the production of H_2O_2 in either the gas or aqueous phase proceed via reactions of HO_2 to produce H_2O_2.

$$HO_2 + HO_2 \rightarrow H_2O_2 + O_2 \qquad \text{Equation 3.5}$$

Photochemical models indicate the gas phase formation of H_2O_2 will result in mixing ratios less than 1 part per billion (Gunz and Hoffman, 1990). Depending on altitude, ambient ultra-violet radiation, ozone mixing ratio, water vapor and NO_x, the expected gas phase mixing ratios vary between 0.1 and 5 ppb(v). Measurements of H_2O_2 levels (e.g. Sagkugawa et al., 1990) confirm these predictions. H_2O_2 can be produced in situ in cloud-water droplets or on surface waters. The photochemistry and free radical mechanisms for H_2O_2 production in cloud-water droplets have been well described in the literature (Gunz and Hoffman, 1990).

The effective Henry's Law coefficient for hydrogen peroxide of 7.45×10^4 M atm^{-1} makes it extremely soluble in water. Its aqueous-phase precursor, HO_2 also has a large Henry's Law constant of 2.0×10^3 M atm^{-1}, indicating the formation of hydrogen peroxide in the aqueous phase is dependent on the accommodation of the gaseous HO_2 radical in the atmosphere. Once dissolved in water hydrogen peroxide dissociates to produce HO_2^- via

$$H_2O_2 \Leftrightarrow HO_2^- + H \qquad \text{Equation 3.6}$$

but is a rather weak electrolyte with a dissociation constant of $K_{h1} = 2.2x10^{-12}$ M at 298 K. Therefore, for most atmospheric applications, the dissociation of dissolved hydrogen peroxide can be neglected.

Unlike stratospheric ozone, ground level (or tropospheric) ozone is created through the interactions of man-made and natural emissions of volatile organic compounds and nitrogen oxides in the presence of heat and sunlight (Liu and Trainer, 1988). Ground-level ozone is formed when volatile organic compounds (VOCs) and nitrogen oxides (NO_x) interact in the presence of sunlight. Sources NOx emissions include industries such as fossil fuel burning power plants as well as internal combustion engines. Tropospheric nitrogen oxides originate primarily from the heating of air to temperatures where the Zeldovich mechanism becomes operative,

$$O_2 + heat \Rightarrow O + O \qquad \text{Equation 3.7}$$

$$O + N_2 \Rightarrow NO + N \qquad \text{Equation 3.8}$$

$$N + O_2 \Rightarrow NO + O \qquad \text{Equation 3.9}$$

These temperatures are reached during most combustion processes (including fossil fuel and biomass burning) and lightning. Additional NO_x sources may be associated with bacterial processes in soils. Once in the atmosphere, NO and NO_2 partake in many chemical reactions. Some of these are simple NO - NO_2 inter-conversions, while others are actual NOx sinks. In particular, the reaction

$$OH + NO_2 + M \Rightarrow HNO_3 + M \qquad \text{Equation 3.10}$$

removes NO_x quickly, with about 1 day lifetime for typical mid-latitude conditions (Seinfeld and Pandis, 1998). The short NO_x lifetime has one important implication: If the sources of NO_x are not geographically uniform (which is certainly the case), the global NO_x distributions will be highly variable, being very sensitive to both chemical and meteorological (transport) processes.

Cars and gasoline-burning engines are also large sources of volatile organic compounds (VOCs). VOCs also come from consumer products such as paints, insecticides, and cleaners as

well as industrial solvents and chemical manufacturing. The sun's direct ultraviolet rays play a role in converting the NO_x and VOC emissions into ground-level ozone, which poses a health hazard when inhaled at high mixing ratios.

Many factors impact ground-level ozone development, including temperature, wind speed and direction, time of day, and driving patterns. Due to its dependence on weather conditions, ozone is typically a summertime pollutant and a chief component of summertime smog. Ozone is made in the troposphere by the same reaction responsible for its formation in the stratosphere: the addition of ground state oxygen atoms $O(^3P)$ to molecular oxygen O_2, assisted by any third body M to ensure simultaneous momentum and energy conservation.

$$O(^3P) + O_2 + M \Rightarrow O_3 + M \qquad \text{Equation 3.11}$$

However, the source of the O atoms is different than in the stratosphere where the O atoms are made by the photodissociation of O_2 at UV wavelengths < 240 nm. In the troposphere, only UV radiation with wavelengths > 290 nm is available, due to essentially complete absorption of shorter wavelengths by O_2 and O_3 above the tropopause. An alternate source of O atoms is necessary to explain tropospheric ozone formation. Exhaustive searches of plausible tropospheric reactions reveals only a few possibilities that yield O atoms, and among these only one appears to be important: the photodissociation of NO_2,

$$NO_2 + h\nu(\lambda < 410nm) \rightarrow NO + O(^3P) \qquad \text{Equation 3.12}$$

While the $O(^3P)$ produced by NO_2 photolysis does form ozone, the NO produced in the same reaction reacts rapidly with ozone,

$$NO + O_3 \rightarrow NO_2 + O_2 \qquad \text{Equation 3.13}$$

Thus, the net ozone production is strongly limited. In a simplistic form, the steady state ozone mixing ratio can be expressed as a function of the $[NO_2]$ / [NO] ratio (Seinfeld and Pandis, 1998).

Ozone is slightly soluble in water with a Henry's Law constant of only 0.011 M atm^{-1} at 298K. For a cloud gas-phase mixing ratio of 100 ppb(v), the equilibrium ozone aqueous phase

concentration is $1.1x10^{-9}$ M. It is not surprising then to see that most of the ozone remains in the gas phase (Seinfeld and Pandis, 1998).

3.3 Some Experimental Details

With the above discussion in mind, investigations into the oxidation of sulfur dioxide to sulfate inside aqueous sea-salt aerosols were conducted.

3.3.1 Instrument Calibration

Prior to using the Raman system to identify various chemical compounds, the system was wavelength calibrated. This involved mapping each pixel in the CCD camera to a specific wavelength. A typical calibration spectrum is shown below in figure 3.1. This technique was used to calibrate both the 300 and 1200 g / mm diffraction gratings.

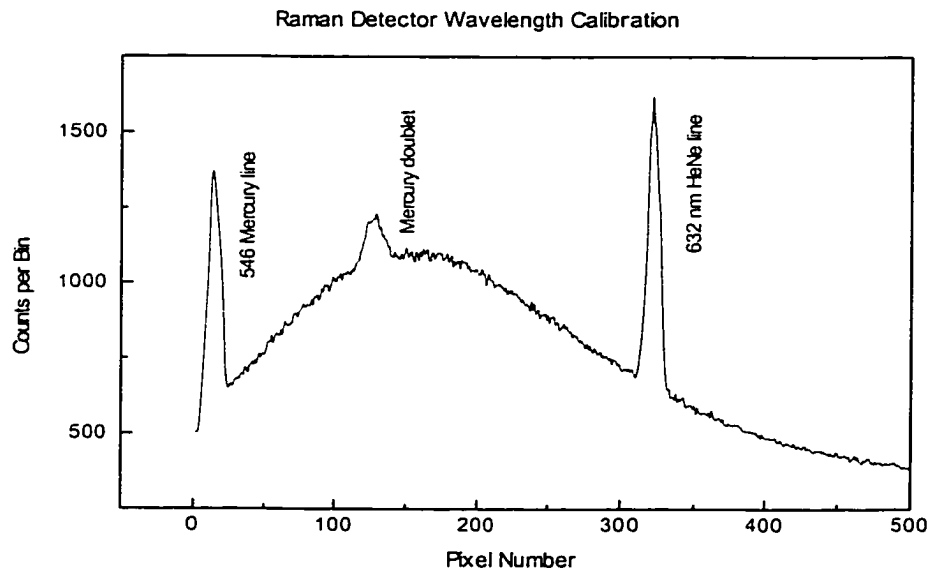

Figure 3.1 Experimental Raman system wavelength calibration. The calibration of the 300 g/mm grating was carried out using a HeNe laser to produce the 632-nm line and a mercury lamp to produce the doublet and 546-nm line. The calibration of the 1200 g/mm grating was carried out in a similar manner, using the identical mercury lines.

To determine the concentration of $SO_4^{=}$ ions in hydrated sea-salt aerosols, a bulk solution calibration curve was created. This procedure is very similar to those described in chapters 1 and

2 of this work. Mixed solutions of varying concentration of Na_2SO_4 were placed in a cuvette and the Raman system response was measured. For each mixture, the counts underneath the water and sulfate peaks were measured using straightforward numerical integration. The procedure for finding sulfate concentration in droplets was treated exactly in the same manner as for the calibration solutions. The sulfate features used were the 980 cm^{-1} line and the 1104 cm^{-1} line. Water peaks located between 3000 and 4000 cm^{-1} as well as the line at 1640 cm^{-1} were also used for the calibration efforts. A typical spectrum from this calibration effort is shown below in figure 3.2.

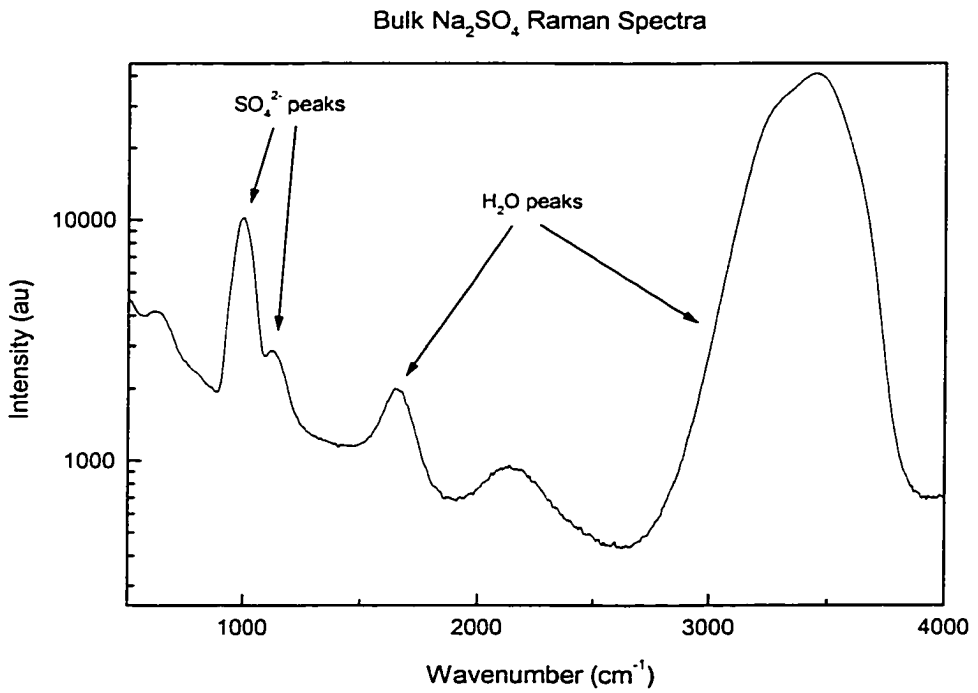

Figure 3.2 Raman spectrum of a bulk 2M Na_2SO_4 solution at 25 °C. The spectrum was taken using the 300 g/mm grating (low resolution) in the monochromator. The sulfate peaks are located at 980 cm^{-1} and 1104 cm^{-1} with water peaks located at 1640 and 3000-4000 cm^{-1}.

The line shown below in figure 3.3 was the result of the calibration effort for the low-resolution diffraction grating. The first task in the calibration was to determine the area (counts)

underneath the sulfate and water peaks respectively. A linear regression to the calibration data showed that the relationship between peak counts ratio to concentration (molarity) was

$$y = (33.2 \pm 0.4)\, x + (0.07 \pm 0.01) \qquad \text{Equation 3.14}$$

with a correlation coefficient of 0.99, where y represents the solution molarity and x represents the sulfate peak area to water peak area ratio.

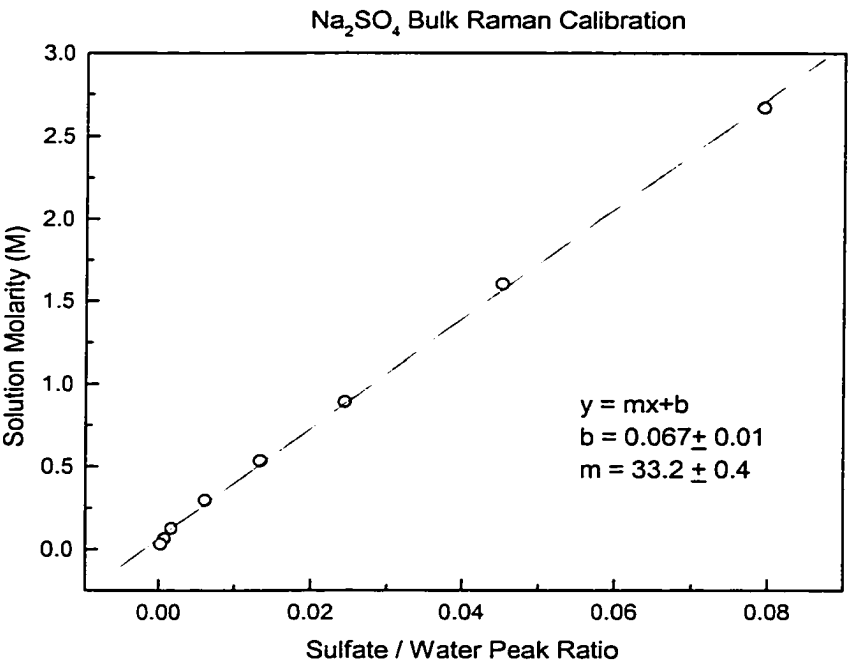

Figure 3.3 Bulk sulfate calibration using Na_2SO_4 in a bulk solution at 25 °C for the low resolution diffraction grating

Due to consistent problems with Raman florescence when examining hydrated aerosols using the low-resolution diffraction grating, the majority of experiments conducted as part of this study were done so using the high-resolution diffraction grating. As a result, similar bulk calibrations had to be conducted using the high-resolution diffraction grating.

In contrast to the 300-g/mm (low-resolution) grating, a spectrum of the same Na_2SO_4 solution taken with the 1200 g/mm (high-resolution) grating is shown in figure 3.4. The

predominant sulfate peak shows up at 980 cm^{-1} and is due to the symmetric SO_4^{2-} ion stretch. The resolution of the observed Raman frequencies is increased by using the 1200 g/mm grating, but the spectrum only spans approximately 1000 cm^{-1}.

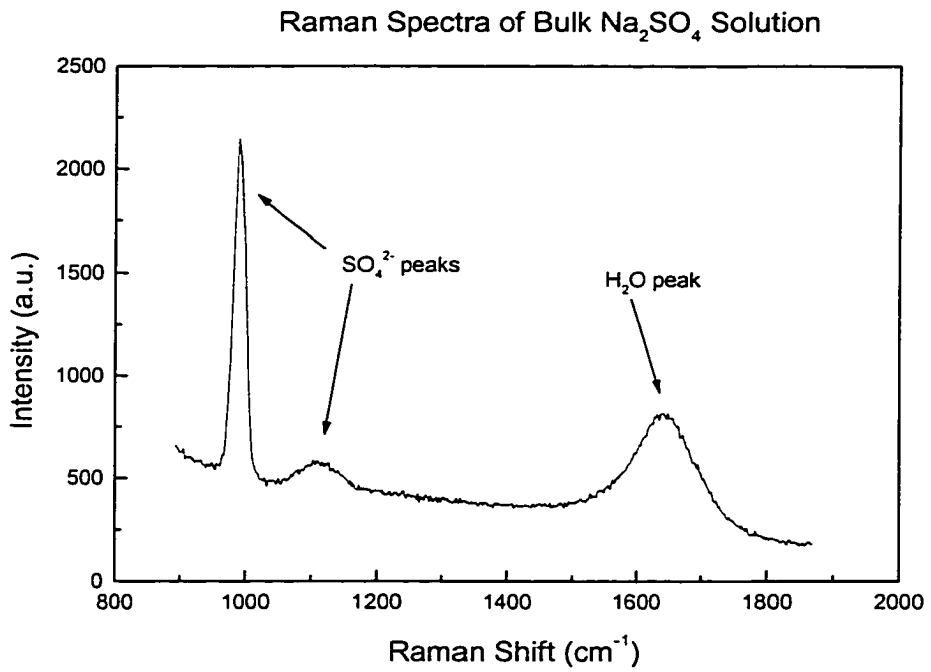

Figure 3.4 Bulk sulfate calibration using 2M Na_2SO_4 in a bulk solution at 25 °C for the high-resolution diffraction grating. The sulfate peaks are located at 980 cm^{-1} and 1104 cm^{-1}.

The results of the calibration using the high-resolution diffraction grating are presented in figure 3.5 below. The sensitivity of the high-resolution grating allowed for a minimum detectable sulfate concentration of 0.003 M.

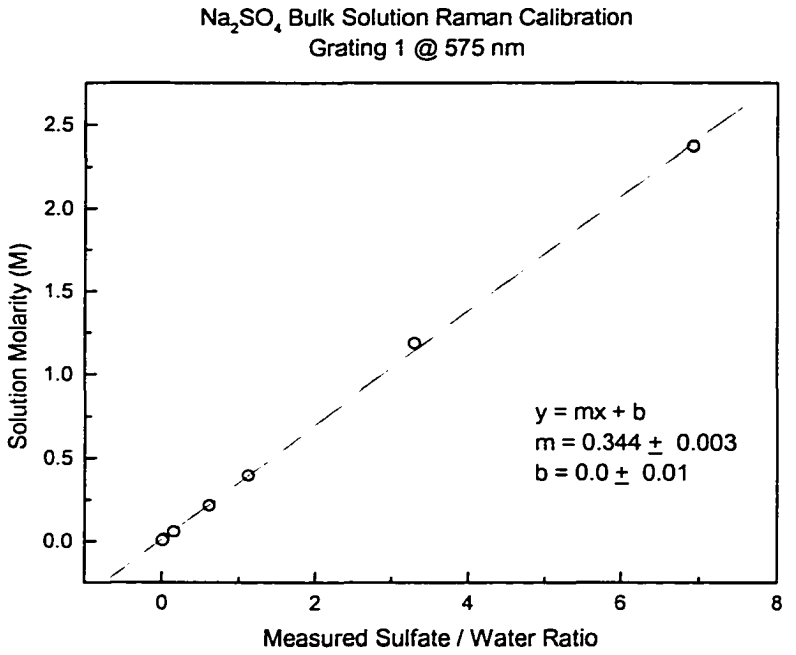

Figure 3.5 Bulk sulfate calibration using Na_2SO_4 in a bulk solution at 25 °C for the high resolution diffraction grating

3.3.2 Delivering the gases (SO_2, O_3, H_2O_2, NH_3)

The goal of these experiments was to use the flytrap instrument to measure sulfur dioxide oxidation rates in aqueous sea-salt aerosols under conditions found in an environment similar to the marine boundary layer. To that end a method for delivering various mixing ratios of sulfur dioxide, ozone and hydrogen peroxide to the trap under high humidity levels had to be developed.

Aqueous particles injected into the trap, like sea-salt aerosols injected into the atmosphere will quickly equilibrate with the background relative humidity. In order to study heterogeneous chemistry of aqueous aerosols, the relative humidity in the chamber surrounding the trap must be well controlled and well characterized. The easiest way to control the relative humidity was with a saturator system in which dry, contaminant-free air was mixed with air bubbled through a water saturator in a well-characterized ratio as described in chapter one of this work.

Creating ozone in a controllable manner on the other hand proved to be somewhat more challenging. Several techniques were attempted including utilizing a corona discharge to produce oxygen radicals in an airflow (see chapter 4 for a complete discussion). The technique that was eventually used involved an ultraviolet pen lamp placed next to a quartz tube with zero air flowing through it. The radiation from the UV lamp split apart O_2 into O atoms, some of which recombined with molecular oxygen to produce O_3.

$$O_2 + h\nu \rightarrow O + O \qquad \text{Equation 3.15}$$

$$O + O_2 \rightarrow O_3 \qquad \text{Equation 3.16}$$

$$O_3 + h\nu_2 \rightarrow O_2 + O \qquad \text{Equation 3.17}$$

The Spectroline 11SC-2 Quartz pencil lamp used was a small, low-pressure mercury vapor discharge lamp made of double-bore material with both electrodes at one end. The lamps proved to be very stable and maintained a high output of ultraviolet radiation over several hours. The pencil lamp had a spectral emission characteristic of a low-pressure mercury discharge consisting of many well-separated lines in the ultraviolet, visible and infrared parts of the electromagnetic spectrum.

A schematic of the device to produce O_3 is shown in figure 3.5 below. Airflow through the quartz tube was on the order of 2-6 liters per minute, most of which was dumped to an exhaust line, and about 10 cm^3 per minute was mixed with air flowing from the humidifier. The output of the ozone generator was quantified with the assistance of Terry Rawlins at Physical Sciences Inc., for several lamp intensities and zero-air flow rates. The configuration used in the following SO_2 / sea-salt experiments produced an ozone mixing ratio of approximately 500 ppb(v). When mixed with humidified air, sulfur dioxide and zero air, the ozone generator could produce O_3 mixing ratios of approximately (60 ± 10) ppb(v) at a relative humidity of (79±5) %. Details of the calculations can be found in the appendix in the form of a MathCad sample worksheet.

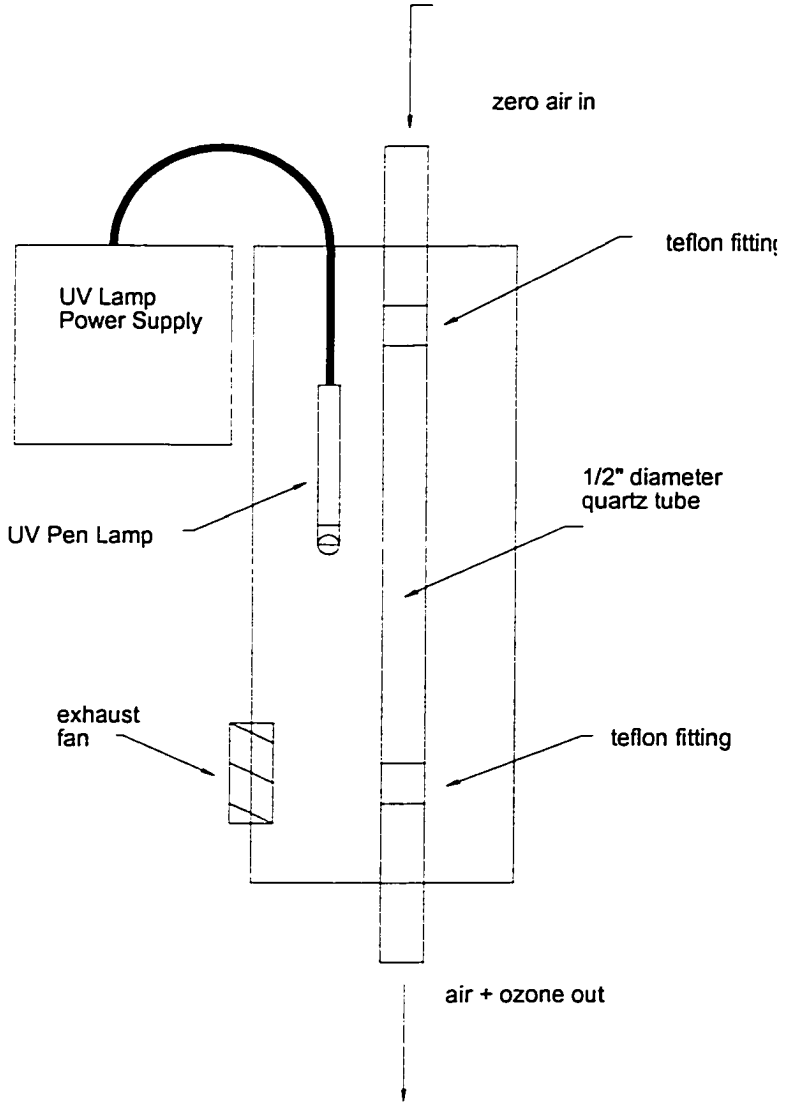

Figure 3.6 Schematic for the generation and delivery of O_3 laden air used in the oxidation experiments. A Spectroline 11SC-2 Quartz pencil lamp was used as a UV source to produce the oxygen radicals.

Sulfur dioxide and ammonia used in the following experiments were supplied to the quadrupole trap chamber by utilizing compressed gas cylinders filled with 1 ppm(v) SO_2 and 1 ppm(v) NH_3 respectively. Sulfur dioxide mixing ratios of 60 ppb(v) to 10 ppb(v) could be generated when mixed with air from the saturator, the ozone generator and dilution air.

Introduction of hydrogen peroxide into hydrated sea-salt aerosols was somewhat simpler. Instead of purchasing a compressed gas cylinder filled with hydrogen peroxide vapor, a solution

of 3% (by weight) hydrogen peroxide was used and mixed with NaCl. This solution was then pipetted into the microparticle injector. Several experiments were conducted with bulk solutions of 3% H_2O_2 in H_2O / NaCl. This concentration in the aqueous phase represents a gas phase mixing ratio of 24 ppm(v) based on the Henry's Law constant of $2.0x10^3$ for hydrogen peroxide at 293K. Clearly, the peroxide in these experiments was not the limiting factor in oxidation reactions. As long as the water in the aerosol did not evaporate to a substantial degree, the hydrogen peroxide did not evaporate. As an added measure against H_2O_2 evaporation, the trap chamber was well humidified throughout the aerosol injection process.

3.4 Conducting the Experiments and Collecting the Data

Before an attempt to observe oxidation of dissolved sulfur dioxide by ozone and hydrogen peroxide, several preliminary experiments were conducted in order to verify system performances and capabilities. A short set of experiments was conducted to insure that a sulfate and water peak could be observed in a single Raman spectrum using the high-resolution diffraction grating, and that the method could be used to calibrate the system in the bulk liquid phase. An attempt was made to observe the intermediate products of SO_2 dissolution in the aerosol phase, namely looking for Raman signatures of HSO_3^- and SO_3^{2-}. It was hoped that these products could provide information and diagnostics on aerosol pH and chemical kinetics.

3.4.1 Sulfur Dioxide / Ozone Results

To observe the properties of aerosol phase sulfate, a solution of 5.3 grams NaCl, 1.28 grams, Na_2SO_4 and 90 grams H_2O was prepared. The solution was introduced to the microparticle injector and an aerosol created from this solution was injected into the quadrupole trap. The aerosol was hydrated at a relative humidity of 90% and observed with the Raman system. Unlike the nitrate experiments, this aerosol had substantial amounts of fluorescence in left-hand side of spectrum below 1000 cm^{-1}, (near pixel 100). It was not just this aerosol that

exhibited this behavior; dozens of similar aerosols were injected into the trap and displayed untenable amounts of fluorescence. A sample spectrum exhibiting this fluorescence is shown below in figure 3.7. The radius of this particular aerosol was (12.5±1.2) μm, based on the results of a Mie scattering analysis.

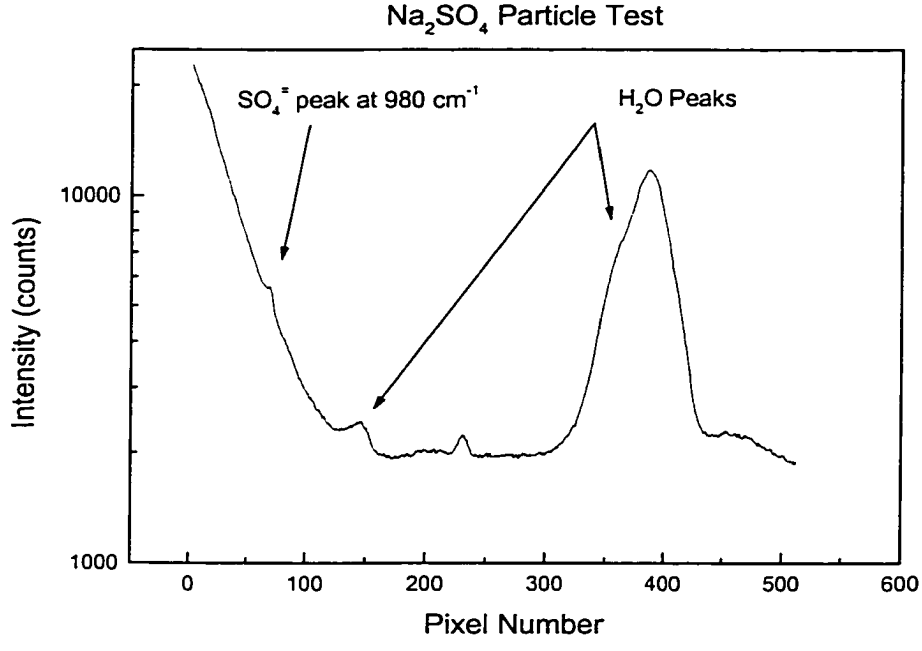

Figure 3.7: Raman spectrum of Na_2SO_4 aerosol in trap using low resolution grating. Large fluorescence problem can be seen on left of spectrum, much larger than the water peaks between 3000-4000 cm^{-1}. The spectrum is displayed using pixel number on the x-axis to aid in instrument diagnostics.

In order to insure that this was not an instrument effect, the trap was cleaned thoroughly and replaced. The quartz windows to the trap chamber were cleaned as well as all the Raman optics. The optics were then replaced and realigned. The microparticle injector was cleaned and the fluid reservoir emptied and refilled with a newly mixed solution. A nitrate aerosol was injected into the quadrupole trap and it exhibited a similar fluorescence behavior as the sulfate aerosols. It was then decided to change the Raman gratings to the high-resolution mode to see if the problem persisted. The results of this etude indicated that the low-resolution diffraction grating had somehow become damaged and was irreparable. Using the high-resolution

diffraction grating meant using different methods and calibrations than those used in the previous nitrate experiments.

When an aerosol derived from a similar solution was injected into the trap and examined with the Raman system, a clean, easily identifiable sulfate peak at 980 cm^{-1} was evident. A sample spectrum is shown below in figure 3.8. The aerosol was repeatedly dried and re-hydrated in order to determine the volatility of the sulfate in the aerosol. No mass change of the aerosol was measured, nor any concentration change of sulfate was observed, indicating that any sulfate in the form of Na_2SO_4 would be permanent with respect to changes in ambient relative humidity.

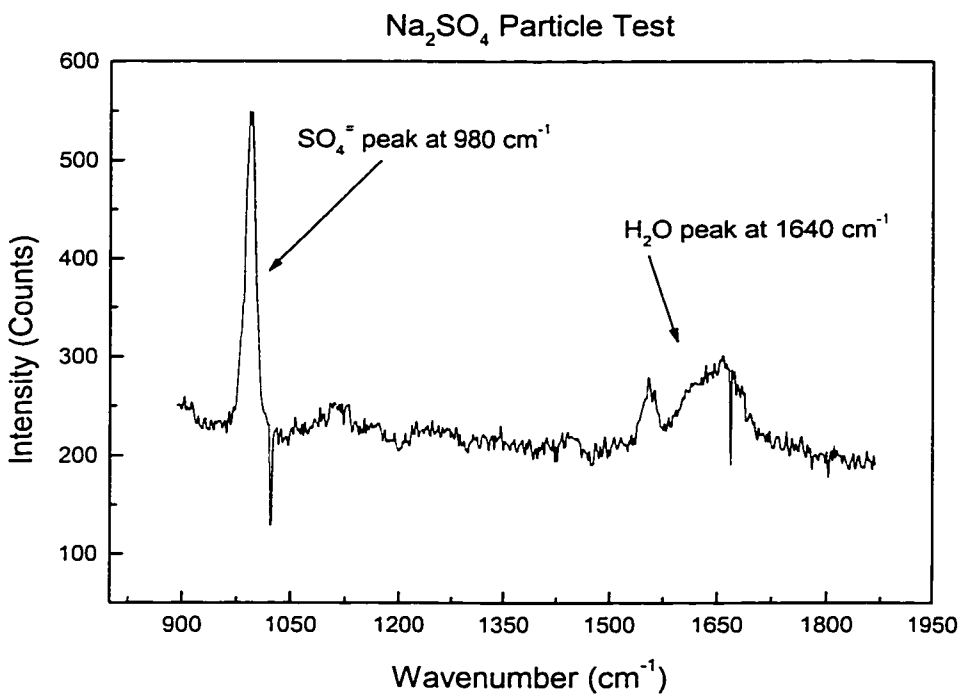

Figure 3.8: Raman spectrum of Na_2SO_4 aerosol in trap using the high-resolution diffraction grating.

The chemical and physical effects of subjecting aqueous NaCl aerosols to 64 ppb(v) of SO_2 vapor were examined. An aerosol created from a NaCl / H_2O solution was injected into the quadrupole trap, subject to 88% RH and 64 ppb(v) SO_2. Raman spectra were taken at 60 minutes,

120 minutes, 180 minutes and examined for signs of SO_2, $H_2SO^-_3$ and $SO_3^=$. There were no indications from the spectra that any of these species were present in the aqueous aerosol. No changes in aerosol mass or balance voltage were observed either. The expected concentration of SO_2 in the aqueous phase was estimated to be 3.2×10^{-5} M at a pH of approximately 4.4. (These estimates were based on Henry's Law and a solution to the electro-neutrality equation).

An aerosol created from a solution of NaCl and water was injected into the trap, hydrated and then subjected to SO_2 vapor at a mixing ratio of 35 ppb(v), O_3 at a mixing ratio of 61 ppb(v) at a relative humidity of 80%. Mie and Raman spectra were taken of the aerosol over a duration of four hours. No sign of sulfate production in the aerosol was observed. The final Raman spectrum of the series is shown in figure 3.9 below.

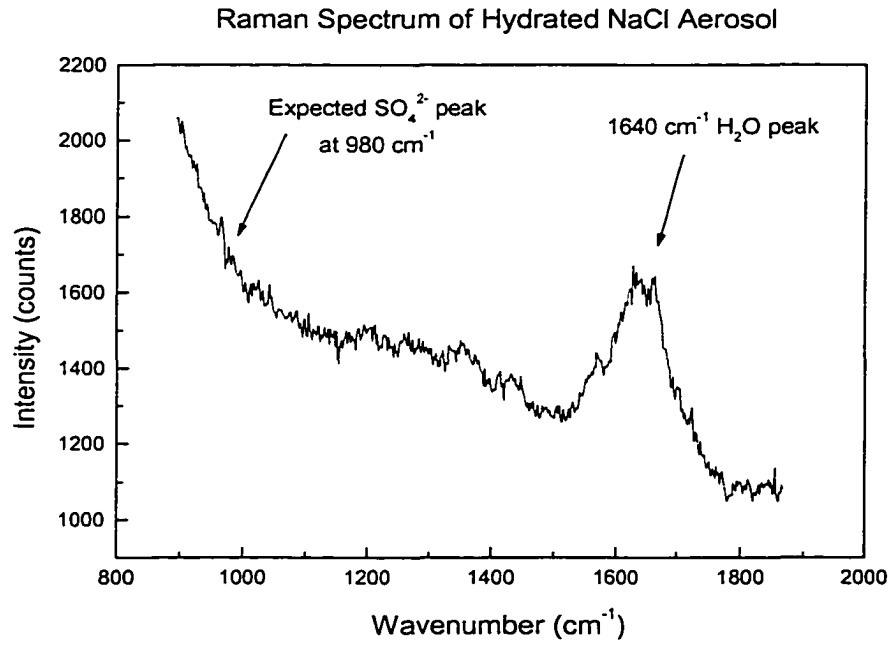

Figure 3.9 Raman spectrum of a hydrated NaCl aerosol that had been exposed to SO_2 and O_3 as an oxidant.

The experiment described above was repeated, but with a much larger aerosol in the quadrupole trap (18 μm radius). The initial and final Raman spectra of the series are shown in

figure 3.10 below. The time separating the two spectra was 240 minutes. The initial pH of the droplet was estimated to be 4.4.

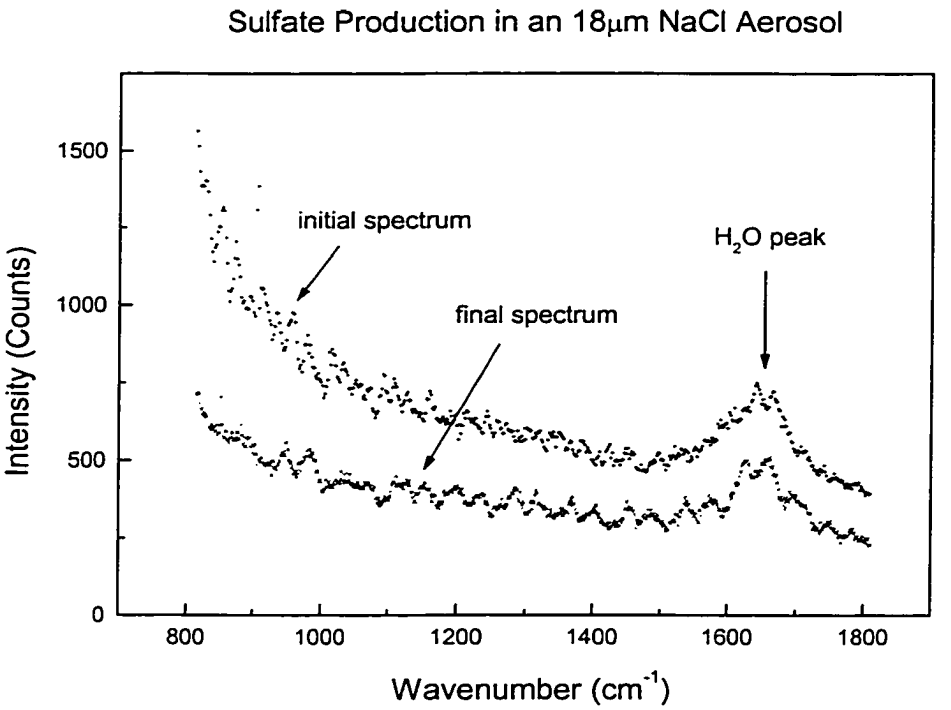

Figure 3.10 Two Raman spectrum of an 18 μm NaCl aerosol. No sulfate production was observed after an exposure time of 240 minutes. The aerosol had been subjected to 35 ppb(v) of ozone and 61 ppb(v) sulfur dioxide.

In a pure water droplet (no salts) the expected oxidation rate of SO_2 to S(VI) can be expressed by the following equation (Hoffman and Calvert, 1985)

$$R_0 = -\frac{d[S(IV)]}{dt} = (k_0[SO_2 \bullet H_2O] + k_1[HSO_3^-] + k_2[SO_3^{2-}]) \bullet [0_3] \qquad \text{Equation 3.18}$$

where $k_0 = (2.4\pm1.1)\times10^4$ $M^{-1}s^{-1}$, $k_1 = (3.7\pm0.7)\times10^5$ $M^{-1}s^{-1}$ and $k_2 = (1.5\pm0.6)\times10^9$ $M^{-1}s^{-1}$. As expected this relationship is extremely pH dependant (Seinfeld and Pandis, 1998). The oxidation rate is expected to increase as the pH increases. The strong increase of the reaction rate with pH will render the SO_2 / O_3 reaction self-limiting. The results of this experiment are discussed in

greater detail in section 3.5. It was thought that by increasing the aerosol pH with the introduction of alkalinity, sulfate production might be observed.

As with the nitric acid experiments, the easiest way to introduce alkalinity to a suspended aerosol in the quadrupole trap is by mixing $NaHCO_3$ into the NaCl solution placed in the microparticle injector reservoir. The bicarbonate buffers the aerosol against changes in solution pH as was demonstrated in the previous chapter. The aerosols used in this alkalinity experiment were created from a mixture of 0.2 M Na_2CO_3 and 0.3M NaCl. The aerosol was created and injected into the quadrupole trap where it was subjected to 20 ppb(v) SO_2, 39 ppb(v) O_3 at a relative humidity of 85%. Raman and Mie spectra were taken at various intervals during the experiment series. Several of the Raman spectra are shown in figure 3.12 below.

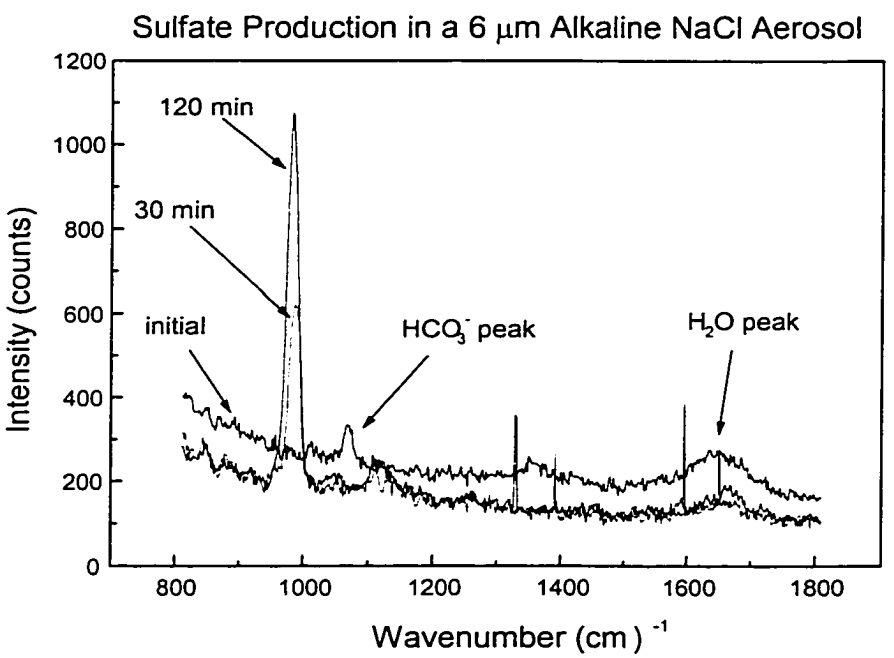

Figure 3.11 Raman spectra associated with sulfate production in a 6 μm alkaline NaCl aerosol at 293K and a relative humidity of 85%. Easily observable are the water peaks at 1640 cm^{-1}, the initial carbonate peak and the sulfate peak at 980 cm^{-1}.

At the following times, Mie and Raman spectra were simultaneously acquired. Analyses of the results are shown in Table 3.1 below. The sulfate concentration was calculated using the calibration curve shown in figure 3.5. A plot of sulfate concentration as a function of exposure time (to O_3 and SO_2) is shown in figure 3.13 below.

Sulfate Production in a 6 μm Alkaline NaCl Aerosol

Time	Radius (μm)	Sulfate (counts)	Water (counts)	Sulfate Conc. (M)
0	12.1 ± 1.2	0	6532	0.01 ± 0.10
900	9.4 ± 1.0	2844	3070	0.31 ± 0.14
1200	9.2 ± 1.0	3454	2605	0.45 ± 0.16
1920	9.5 ± 1.0	4904	3428	0.48 ± 0.17
3000	9.0 ± 1.0	16008	8076	0.66 ± 0.20
4800	9.8 ± 1.0	7265	3945	0.62 ± 0.19
6000	9.6 ± 1.0	12241	4948	0.83 ± 0.22
7000	9.6 ± 1.0	9608	3961	0.81 ± 0.22

Table 3.1 Sulfate Production in a 6 μm Alkaline NaCl Aerosol

The estimate of initial carbonate concentration in the aerosol was determined by measuring the initial mass and radius of the aerosol when it was completely dry and then fully hydrated, allowing for a calculation of the number of NaCl and Na_2CO_3 moles present in the aerosol. This calculation is demonstrated in one of the Mathcad worksheets located in the Appendix. The largest rate of change of S(IV) into S(VI) occurs within the first 900 seconds of the exposure. This rate was estimated to be $(3.5\pm0.7)\times10^{-5}$ M s^{-1}. The implications of this measurement are discussed in section 3.5. The concentration of chlorine ions in the aerosol was estimated to be nearly twice that of the carbonate ions. Clearly, removal of HCl as a buffer against pH changes in the aerosol did not occur.

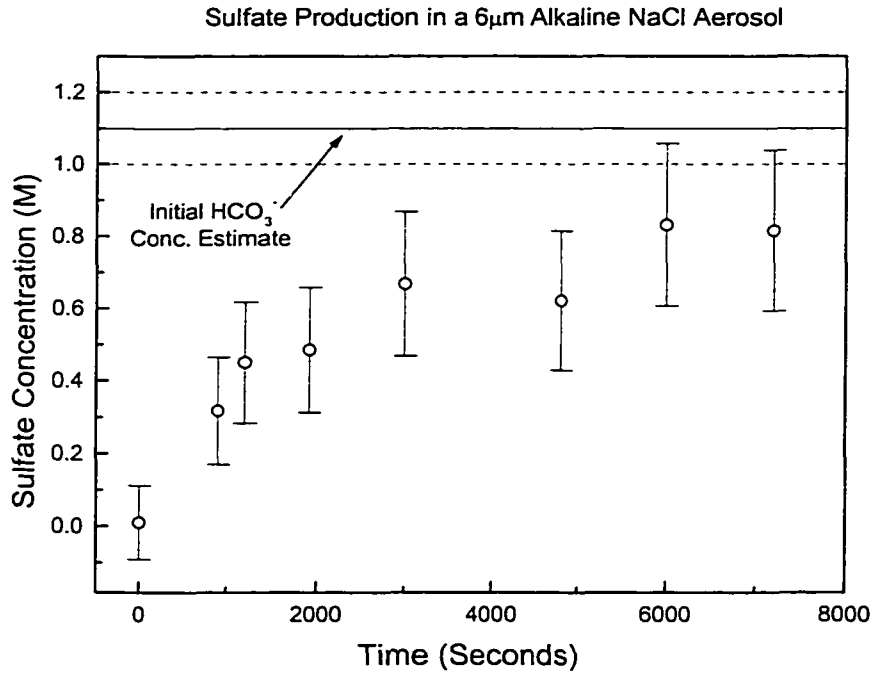

Figure 3.12 Time dependence of sulfate production in a 6μm NaCl aerosol spiked with carbonate alkalinity. The rate of sulfate production is clearly pH dependent and slows as the alkalinity of the aerosol is depleted.

Given the relative success of the first alkalinity experiment, it was thought that adding alkalinity into the aerosol via NH_3 vapor adsorption and dissolution would prove to be enlightening. A large difference between NH_3 experiment and the carbonate alkalinity experiment is (1) the initial pH of the aerosol and (2) the NH_3 vapor system delivers an unlimited supply of gas to the aerosol surface; it's not depleted as is with the carbonate ions.

As with other experiments, a solution created from NaCl and water was placed in the microparticle injector reservoir. The subsequent 7.8 μm aerosol was subjected to 95 ppb(v) SO_2, 40 ppb(v) O_3, 49 ppb(v) NH_3 at a relative humidity of 80%. Mie and Raman spectra were taken of the aerosol for duration of 3 hours.

Estimates of initial aerosol pH were calculated to be 6.6. This calculation was based on measured thermodynamic data for NH_3 and SO_2 dissociation in initially neutral cloud droplets and the solution to the electroneutrality equation shown below (Seinfeld and Pandis, 1998).

$$[H^+]+[NH^+_4]=[OH^-]+[HSO_3^-]+2[SO_3^{2-}]+2[SO_4^{2-}]+[H_2SO_4^-] \qquad \text{Equation 3.19}$$

Had the SO_2 not been present the initial (estimated) pH would have been closer to 8.8 (very basic). Had the NH_3 not been present the aerosol would have had an estimated pH of 4.3. With such low pH, it was not expected that the rate of SO_2 oxidation would have been very great. The last Raman spectrum obtained in this series is shown in figure 3.13 below. No signs of sulfate production were observed in this or any other similar experiment conducted using NH_3 as a source of alkalinity to the aerosols.

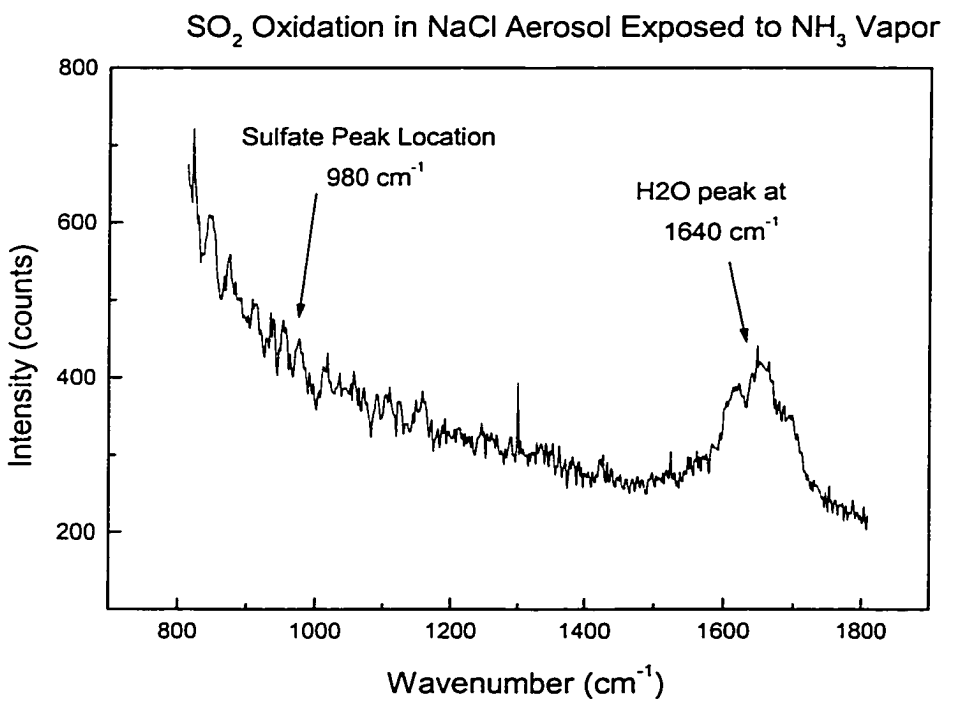

Figure 3.13 NaCl aerosol subjected to NH_3 and SO_2 vapor. No sulfate production was observed to occur during the observation period of three hours.

The conclusion that one can draw from this experiment is that at low pH values, ozone oxidation of SO_2 to $SO_4^=$ is not a very fast mechanism compared to using hydrogen peroxide as an oxidant. This is the subject of the next series of experiments.

3.4.2 Peroxide results

The expression for oxidation of S(IV) to S(VI) with H_2O_2 as an oxidant has been estimated to be

$$-\frac{dS(IV)}{dt} = \frac{k \cdot [H^+] \cdot [H_2O_2] \cdot [S(IV)] \cdot \left\{1 + \frac{[H^+]}{K_{S1}} + \frac{K_{S2}}{[H^+]}\right\}}{1 + K_{S1} \cdot [H^+]} \qquad \text{Equation 3.20}$$

where $k = (7.5 \pm 1.6) \times 10^7\ M^{-1}s^{-1}$ and $K_{S1} = 13\ M^{-1}s^{-1}$ at 298 K (Hoffman and Calvert, 1985). In that H_2O_2 is a weak electrolyte, it can be concluded that the rate of this reaction is independent of solution pH over the range if interest to atmospheric chemists (Seinfeld and Pandis, 1998).

Hydrogen peroxide exhibits a very strong feature at a wavenumber of $879cm^{-1}$, making it easily identifiable and quantifiable. H_2O_2 is however susceptible to decomposition when subjected to strong intensities of visible light (hence the dark bottles). The Raman laser was a superb instrument for destroying H_2O_2 in aerosols. This effect made quantification of H_2O_2 in the aerosol phase untenable by means of Raman spectroscopy. The HeNe laser used for Mie scattering however did not seem to have an effect on the amount of H_2O_2 present. A Raman spectrum of bulk phase (3%) H2O2 is shown below in figure 3.14.

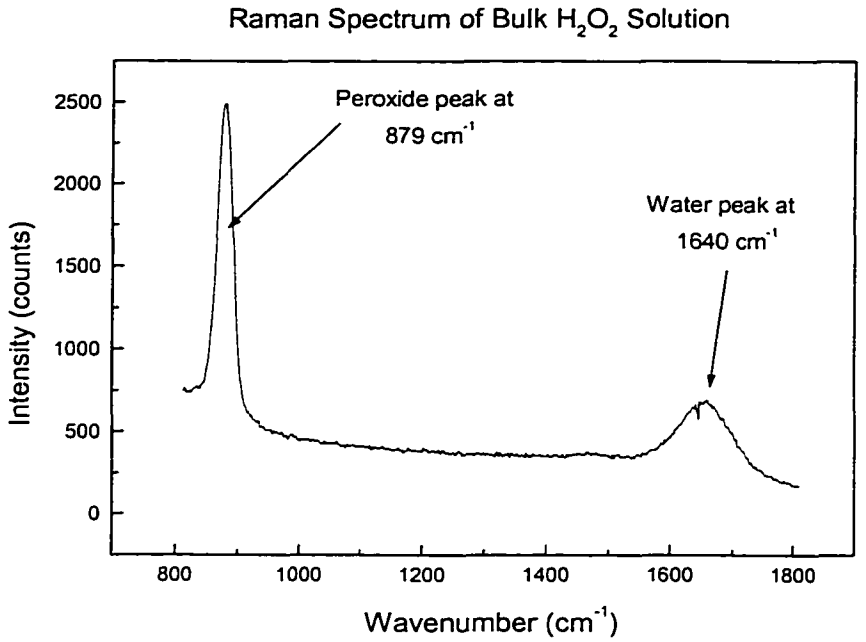

Figure 3.14 Raman spectrum of 3% (wt) hydrogen peroxide at 298K. The feature at 879 cm^{-1} was easily destroyed by high intensities of visible light (λ < 700nm).

To circumvent the problem of peroxide destruction, an aerosol with H_2O_2 was inserted into the trap and subjected to SO_2. After a certain time interval the SO_2 flow was closed and a Raman spectrum obtained. To obtain additional kinetic information another aerosol of (approximately) the same radius was injected into the trap and exposed for a different amount of time. In this manner, the oxidation rate of SO_2 to S(IV) with H_2O_2 as an oxidant was obtained for 30 minute, 60 minute and 120 minute time intervals. While the Raman laser did destroy any H_2O_2 present, it left the sulfate intact. A table of the data obtained is presented below while a sample spectrum of oxidized sulfur by hydrogen peroxide is presented in figure 3.16 below. It should be pointed out that great efforts were taken to present several aerosols that were identical in radius (within experimental possibility). Doing so eliminated one possible parameter in variation of results between the separate aerosols.

Time (sec)	Radius μm	Sulfate Counts	Water Counts	[Sulfate] M	d [S(VI)] /dt (M/s)
900	9.1	872	2406	(0.13 ± 0.01)	$(1.4\pm0.2)\times10^{-4}$
3600	8.4	4871	10208	(0.16 ± 0.01)	$(8.3\pm0.9)\times10^{-6}$
7200	9.6	1221	2544	(0.17 ± 0.01)	$(1.4\pm0.9)\times10^{-6}$

Table 3.2 Results of S(IV) oxidation by hydrogen peroxide in deliquescent NaCl aerosols.

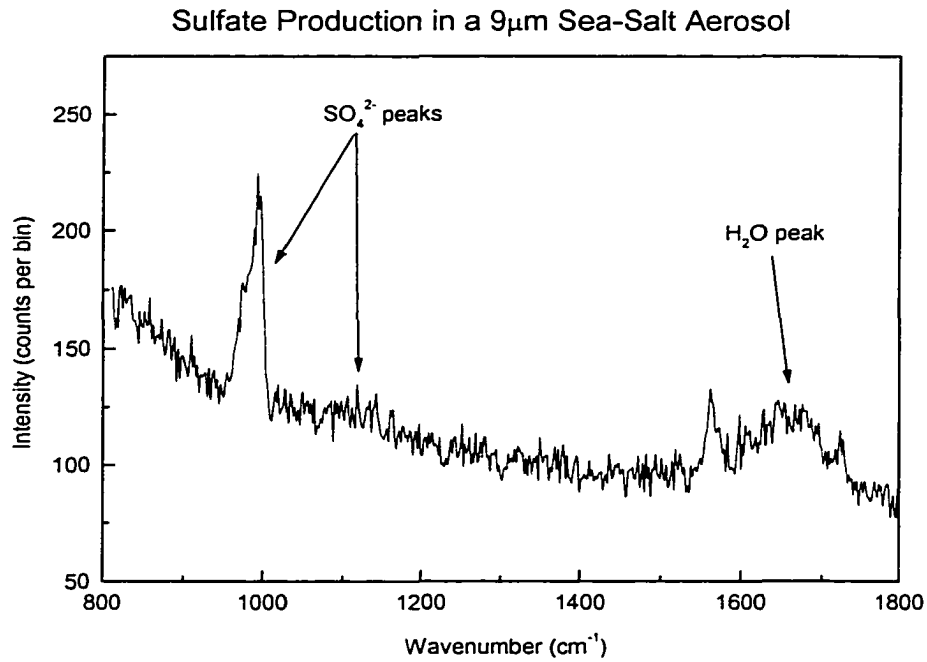

Figure3.15: Sulfate production in a 9 μm sea-salt aerosol. A 3% H_2O_2 mixture was used as an oxidant. The generated aerosol was subjected to SO_2 flow for a time of two hours with the system temperature at 298K.

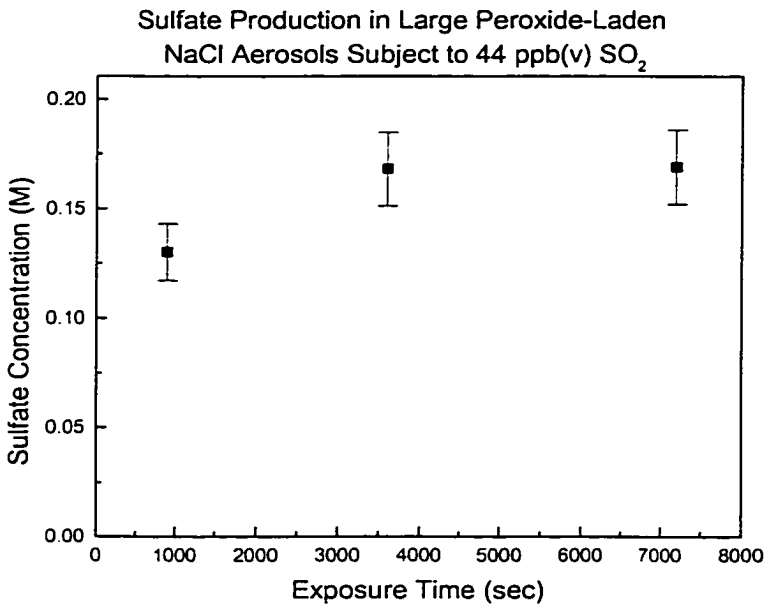

Figure 3.16 Time dependent behavior of sulfate production in sea-salt aerosol when hydrogen peroxide is used as an oxidant for SO_2.

As evident in figure 3.16 above, the oxidation of S(IV) to S(VI) proceeds extremely rapidly, much more so than that produced by ozone oxidation. Initial estimates of the amount of hydrogen peroxide in the aerosol were calculated to be (0.2±0.05) M. Without the Raman system to provide better quantitative information, H_2O_2 concentration had to be inferred from amounts of peroxide in the microparticle injector reservoir as well as thermodynamic data on H_2O_2 in cloud droplets. Further complicating matters was the fact that the relative humidity in the trap chamber was uncertain to within two percent. As the reaction proceeds, one can conclude that the limited supply of peroxide in the aerosol is consumed, the reaction quickly stops. Estimates of the time rate of change of S(VI) are provided in the last column of table 3.2.

3.5 Summary and Discussion

During the course of these experiments, it was demonstrated that sulfate, once present in NaCl aerosols was permanent. No changes in trace gas mixing ratios or changes in relative

humidity could cause volatilization of Na_2SO_4. The implication is that oxidation of dissolved SO_2 by any mechanism in sea-salt aerosol represents a permanent removal pathway of sulfur from the atmosphere.

No sulfate production was observed when an aqueous NaCl aerosol was subject to 35 ppb(v) sulfur dioxide concurrently with 61 ppb(v) ozone. An uncertainty analysis based on water Raman signals, noise in the Raman spectrum and calibration uncertainties yielded the result that (at a lower limit) a 0.05 M sulfate signal would not be detected. Anything larger would conceivably have a detectable signal with respect to the spectrum noise. During a four-hour exposure to ozone and sulfur dioxide, this yielded a lower limit of 3.4×10^{-6} M s^{-1} on the production of sulfate when the aerosol was at an approximate pH of 4.4. Compared to oxidation of SO_2 by H_2O_2, the ozone reaction is surprisingly slow.

The opportunity to observe the effect of Na^+ and Cl^- ions on the reaction rate (as with the nitric acid experiments) was not possible. It is thought, however, that the rate of S(IV)-O_3 reaction increases linearly with the ionic concentration of the salt solution (Lagrange et al, 1994). The ionic strength correction by Lagrange et al was reported to be $R = (1+FI)R_0$, where R and R_0 are reaction rates at ionic strengths I, and zero respectively. F is a parameter characteristic of the ions supporting the electrolyte ($F = 1.59 \pm 0.3$) for NaCl. Sadly, the attempt to verify this relationship could not be made during the course of these experiments.

The S(IV)-O_3 reaction was observed to proceed extremely rapidly when carbonate alkalinity was introduced to the aerosols under study. Time dependent measurements of this reaction were made. If was found that the reaction proceeded until the aerosol was depleted of alkalinity (via CO_2 escape – see figure 2.20 for the mechanism). In the natural atmosphere where SO_2 and O_3 coexist with natural sea-salt aerosols, the potential for removing large amounts of sulfur from the atmosphere exists. The calculations of Chameides and Stelson (1992) indicate that the rate of removal of SO_2 by sea-salt is quite significant and is roughly equal to the rate of DMS emission from the ocean. It is thus possible that much of the SO_2 produced from DMS

oxidation is removed by sea-salt and returned to the ocean before it has had a chance to be converted to CCN sulfate particles. This however would not be the case if the aerosols were highly acidic due to uptake of anthropogenically created nitric acid.

When the carbonate alkalinity was replaced with ammonia, there was no observed end product to the S(IV)-O_3 reaction. A similar uncertainty analysis provided the estimate that a 0.05 M signal could have been lost in the spectrum noise. This result yields a lower limit on the reaction rate of 4.6×10^{-6} M s^{-1} when the aerosol is at a pH of approximately 6.

Attempts at observing hydrogen peroxide in aqueous aerosols with the Raman spectrometer proved to be ineffective due to the tendency of H_2O_2 to break down under high intensities of visible radiation. The problem of obtaining time-dependent information on the S(IV)-H_2O_2 reaction was circumvented by using identical aerosols subjected to SO_2 vapor for various exposure times. The observed S(IV)-H_2O_2 reaction rates were very rapid with respect to the S(IV)-O_3 rates. Field measurements and theoretical studies indicate that H_2O_2 and SO_2 rarely coexist in clouds and fog (Faust, 1994), (Gunz, D.W., M.R. Hoffman, 1990). The species with lowest mixing ratio before a phase transition is expected to be the limiting reactant and rapidly depleted inside cloud droplet or aerosols (Seinfeld and Pandis, 1998).

Many experimental parameters were not varied in the study of oxidation rates of SO_2 in sea-salt aerosols, one of which is temperature. For most experiments conducted in this series, the lab and experiment temperature was kept constant at 298K. The variation of temperature could have a profound effect on the S(IV)-O_3 and S(IV)-H_2O_2 reaction rates. The expected effect of changing the temperature on the reaction rates for hydrogen peroxide is explored below briefly.

Henry's law for H_2O_2 is of the form

$$\left[H_2O_2\right]_{aq} = K_H P \qquad \text{Equation 3.21}$$

where K_H is the proportionality constant (Henry's law constant), P is the partial pressure of H_2O_2 in the atmosphere and $[H_2O_2]_{aq}$ is the aqueous phase concentration. The K_H has a temperature dependence however given by

$$K_H = e^{(\frac{a}{T}-b)} \qquad \text{Equation 3.22}$$

A quick calculation using a = 6621, b = 11.00, T = 298 K and a partial pressure of H_2O_2 gives a value of K_H of $1*10^5$ M atm^{-1} leading to a value of $[H_2O_2]_{aq}$ of $1*10^{-4}$ M. These values agree closely with published values. K_H, for a range of temperatures found in the marine boundary layer around the globe (273 K < T < 303 K) has a profile shown in figure 3.18 below. A graph of $[H_2O_2]$ as a function of temperature is shown in figure 3.19.

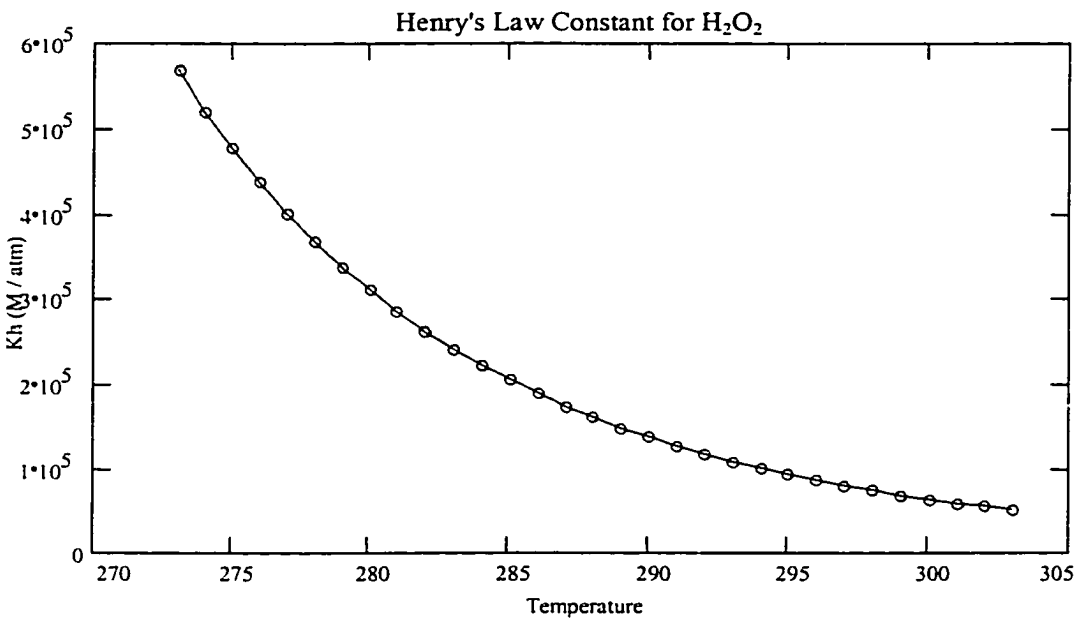

Figure 3.17. Henry's law constant for a temperature range found in the MBL. The H_2O_2 is much more soluble in the colder air, as expected.

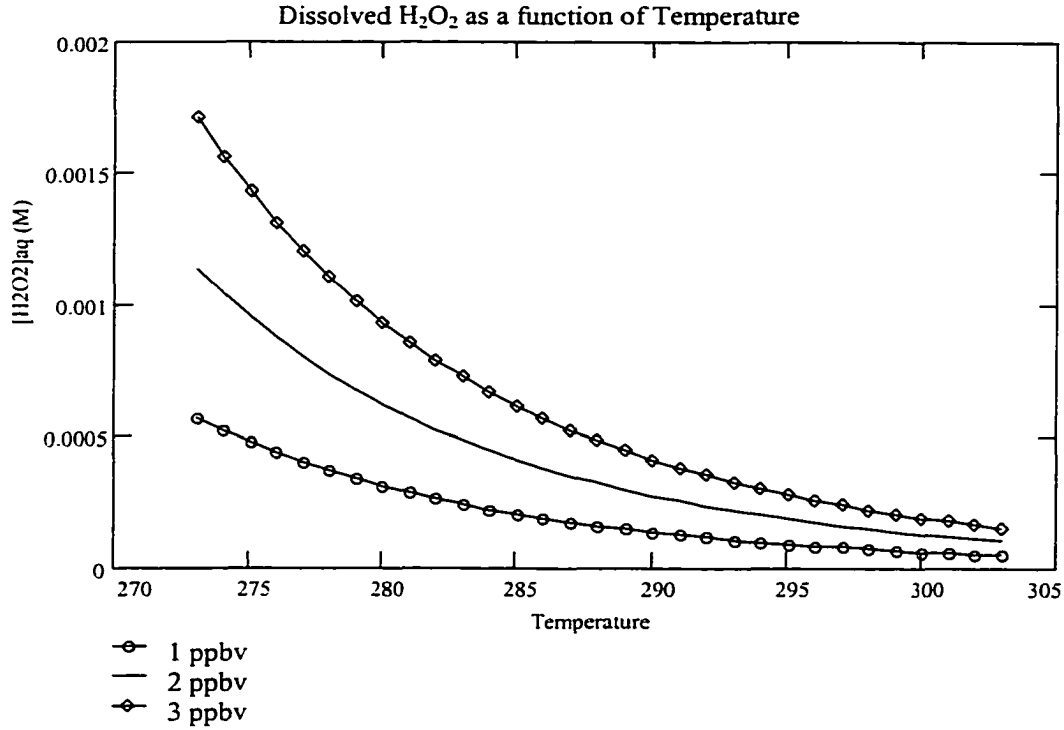

Figure 3.18: The effect of temperature changes on the aqueous phase concentration of hydrogen peroxide for several different mixing ratios.

The results of the calculations presented in figure 3.19 are also not unexpected, given the nature of Henry's Law. These results closely agree with published values. It should be noted that due to its weak dissociation behavior, there is no effect that pH has on the solubility of H_2O_2 in water. The review paper by Gunz and Hoffmann (1990) makes no references to a pH effect either. Given the solubility of H_2O_2, one would expect that an aerosol containing water would quickly scavenge it out of the gas phase. The solution pH does however play a role in the dissolution of SO_2 and the subsequent mole fractions of S(IV).

Using the equation 3.23 below calculations of the concentrations of S(IV) as a function of pH and temperature were made.

$$[S(IV)] = K_{hs} \cdot p_{so2} \cdot \left[1 + \frac{K_{S1}}{[H^+]} + \frac{K_{S1}K_{S2}}{[H^+]^2}\right] \qquad \text{Equation 3.23}$$

where K_{hs}, K_{s1} and K_{s2} are the temperature dependent Henry's Law constants for SO_2, HSO_3^- and $SO_3^=$ respectively. The equilibrium concentration of dissolved S(IV) were estimated and the results are shown below in figure 3.23 Temperature used in the calculations while generating the plot below was 298 K. If the temperature is decreased to 288 K, it was expected that a slight increase in the concentration of the S(IV) species would occur. It would appear that pH has a greater affect on the concentration of S(IV) species than does the temperature.

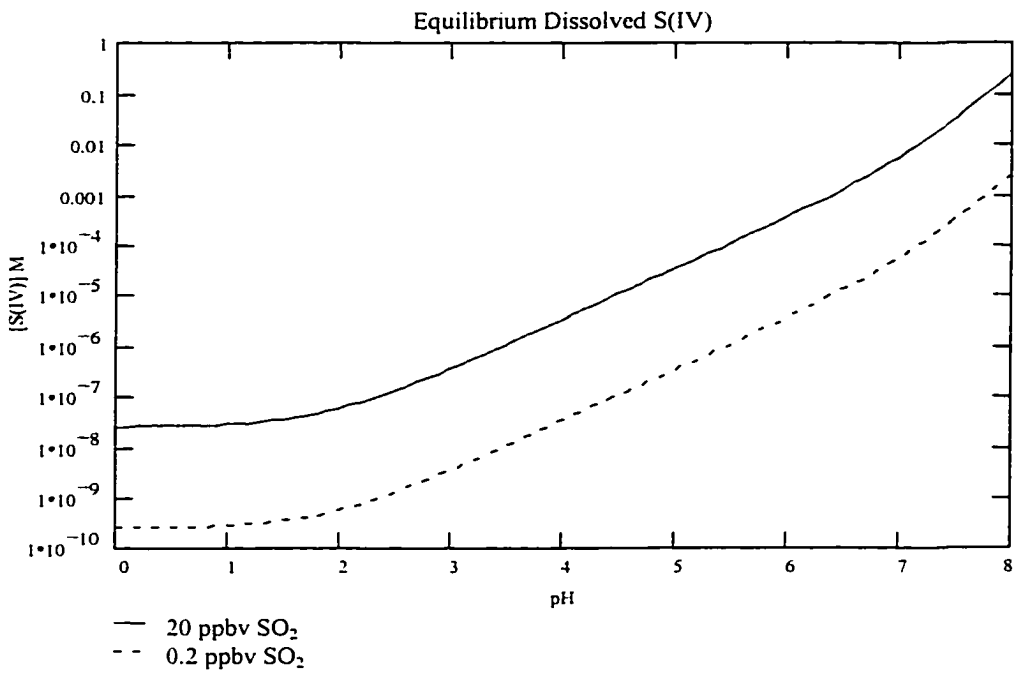

Figure 3.19 Concentration of equilibrium S(IV) species as a function of aerosol pH for two concentrations of sulfur dioxide.

The natural buffering capacity of seawater, hence sea-salt aerosols means that the aerosols are capable of sustaining large amounts of sulfate production through the oxidation of sulfate by ozone. The buffered sea-salt aerosols possess a high pH allowing the reaction to proceed at a substantial rate. The progress of this reaction is apparently limited by the availability of the carbonate buffer, which once overwhelmed, allows the aerosol pH to fall and consequently the rate of sulfate production to slow.

CHAPTER 4

AEROSOL CHARGING AND TRAPPING EXPERIMENTS

4.1. Rationalization

In order to use flytrap as a field and aircraft based instrument, the atmospheric aerosols sampled must have a large electric charge in order to be captured by the quadrupole trap. The charging mechanism must be able to electrically charge the aerosols without changing their physical or chemical characteristics. Because the electrical force of the quadrupolar trapping potential is proportional to aerosol charge, greater particle charges lead to more effective trapping. Previous experiments with the microparticle injector lead to aerosols with applied charges of 10^4 to 10^6 electrons. There are very few mechanisms that can charge aerosols to these high values without perturbing their chemical and physical characteristics (Carleton et. al, 1995). To this end, a method for charging and capturing atmospheric aerosols needed to be developed. At the time, field-charging aerosols using a corona discharge and an electric field seemed to be most promising.

In this application, it was desirable to charge the aerosols in a gas (air) stream without being deposited to the walls of the flowtube. After being charged, the aerosols would flow down towards the trap for capture and optical characterization. The principles behind the corona charger operation, mechanical and electrical design and the laboratory testing of this device are described in the following sections.

4.2. A Brief Review of Field Charging Theory

In the simplest form of a corona discharge, a small diameter wire or a sharp needle is biased to a high voltage relative to a nearby plate, which is electrically grounded. The voltage creates a local breakdown of the ambient gas, which in turn generates charged molecular species. Once created, these ions can be spatially directed with additional electric fields. Altering the polarity of the voltage applied to the small wire can create both positive and negative corona. This creates a discharge region filled with predominately positive or negative ions. Directing an aerosol laden gas stream through the ion region can result in a large electrical charge on the aerosols (diffusion charging). An even higher electrical charge on the aerosol can result if the ions are subjected to a large external electric field. The result is a large number of ions are driven onto the aerosol surface with a large external electric field (field charging). This method of charging aerosols is typically found in electrostatic precipitators.

In order to maximize the probability an aerosol will be stopped in the quadrupole trap, the charge on the aerosol must be as large as possible. There is however, an upper limit to the amount of charge that can be driven onto an aerosol using an electric field. According to the theory of field charging (White, 1954), an aerosol in a specified electric field configuration will charge to a maximum value, known as the saturation charge. The first electron applied to the surface of the aerosol has no work done on it due to a lack of electric field set up by the aerosol. The next electron must overcome the field setup by the first electron. The more charge applied to an aerosol, the stronger the field subsequent ions must overcome in order to reach the aerosol surface. The saturation charge of an aerosol is a function of electric field strength, particle radius and particle chemical composition (dielectric constant). The applied saturation charge q_{sat} (coulombs) for a given particle in a given electric field configuration can be estimated by

$$q_{sat} = 4\pi\varepsilon_0 \frac{3\varepsilon_p}{2+\varepsilon_p} E_0 a^2 \qquad \text{Equation 4.1}$$

Where a is the particle radius, E_0 is the peak amplitude of the electric field (in volts per meter), ε_p is the dielectric constant of the aerosol material and ε_0 the permittivity of free space. Figure 4.1 below illustrates the applied particle charge amount as a function of particle diameter for a 2kV field. The calculation was carried out using the dielectric constant for droplets composed of latex (polystyrene) and water.

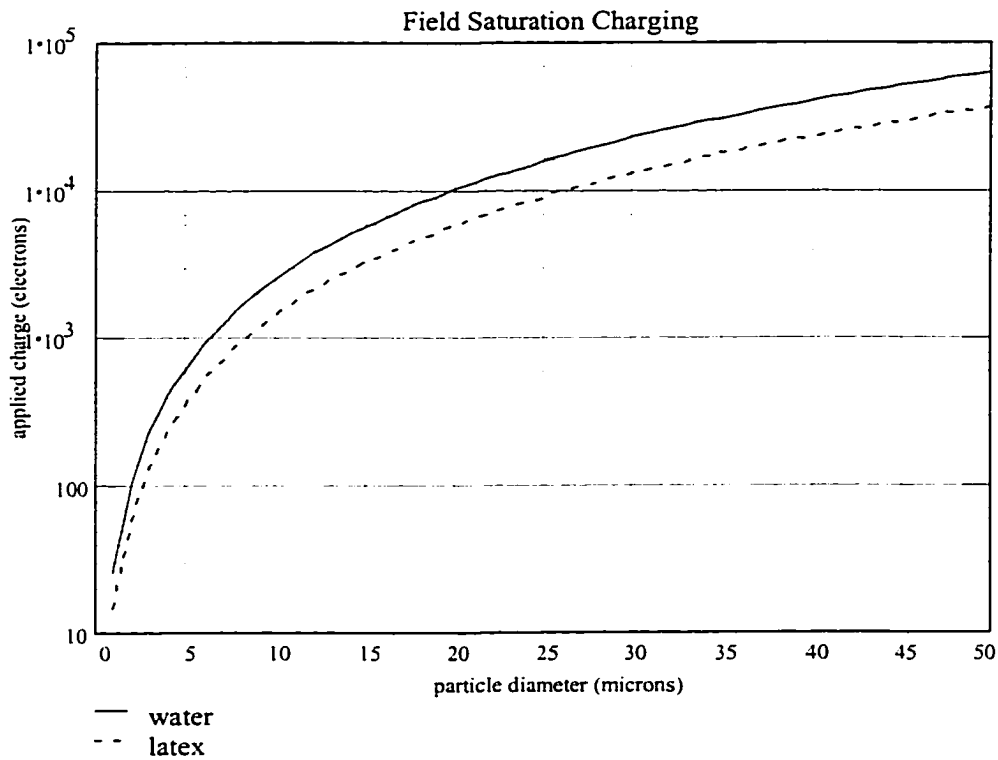

Figure 4.1: Particle saturation charge as a function of particle radius, for both water and latex spheres in a 2kV external electric field.

As given by equation 4.1, the saturation charge of an aerosol is dependent on several variables: (1) the amplitude of the electric field driving the ions onto the aerosol, (2) the chemical composition of the aerosol and (3) the surface area of the aerosol. It is apparent from figure 4.1 that larger aerosols will have a larger saturation charge. Classical electrostatics predicts that a charge applied to a dielectric sphere will reside on the exterior of the sphere in

order to minimize the potential energy of the charge configuration. It is expected then that the saturation charge is a function of aerosol surface area. Assuming a uniform density, the mass of the aerosol, however, is a function of the radius cubed. The charge to mass ratio (q/m) will therefore be inversely proportional to the radius of the aerosol. This relationship played an important role in the final design of the corona charger.

As the aerosol becomes charged (q), it is now susceptible to electric force (F_{elec}) set up by the electric field (E) as given in equation 4.2.

$$F_{elec} = Eq \qquad \text{Equation 4.2}$$

For a charged saturated particle in a kilovolt electric potential these forces are large indeed. A large electric force on an aerosol of finite mass has the effect of violently pushing the aerosol in the direction of the electric field. The goal was to design a charging mechanism that applied a large (10^6) electron unit charge to an atmospheric aerosol, while maintaining control of the motion. Charging the aerosol to a high degree, maintaining control of the aerosol motion and minimizing chemical and physical perturbations proved to be a formidable and daunting task.

4.3. Mechanical and Electrical description of charger

Hutchins and Holm [1989] claimed to have developed a fairly sophisticated design that maximizes particle charging while minimizing particle deposition. Using a field charging mechanism they claimed they could highly charge micron sized latex spheres that were seeded into a gas stream. The aerosol charger developed for flytrap applications was based heavily on their design.

The centerpiece of the flytrap charger design consists of two aluminum plates that house several small cylindrical cavities containing corona discharge wires. The two aluminum plates are biased to a very large AC voltage. By applying an AC potential to these plates, molecular

ions created with the corona discharge are swept out of the cylindrical cavities and directed across the space between the two plates. A gas flow containing aerosols is directed vertically downward between the AC charging plates such that the molecular ions impact and charge the aerosols. As the aerosols charge up, they will be attracted to the large aluminum charging plates. By using a high-frequency AC potential on the plates, the charged aerosols will be alternately attracted to each plate, resulting in very little net motion to either side. A high frequency minimizes chances of aerosol deposition to the wall of the charger chamber or the AC charging plates. A schematic is shown in figure 4.2 below. It was thought that by varying the AC voltage amplitude, frequency, gas flow velocity and corona current it would be possible to maximize aerosol throughput as well as applied charge.

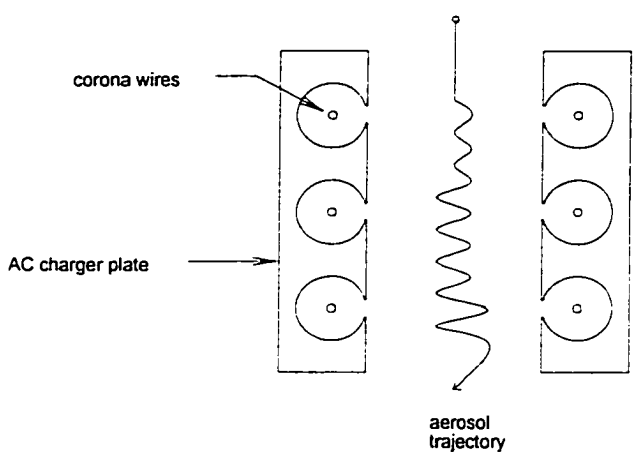

Figure 4.2: Cross section of aerosol charger. AC charger plates are held to 1-10 kV AC voltage, with the corona wires floating ~1000 volts (DC) above that. Aerosols to be charged are passed between the two charger plates.

The AC charging plates were machined from 31-30 aluminum stock to measure 1 x 3 x 3/8 inches. The cylindrical cavities containing the corona wires are ¼ inch in diameter and run the length of the plates. The wires were constructed from 25 μm diameter stainless steel wire. Each plate assembly is held in a block of insulating lucite and secured to an aerosol duct section using brass standoffs and a mounting plate. The two charger plates are held such that the space between the plates is approximately ½ inch.

The entire charging mechanism is housed in a flowtube section similar to the section housing the quadrupole trap. The flowtube section housing the charging mechanism has a ½ inch quartz window for observing particle trajectory between the plates as well as the intensity of the corona discharge. The AC charging plates and the corona wires are connected to a specialized power supply by four SHV (super high voltage) vacuum feedthroughs and custom-made SHV cables.

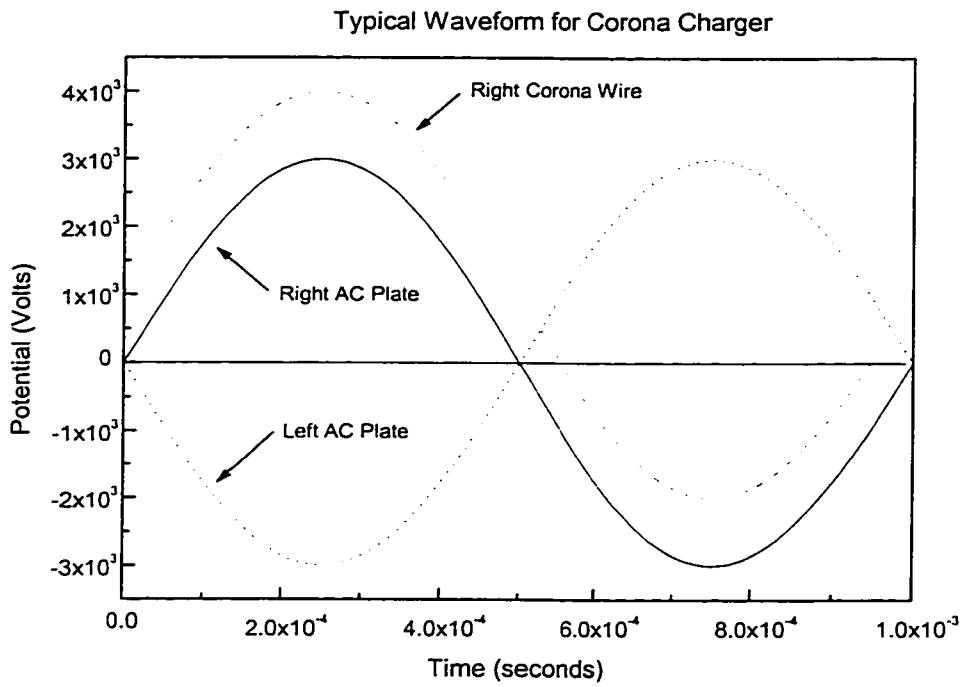

Figure 4.3 Typical voltages produced by corona charging circuit.

The voltages needed to operate the corona charger are fairly complex. A typical phase diagram of voltages as a function of time delivered to the charger is shown in figure 4.3 above. In this example, the AC frequency is 1000 Hz; the AC amplitude is set to 3000 volts with the corona wires floating 1000 volts (DC) above that. It is this DC potential floating above the AC potential which creates the corona discharge. It should be noted that the potential of the left corona wire is not shown in figure 4.3 for the sake of simplicity. The two AC signals are exactly

180 degrees out of phase with each other. The result of this phase difference is an electric field with twice the amplitude with a minimal need for additional power or potential applied to the charger plates. According to field charging theory (White et al., 1954), doubling the electric field in the charging region has the effect of doubling the applied charge to the aerosol. Typical operating frequencies of the corona charger were held between 1000 and 3000 Hz, while the amplitude of the AC voltages were between 1000 and 10,000 volts. The number density of ions created by the corona discharge could be varied somewhat by applying a potential of 1000 to 3000 volts to the corona wires.

The electrical circuitry needed to create the waveform illustrated in figure 4.3 is also fairly complicated and was based loosely on the work of Hutchins and Holm (1989). The required waveform has its origin in a Wavetek FG2A function generator. The function generator was set such that it would emit a small 2-volt (peak to peak) AC signal at a specified frequency from 1 to 3 kilohertz. The signal from the function generator was then sent to a Radio Shack MPA-200 power amplifier where it was split into two separate channels and amplified to approximately 25 volts (peak to peak) at the same frequency. The resultant pair of signals is then sent to a rack mounted chassis containing additional charger electronics via BNC cables. This chassis contained the remaining components of the charger power supply.

Inside the charger power supply, each of these signals is split again into two for a total of four signals. Two of these signals are sent to high-voltage, three-terminal step up transformers and then directly to the AC charging plates with SHV cables. The other two signals are sent to two high–voltage, four-terminal step up transformers. The signals emanating from the four-terminal transformers are sent through a series of diodes and capacitors to quadruple the voltage and then rectify the AC signal into a DC voltage. This DC voltage is then superimposed on the AC signals and sent to the appropriate corona wires in the charger with SHV cables. The schematic for the corona charger circuitry is shown in figure 4.4. The final AC and DC voltages

sent to the charger could then be controlled through use of the two channel "volume" knobs on the Radio Shack power amplifier.

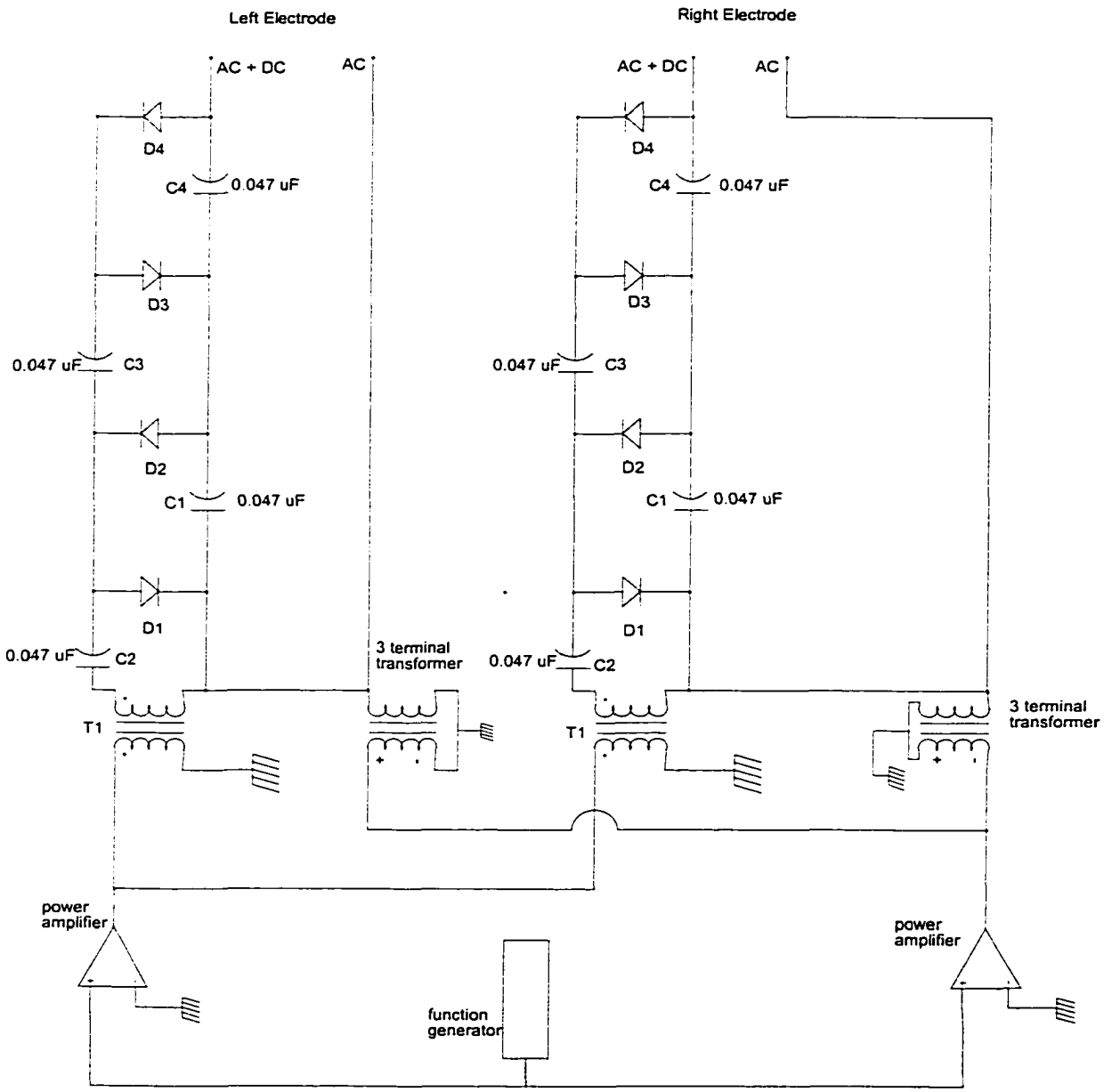

Figure 4.4 Modified circuit used for operation of the Flytrap instrument corona charger.

After the charging system was constructed and the circuitry assembled, the entire device was tested with a digital oscilloscope and high-voltage probe for correct waveform, frequencies

and voltages. Once this was accomplished, testing and experiments to optimize the operation of the charger were carried out.

4.4. Laboratory Setup For Corona Charger / Trap Experiments

As part of the experiments for evaluating Flytrap as a field instrument, a laboratory flow tube facility was designed and built to serve as a mock-up for the final aircraft based flowtube. These laboratory tests were designed and carried out to aid in determining the optimal operating conditions and the efficiency of the corona charger and trap. Figure 4.5 illustrates the schematic of the apparatus used to test the corona charger.

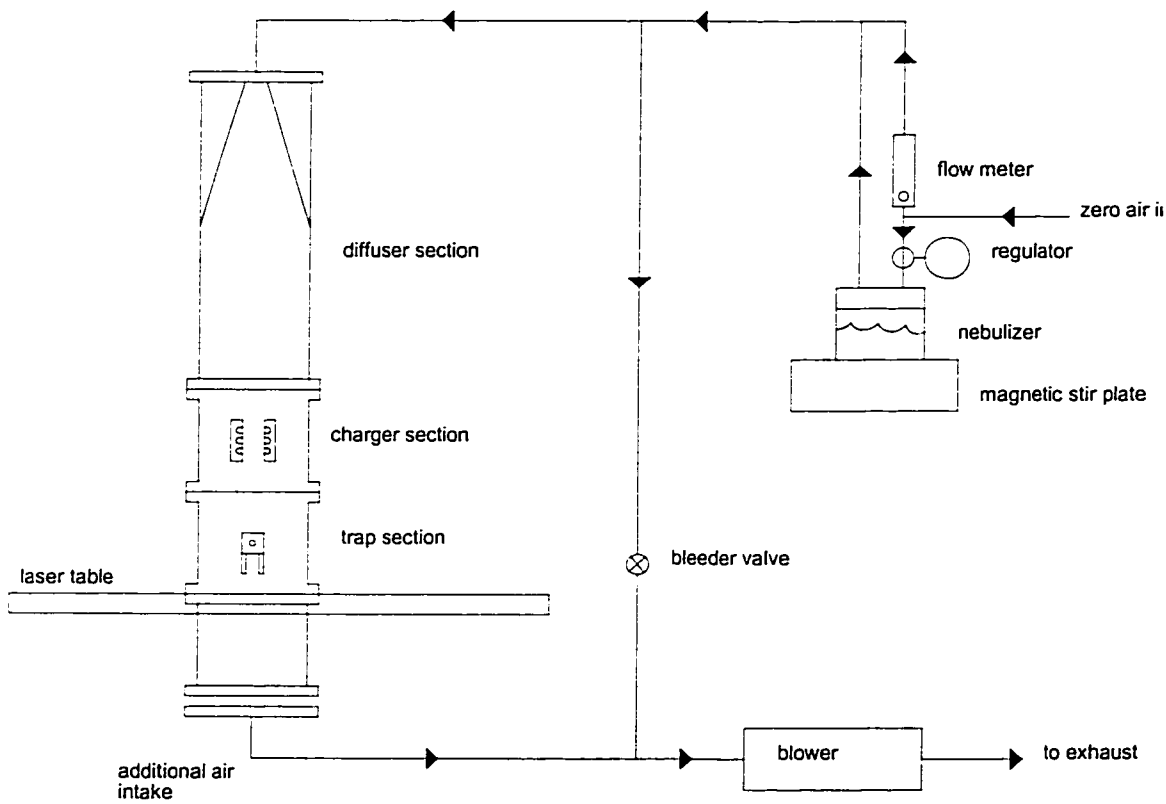

Figure 4.5 Schematic of the system used to test the corona charging apparatus.

Test aerosols were created through the use of a TSI Model 9302 Nebulizer. The nebulizer contained dilute solutions of polystyrene latex (PSL) or polydivinyl benzene (PDVB)

spheres obtained from Duke Scientific Inc. The sizes of the spheres used in this study are listed in table 4.1. The solution in the nebulizer was stirred by a magnetic bar to keep the sphere concentration fairly uniform and prevent the spheres from settling to the bottom of the reservoir. A minimum pressure of 5 psi was required to seed latex particles into the air stream. This resulted in a gas flow rate greater than 3 SLM. Drying air was added to this flow to evaporate excess water from the generated aerosols. The final flow containing a cloud of dry, single sized latex spheres was sent towards the flow tube assembly. When slower gas velocities were needed, a fraction of this flow was directed through a bleeder valve and dumped to the exhaust. This allowed for the required flow rates to completely dry the latex spheres but still control the gas and aerosol velocity in the flow tube. Flow velocities from 0.1 to 50 cm/sec were achieved this way.

Nominal Size (μm)	Standard Deviation (μm)	Material
0.966	0.013	PSL
3.7	0.11	PSL
5.3	1.2	PDVB
8.7	1.5	PDVB
10.2	1.9	PDVB
15.8	2.9	PDVB
23.4	3.6	PDVB
26.1	4.0	PDVB

Table 4.1: Different size latex spheres used in flow tube studies.

The flowtube assembly was a 7.5-cm diameter aluminum tube built in several sections. The flow tube design was tested using flow visualization with the HeNe or Nd:YAG lasers to learn about the uniformity of gas flow. This was accomplished by using a cylindrical lens to form the laser beam into a sheet. The sheet illuminated a slice across the flow that was then viewed with the lens/camera assembly. It was determined that the initial flow of air and dry latex spheres down the tube was turbulent and poorly characterized. The flow of air and spheres was smoothly expanded (and slowed) by adding a 35-cm long, 7-degree diffuser section to the

flowtube assembly. Visual observations of the spheres demonstrated that flow down the tube was fairly smooth and laminar.

Controlling the number density of latex spheres inside the flowtube was accomplished by adding fewer or more droplets of sphere/surfactant mixture to the nebulizer reservoir. The number density control was crude at best. Once introduced into the flowtube, the dried latex spheres were directed through the corona charger section, some of which went through the charging region. It was thought that a large number of these latex spheres would be highly charged when entering the trap section, some of which would be stopped in the quadrupole trap. The end of the flowtube was capped with a hood-like device to vent latex spheres and ozone (created by the corona charger) to an exhaust dump.

The task then was to adjust several experimental parameters in order to trap latex spheres easily, quickly and routinely. Table 4.2 contains a list of parameters and their ranges that were tested to optimize aerosol trapping conditions.

Parameter	Parameter Values
Latex sphere size	0.9 μm – 26 μm
Latex sphere number density	
Trap AC voltage	0-900 volts
Trap AC frequency	93 - 200 Hz
Trap DC voltage	0-200 volts
Flow velocity in trap	0-50 cm/sec
Flow velocity in charger	0-60 cm/sec
Corona discharge current	full, half, minimal, none
Charger AC voltage	0-5000 volts
Charger AC frequency	1000-3000 Hz
Trap – charger distance	2 cm, 6 cm, 15 cm

Table 4.2 A list of parameters controlled in charging and trapping experiments.

4.5 Summary of Charging and Trapping Experiments

Several experiments were carried out to determine whether latex spheres traveling down the flowtube would enter the quadrupole trap. Latex spheres of 0.9 μm, 3 μm, 8 μm, 15 μm and 23 μm diameters were injected into the flowtube using the atomizer delivery system and allowed to travel past the charger and into the trap section. All of the different diameters of latex spheres listed above were observed to enter the quadrupole trap from the top and exit through the bottom aperature. The velocity of the gas carrying the spheres through the flowtube was kept below 20 cm/sec. Once the velocity of the gas exceeded 30 cm/sec, turbulence around the exterior of the trap caused latex spheres to enter from the bottom of the trap and exit through the top. Placing aerodynamic shrouds constructed of PVC on the top and bottom of the quadrupole trap had little or no effect on the generation of turbulence and particle trajectory through the trap. This series of tests indicated that control of velocity in the flowtube had to be limited to below 20 cm/sec.

Once it was determined that latex spheres traveling down the flowtube would enter the trap orifice, several experiments were conducted to ascertain if the quadrupole trap potential well was strong enough to contain charged aerosols at these flow velocities. Several 23 μm and 15 μ m latex spheres were injected individually into the trap by hand. With only zero air in the flowtube, the gas velocity was varied between 0 cm/sec and 60 cm/sec. The latex spheres remained very stable in the trap until the velocity of the carrier gas was increased above 11 cm/sec. Above this point, turbulence caused the latex spheres in the trap to move around the potential well away from the trap stable point and away from the Raman laser focus point. Larger latex spheres in the trap were ejected once the gas velocity in the flowtube was increased beyond 50 cm/sec.

As a baseline for some of the experiments with the corona charger, attempts were made to ascertain if latex spheres could be trapped from a flow without the corona charger operating. Separate batches of 0.9 μm, 3 μm, 8 μm, 15μm and 23 μm diameter latex spheres were into

placed the nebulizer, mixed output with drying air and down the flowtube with the charger off and the quadrupole trap voltages turned on. It was hoped that some of the spheres would become slightly charged via friction with the atomizing apparatus, the air, with other spheres or with the flowtube walls and become entrained in the quadrupole trap. The individual batches of spheres were allowed to flow down the flowtube for approximately 5 minutes per run while the trap voltages were on. This experiment was repeated with the trap voltages set between 0 and 900 volts and several different flow velocities. The voltages on the DC endcap electrodes were also varied between -100 and +100 volts. The result of the experiment was the failure to trap even a single particle of any size, at any trap voltage, at any flow velocity.

Along these lines, several experiments were conducted to see if the electric fields set up by the quadrupole trap were excluding uncharged latex spheres via an induction mechanism. Spheres with a 15 μm diameter were placed into the nebulizer. For each run of this experiment, these spheres were mixed with drying air and sent down the flowtube at a nominal 10 cm/sec (with the charger completely shut off). The interior of the trap was observed with the aid of a TV camera/ zoom lens/ VCR assembly. The number of spheres entering the trap was tracked with the use of a handheld counter. The data from this experiment is presented in table 4.3 below. The conclusion from these experiments was that the AC electric field set up by the quadrupole trap does not interfere with the trajectory of uncharged latex spheres. The experiments were repeated with 8 μm latex spheres placed in the nebulizer with similar results.

AC Trap Voltage	0 Volts	400 Volts	600 Volts
Run 1	34 ± 6	26 ± 5	28 ± 5
Run 2	32 ± 6	32 ± 6	24 ± 5
Run 3	31 ± 6	34 ± 6	30 ± 6

Table 4.3 Data table for 15 μm latex spheres entering the trap orifice at 10 cm/sec.

Several additional experiments were carried out to insure that ion streams or the AC and DC electric fields used to operate the corona charger were not interfering with the fields necessary to hold a charged aerosol in the trap. A 15 μm latex sphere was injected tribologically into the trap. The corona charger voltages (both AC and DC) were increased to their maximum value and zero air was pumped down the flowtube at 10 cm/sec. The effect of this on the trapped aerosol was negligible: both the particle position and the particle balance voltage did not vary appreciably over several hours. This experiment was repeated with 8 μm and 23 μm spheres in the trap with the same result. The conclusion was that the "normal" operating range of the corona charger does not interfere with the ability of the quadrupole trap to hold an aerosol.

A question was posed as to whether or not the corona charger itself was responsible for an observed lack of charged latex spheres in the quadrupole trap. To answer this question 8 μm latex spheres were seeded into the nebulizer reservoir. After mixing the output with drying air, the spheres were sent down the flow tube at 7.5 cm/sec. The corona charger was configured such that both AC voltage plates were turned off and the DC corona wires were either off or held to the minimum potential necessary to create a discharge. The trap aperture was examined with laser and a TV camera/ zoom lens/ VCR assembly. Each time an 8 μm sphere entered the trap, a count was registered with a handheld counter. The following data were taken in 2 minute intervals:

Experimental Setup	Time	Counts
Trap Off Charger Off	2 min	34 ± 6
Trap Off Charger On (min)	2 min	6 ± 2
Trap On (600 v) Charger On (min)	2 min	12 ± 3

Table 4.4 The effect of a minimal DC corona discharge on aerosol throughput. The result is that a significant fraction of latex spheres in the flowtube are pulled out of the air stream when going through the corona charger when there is a minimal DC corona discharge.

The conclusion of this and similar experiments was that the discharge created with the DC corona wires were pulling large numbers of latex spheres out of the air stream. The deficit represented a large proportion of spheres traveling down the flowtube. When the voltage on the AC charger plates was increased from 0 volts to 1000 volts, the deficit was nearly 100%. Similar experiments with latex spheres of several sizes did not seem to alter the outcome of the experiment. Increasing the air flow from 7.5 cm/sec to 20 cm/sec had a slight positive effect in the number of particles that entered the trap when the DC corona discharge was operating in conjunction with the AC charger plates.

It was thought that the aerosol throughput would improve if the gas velocity between the charging plates was increased significantly. A pair of cylindrical venturis was machined to boost the gas velocity from 7.5 cm/sec to 30 cm/sec through the charger plates. Additionally, the fraction of latex spheres travelling between the plates was also increased by a factor of 60%. The half-angle on the venturis was set to be 9° to keep the flow from separating from the venturi surface, thereby minimizing any additional turbulence in the flowtube. Tests conducted using water droplets from the nebulizer and the HeNe laser demonstrated the aerosol and gas flow through the charger with the venturis in place was smooth and laminar.

With the venturis in place, 3 μm latex spheres were seeded into the nebulizer and allowed to flow down the flow tube at 7.5 cm/sec. The speed of the spheres through the charger plates was measured to be 30 cm/sec. With the corona charger completely shut off, 30 spheres (±5) were observed to enter the trap in the span of two minutes. When the corona charger was turned on using a minimum discharge voltage, 9 spheres were observed to enter the trap in a two-minute time interval. The conclusion was that the charging mechanism was still removing a large proportion of aerosols in the flowtube. Similar results were observed when the flow rate between the charger plates was boosted to 51 cm/sec. Using spheres of larger sizes did not affect the outcome of similar runs.

At this point the charger was disassembled and the AC charger plates were examined under a microscope. The remains of thousands of latex spheres of various sizes were observed on the plates with a microscope. To insure that this was not a problem with dry deposition, the plates were cleaned with distilled water and methanol. A re-examination showed that no spheres remained on the plates. The charger was then reassembled. Latex spheres 8 μm in diameter were seeded into the nebulizer and allowed to travel down the flowtube when just an AC voltage was put on the charger plates. After running in this mode for 1 hour, the charger was disassembled and examined under a microscope. The number of spheres that had impacted the plates was negligible. This experiment was conducted again, but this time with both the corona discharge operating and an AC voltage put on the charger plates. Examination of the charger plates after this experiment showed that hundreds of latex spheres had impacted both left and right charger plates just below the first corona charging cavities.

In order to observe the aerosol trajectories in the charger, an observation port was machined into the charger section. A one-inch quartz window placed in the port and allowed an unobstructed view of the region between the charger plates. To illuminate latex spheres between the plates, the quadrupole trap was removed from the trap section of the flowtube and replaced with a diagonal prism which redirected the HeNe and Nd:YAG laser light vertically up the flowtube and between the charger plates. A TV camera placed at the observation port window allowed the trajectories of the latex spheres to be recorded onto a VCR tape for further analysis.

With this setup in place, latex spheres were seeded into the nebulizer. The corona charger was turned on with the AC voltages set to 0 volts. The trajectories of the spheres were observed to scatter abruptly and violently out of the center of the flowtube and impact the charger plates below the first corona wire. Turning the AC voltage on at this point only exacerbated the scattering problem. The magnitude of scattering of the aerosols through the charger was observed to be independent of their radius and velocity through the charger. The

only parameter that seemed to improve the latex sphere throughput was setting the magnitude of the DC corona discharge to the minimum voltage necessary to maintain a discharge. Even with this minimal corona setting, the scattering of the spheres out of the center of the flowtube was easily observable. This corona setting, while improving the aerosol throughput, did not charge the spheres enough to be stopped in the quadrupole trap. The positive side of these experiments was the corona charger was indeed charging latex spheres to a very high Q value, but control of the spheres, once charged was proving to be a problem. It was decided to examine the nature and trajectory of charged latex spheres in an AC electric field using a Euler-Cromer model.

4.6 A Model of Aerosol Motion in the Corona Charger

Observations of latex spheres between the AC charging plates illustrated a lack of control over the particle trajectories in the charger. Two fundamental parameters used to control the particle trajectories are the AC voltage amplitude and the AC voltage frequency. An estimate of how these parameters controlled the sphere trajectory were made with a model of charged particle motion in the charger electrode configuration. It was thought that the model would yield optimal settings for the AC voltage magnitude and frequency in order to control the particle trajectory through the charger.

A charged aerosol subjected to an electric field has two distinct forces acting upon it: the electric force, which is proportional the particle charge and the electric field strength, and a friction force which is proportional to the particle surface area and velocity through the carrying medium. The equation for the motion of the particle can be described with

$$m\frac{d^2x(t)}{dt^2} = q_{sat}E(t) + \frac{\pi\rho_{gas}C_d\chi}{8C_c}r\frac{dx(t)}{dt} \qquad \text{Equation 4.3}$$

The term on the left is the net force (hence acceleration) on the charged aerosol, the first term on the right describes the driving force on the aerosol with an electric field. The second term on the

right is the drag force felt by the particle due to friction with the air. The individual variables of this equation are listed below.

m	particle mass
x(t)	particle position as a function of time
q_{sat}	saturation charge on sphere (see equation 4.1)
E(t)	electric field vector as a function of time
ρ_{gas}	gas density
C_d	particle drag coefficient (a function of the particle Reynolds number)
C_c	Cunningham slip factor (a function of the particle Knudsen number)
r	particle radius

The differential equation expressed in equation 4.3 can be solved numerically using a fourth order Runge-Kutta technique or an Euler-Cromer technique to predict the resultant particle motion, x(t), as a function of time. The model was written so that it could be used by the MATLAB software package. The code for the model is included in appendix A2.

In simulating the particle trajectory, the time step for the model was set such that each period of the electric field, E(t) (determined by the AC frequency) was divided into 500 parts. The assumption was made that each particle was charged to its q_{sat} value shortly after entering the charger. This assumption was based on observed particle trajectories in the charger as well as observed deposition of latex spheres to the AC charger plates. The model was run for several different scenarios of latex sphere size, AC charger frequency and electric field magnitudes. The results for latex spheres in several of these configurations are shown in figure 4.6 and figure 4.7 below.

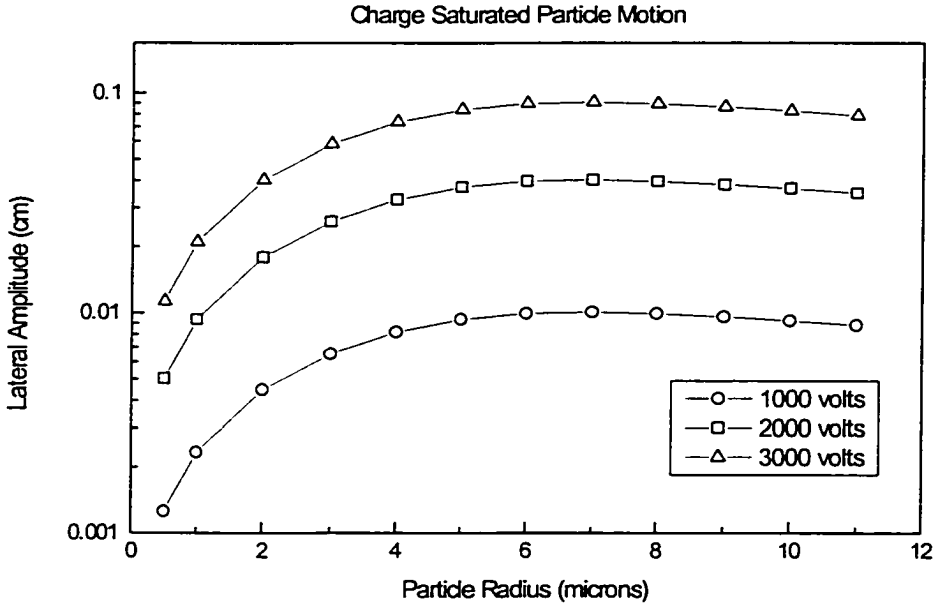

Figure 4.6 Lateral amplitude of a charge "saturated" particle as a function of applied AC voltage and particle radius at a frequency of 2000 Hz.

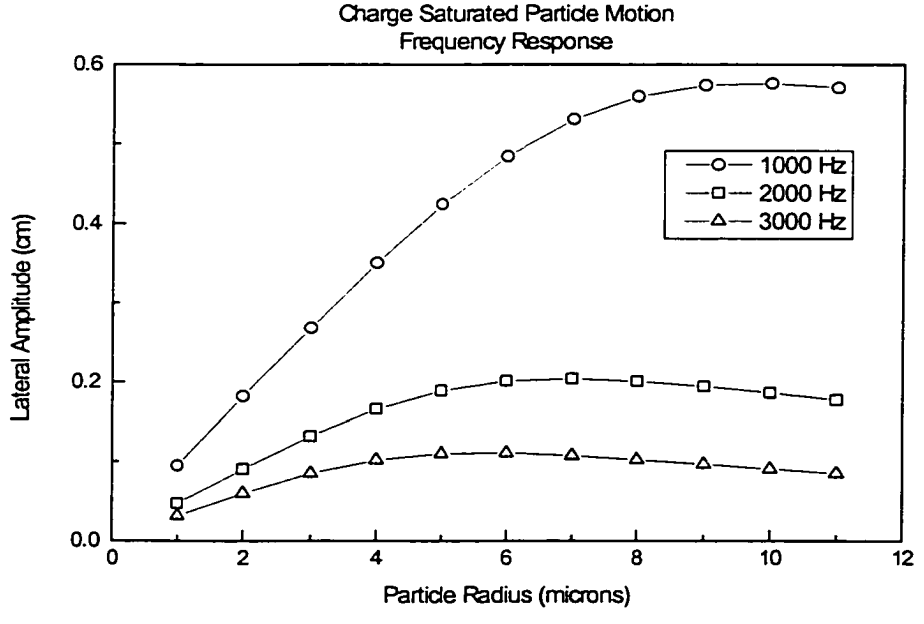

Figure 4.7 Results of a Euler-Cromer numerical solution to the trajectory differential equation. Results show the lateral amplitude of a charge "saturated" particle as a function of applied AC voltage frequency and particle radius using an applied AC voltage of 15,000 volts (the upper limit on the charger power supply).

The results of the simulation were not surprising. When the electric field generated by the AC charger plates is increased, the saturation charge of the aerosol is increased thereby increasing the amplitude of lateral oscillation. The largest lateral amplitude of latex spheres of all radii used in charger experiments possible is well below the space separating the charging plates. The conclusion is a magnitude of voltage on the AC charging plates between 2 kV and 6kV will charge the latex spheres sufficiently to allow them to be captured in the quadrupole trap while maintaining a charger throughput above 90%. Examination of the frequency response was another matter. Changes in the frequency of voltage applied to the AC charging plates from 3000 Hz to 1000 leads to changes in lateral motion amplitudes from 0.1 cm to 0.6 cm. The largest lateral amplitude of 0.6 cm (for 10 μm spheres at 1000 Hz and 15 kV) represents a significant fraction of the space between the charger plates. Even with this large amplitude, the particle throughput was estimated to be close to 60%.

It was obvious from the results of the simulation that the charger frequency was more important than either the particle radius or the magnitude of the charger voltage in controlling the sphere trajectory. Based on these findings, the charger frequency was set to 3000 Hz for the duration of the charger experiments. 3000 Hz represents the maximum frequency the step up transformers in the power supply could handle. When charging and trapping experiments were resumed, the smallest size latex sphere that could be trapped was still only 23μm in diameter. These larger particles had enough inertia to overcome some of the electrical forces diverting their smaller, less massive counterparts. Considering that some interesting heterogeneous atmospheric chemistry occurs in aerosols with submicron radii, it was thought the performance of the charger was not adequate enough to use as part of an aircraft or field instrument. As a result, further tests were designed and conducted to help optimize the corona charger operating parameters.

4.7 Current Measurements and Magnetic Field Estimates in the Corona Charger

A technique for measuring extremely small currents of ions between the charger plates (down to 50 nanoamps) was developed to elucidate the behavior of the corona charger. The technique is centered on using a highly sensitive Keithly electrometer coupled to a needle placed between the charger plates. When the corona current is turned on, molecular ions are deposited to the needle and measured by the electrometer. A measure of this charge as a function of time allows an estimate of the corona current as a function of several different experimental parameters to be made. The initial diffusion current measurement was made by disconnecting the left side corona wires from the power supply. The AC voltage plates were left in the off position when the ion collection needed was placed between the plates. The accumulated charge on the needle was then measured as function of time and the resultant ion diffusion current was calculated. The results are shown in figure 4.9 below and are similar to the results obtained by Hutchins and Holm (1989).

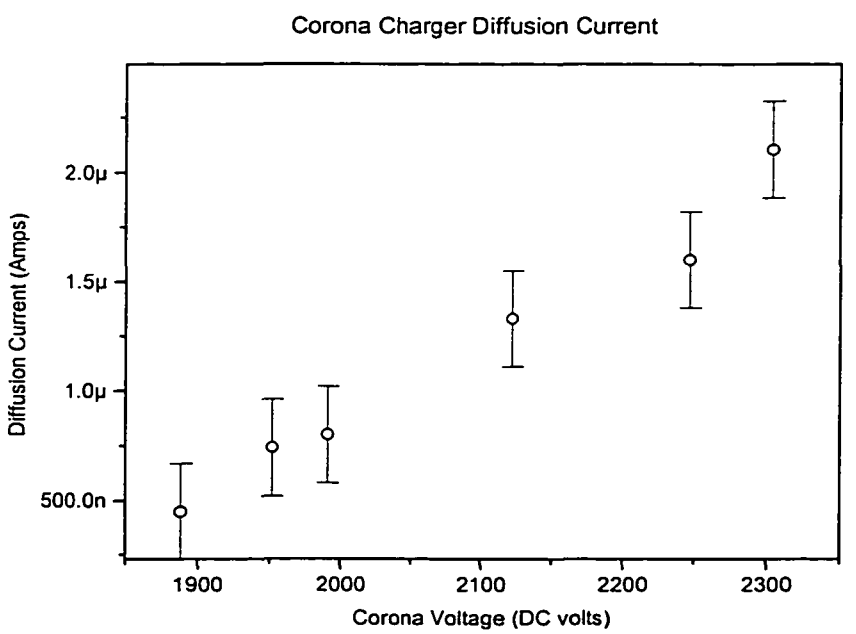

Figure 4.8 Measurements of the cross-channel diffusion current produced by the corona charger as a function of voltage applied to the corona wires.

When one of the AC charger plates was biased with 1000 volts DC, (the one with the corona wires disconnected), the number of ions impacting the collection needle increased substantially. The calculated current for this configuration was estimated to be 750 μA, nearly three orders of magnitude higher than the diffusion current alone. While the current measurements may be small compared to a household toaster, the rapid oscillation of the current caused by the high frequency on the AC charger plates leads to several effects which would potentially interfere with the trajectory of charged particles through region: (1) magnetic fields and (2) induced electromotive forces (Emf).

A basic calculation of the force needed to alter the trajectory on a charge-saturated aerosol 10 μm in diameter, with a flow velocity of 10 cm/sec (comparable to 1/10 that of electric force from AC charger plates) would require a magnetic field of 265 Tesla. An upper limit of the magnitude of the magnetic field in the charger was estimated to be 1.5×10^{-5} Tesla. This estimate was based on the results of classical electrodynamics (Jackson, 1979) and a measured corona current of 750 microamps through the corona charger. It would seem reasonable then to conclude that magnetic fields in the charger region are not substantial enough to alter the trajectory of charged particles through the region.

While the magnetic field created by the corona current may not alter the trajectory of a charged particle, it was thought that an induced electromotive force might. A circuit carrying a time varying current will induce a magnetic field, which will in turn cause an induced Emf. The largest estimate of an induced Emf in the corona charger was calculated to be ½ volt, indicating that an induced Emf in the charging region was not responsible for removing most of the charged aerosols.

4.8. Experiments with a Second (Radioactive) Charger

It was apparent from numerous lab tests that another method of charging aerosols had to be developed. A major conclusion from tests of the corona charger was the aerosols passing through the charging region were being charged to a high degree, but that only few of the largest aerosols were being stopped in the trap. Experiments conducted with the single particle injector demonstrated that the quadrupole trap was capable of slowing and trapping charged aerosols that had very large velocities and momentum. A logical conclusion was that something in the charging mechanism was responsible for completely removing or scattering charged aerosols out of the center of the flowtube, away from the quadrupole trap aperture. It was decided, therefore, to pursue another avenue of aerosol charging.

Instead of using a geometrically and electrically complicated corona discharge, a more likely method of creating large numbers of ion pairs seemed to be utilization of small amounts of a radioactive isotope. Once created, the ion pairs would then be separated by a moderate electric field to produce a unipolar ion region. As with the corona charger, small aerosols would then be passed through this region to be charged, for the most part by diffusion. The diffusion charging mechanism would not charge the aerosols to as high a degree but the momentum of the small aerosol would be substantially lower as well. Initial estimates of momentum and charge (electrical mobility) placed on a 1 μm latex sphere indicated that the quadrupole trap was capable of stopping and confining such aerosols.

Using a radioactive source to produce ions had several benefits. The first of these benefits was the charger would not produce the copious amounts of ozone that the corona discharge did. Eliminating the corona charger also removed the need for a complicated power supply. The initial design of a radioactive charging mechanism also eliminated the need for complicated electrode geometry. Instead of the complicated geometry of the corona discharge, the radioactive could be easily constructed from two concentric cylinders. The turbulence created

by two cylinders within the flowtube would also be greatly reduced, thereby increasing the changes of a charged aerosol successfully entering the trap aperture.

When aerosols are exposed to unipolar ions, they become charged due to collisions between the ions and the aerosol surface. In the absence of an applied electric field, particle charging is primarily due to collisions caused by Brownian motion of the ions, and is referred to as diffusion charging. When aerosols are charged under moderate electric field intensities, both field and diffusion mechanisms of particle charging should be considered (Yeh, 1993). An estimate of the charge deposited on an aerosol is given by the following equation developed by Cochet (1961)

$$n = \left(1 + \frac{K_{ni}}{2}\right)^2 + \frac{2}{1 + K_{ni}}\left(\frac{\varepsilon - 1}{\varepsilon + 1}\right)\left(\frac{Ed_p^2}{4e}\right)\left(\frac{\pi N_i e Z_i t}{\pi N_i e Z_i t + 1}\right) \qquad \text{Equation 4.4}$$

where

N_i is the ion concentration (ions / cm3)

t is the charging time (sec)

e is the elementary unit of charge (4.8×10^{-10} statC)

E is the applied electric field strength (statV / cm)

Z_i is the mobility of the ions (~ 450 cm2 / statV s)

ε is the dielectric constant of the aerosol

d_p is the particle radius (cm)

Kn_i is the aerosol Knudsen number

Estimates of charge deposited under conditions of a 500-volt field and a ten second residence time in the charging region indicate that the quadrupole trap would be capable of stopping and confining aqueous aerosols with diameters close to 3 μm. The only drawback to

such a design was the selection and procurement of a radioactive source. Two candidates were the alpha particle emitters Americium and Polonium.

A nuclear radioactive decay process is characterized by a nucleus that emits a proton, alpha particle, electron or photon to rid itself of excess energy. Heavy nuclei are usually energetically unstable against the spontaneous emission of alpha particles.

The alpha decay process is usually described with the following notation ${}^{A}_{Z}X \rightarrow {}^{A-4}_{Z-2}Y + {}^{4}_{2}\alpha$ where X is the parent nucleus, Y the daughter and α is the alpha particle. The result of alpha emission is to drop the atomic number of the nucleus down by four and the charge by two. Radioactive alpha sources usually emit particles that are generally limited to the energy range $\approx$ 4-7 MeV. The alpha decay process was first described by Gamow and Condon and by Gurney as the quantum mechanical tunneling of the alpha particle through the potential barrier of the nucleus. The half-life of the alpha particle source is inversely related to the energy of the emitted alpha particle. If the particle energy is large, the half-life will be short. If the emitted particle is low in energy, the half-life will be long, due to the small probability that the alpha particle will tunnel through the potential barrier.

In terms of other charged particles, alpha particles are considered very heavy. When passing through matter, alpha particles bump their way through atomic electrons of the medium via the coulomb field, resulting in ionization of the medium. As a result of the ionization, the alpha particle gradually loses its energy. As an alpha particle passes through a gas, positive ions and electrons are formed in equal numbers by way of inelastic collisions along its path. If the ions are formed in a gas-filled space between two electrodes with some potential difference between them, the negative ions will be attracted to the positive electrode and the positive ions will be attracted to the negative electrode. This is the fundamental concept behind the ionization chamber (Litton and Hertzberg, 1977). This idea can be used to electrically charge aerosols for use with the flytrap instrument.

The alpha source initially chosen for use in investigations of a radioactive charging mechanism was ^{241}Am. Americium is a byproduct of the artificial production of Neptunium 237. ^{241}Am is widely used as an alpha source due to its relative abundance and its nearly mono-energetic (and low energy) alpha particles and its long half-life. The isotope ^{241}Am has half life of 433 years and emits alpha particles of 5.486MeV

For a gaseous medium such as air, the accepted average ionization potential is 32.5 eV. The number of ions that are theoretically possible then is easily calculable. With energies of 5.4 MeV, alpha particles from ^{241}Am are expected to produce approximately $1.6*10^5$ ion pairs per disintegration. With a 200 microcurie source, the ion generation rate should then be $(1.6*10^5 ipd)*(7.4*10^6 dps) = 1.2*10^{12}$ ion pairs per second.

To calculate where most of these ions will be formed, the range of alpha particles through air at standard pressure and temperature needed to be estimated. The range of a 5.4 MeV alpha particle through air at standard pressure and temperature cannot be calculated from the Bethe-Bloch equation. The assumptions made in the derivation of this relationship are not valid for low energy alpha particles. The behavior of alpha particles at this energy range comes entirely from empirical data.

Estimates of alpha particle range at standard temperature and pressure indicated that most of the ion production would not occur within the geometry limitations of the flowtube. Therefore a thin coating of gold (Au) would be necessary around the ^{241}Am alpha source for two reasons. The thin gold coating prevents the decay product (Np), from being kicked out into the charging chamber and most importantly, the gold absorbs some of the alpha energy so that the maximum amount of ionization (specific ionization) occurs within the charging chamber, and not inside the electrode walls.

The data shown below [Williamson, 1966] illustrates the range of alpha particles in a gold medium. Based on the data from figures, estimates were that a 5.7 micron gold coating was

needed on the Americium source to reduce the energy of the alphas from 5.48 MeV to a nominal 2.713 MeV. With energies of 2.714 MeV, alpha particles will travel through approximately 1.5 cm of air at standard pressure and temperature. This distance will be much greater at reduced pressures, thereby increased altitudes of charger operation.

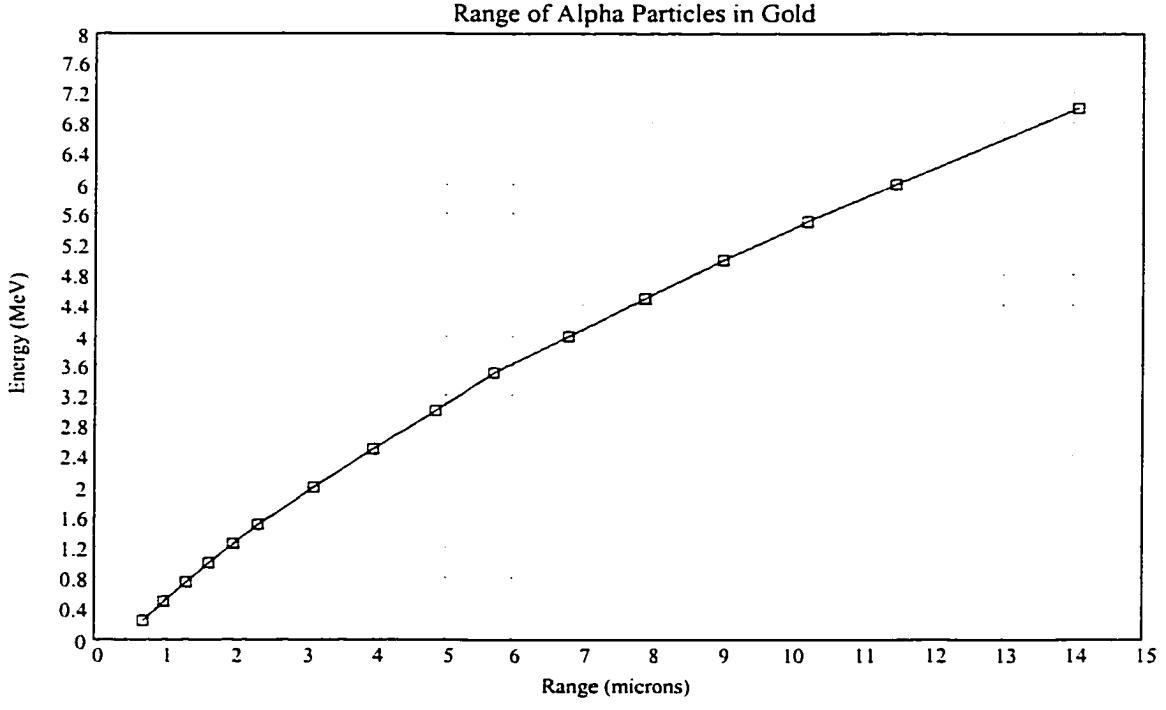

Figure 4.9 Range of Alpha particle through solid gold. Range-Energy values for Alpha Particles in a gold absorber : Data from CF Williamson, JP Boujot, H Picard : Tables of Range and Stopping Power of Chemical Elements for Charged Particles of Energy 0.5 to 500 MeV, CEQ-R_3042 (1966). Available from Clearinghouse for Federal Scientific and Technical Information, Springfield Virginia.

Several problems arose with trying to procure a 200-microcurie Americium source for the flytrap experiment. The first of these problems was cost. Isotope Products Laboratories (Burbank CA) quoted a price in excess of ten thousand dollars for a 200-microcurie custom-manufactured Americium source. Placing a 5 – 6 μm gold coating over the source via vapor deposition would add to this cost substantially. The second problem involved the University of New Hampshire Office of Environmental Health and Safety: They would not issue a radiation permit for the flytrap lab. Several alternatives were investigated including disassembling several

dozen smoke detectors to obtain the needed Americium from them. The other alternative was to remove the strips containing Polonium from several dozen commercially available anti-static brushes.

Using Polonium as a source of ions instead of Americium posed no experimental difficulty. The isotope used for this study was Polonium 210, with a half-life of 138 days. The energy of alpha particles emitted by ^{210}Po is a nominal 4.5 and 5.3 MeV. The twenty four polonium strips used in this experiment were removed from anti-static brushes obtained from McMaster-Carr. Each strip was characterized for activity with a small Geiger counter. The individual strips were found to have an average initial activity of 500 ± 50 microcuries.

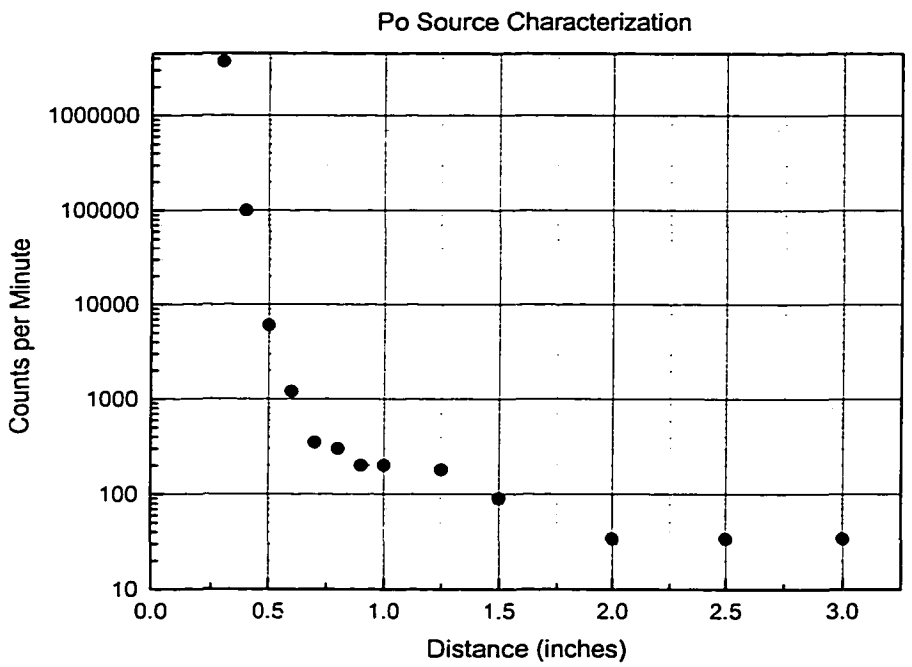

Figure 4.10 Data from the characterization of a single Polonium source. Plot was used to determine the placement of the sources in order to maximize charging volume, minimize deposition and to send aerosols on a trajectory towards the center of the flowtube assembly.

Several individual PSL spheres were injected into the trap tribologically. When a Polonium strip was brought close to the trap aperture, the charge on the sphere was quickly

neutralized. The conclusion of this test is the polonium was active enough to produce copious amounts of ion pairs. The polonium strips were then fastened with epoxy to the interior of a brass cylinder ten inches long with a radius of two inches. A solid brass rod was then inserted into the first cylinder creating a region in which to create unipolar ions. Both electrodes were suspended in a flytrap flowtube section with the use of lexan spiders.

When the ion pairs formed in a gas-filled space between two electrodes with small potential difference between them, the negative ions were attracted to the positive electrode and the positive ions attracted to the negative electrode. This is the fundamental concept behind the ionization chamber (Litton and Hertzberg, 1977). This idea was used to electrically charge aerosols for use in the flytrap instrument. The net effect of the radioactive ionization chamber was to create a region of space filled with unipolar ions, through which aerosols move to become charged. Figure 4.11 below illustrates the essential geometry of the charger. Each electrode is connected to ground or a power supply via SHV feedthroughs.

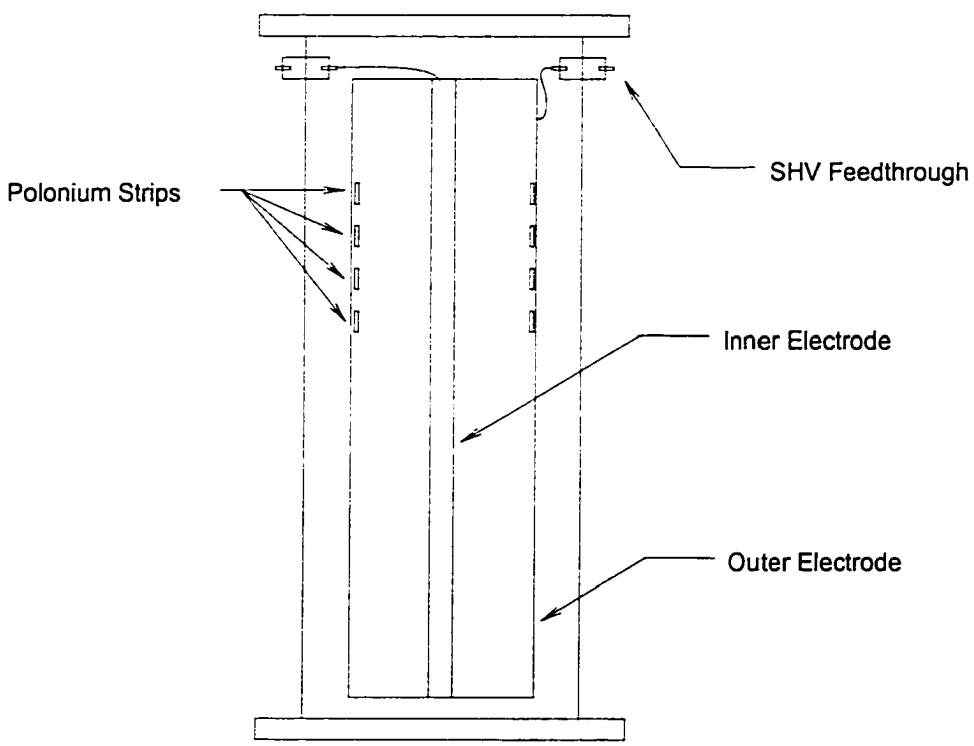

Figure 4.11 A drawing of the "radioactive charger" illustrating relevant geometry and placement of the Polonium sources.

The outer cylinder was connected to either a DC power supply capable of producing 0 ± 1000V or an AC voltage capable of producing 0 – 10,000 volts (borrowed from the corona charger power supply). The inner cylinder was electrically grounded. The DC voltage on the outer cylinder, depending on the sign of the voltage created a volume filled with positive or negative ions. Aerosols traveling through this region could be charged via diffusion charging or a combination of field / diffusion charging depending on the magnitude of the voltage in the region between the electrodes.

The electric field and the voltage between the electrodes was calculated with appropriate boundary conditions and Laplace's equation. The potential in the charging region (between the electrodes) was easily calculated from Laplace's equation, $\nabla^2\Psi = 0$, where ψ is the potential in cylindrical coordinates. Once the radial potential is determined, the electric field strength in the charging region was estimated as a function of distance from the source electrode. The electric field magnitude for 500 V and 1000 V placed on the outer electrode is shown in figure 4.12

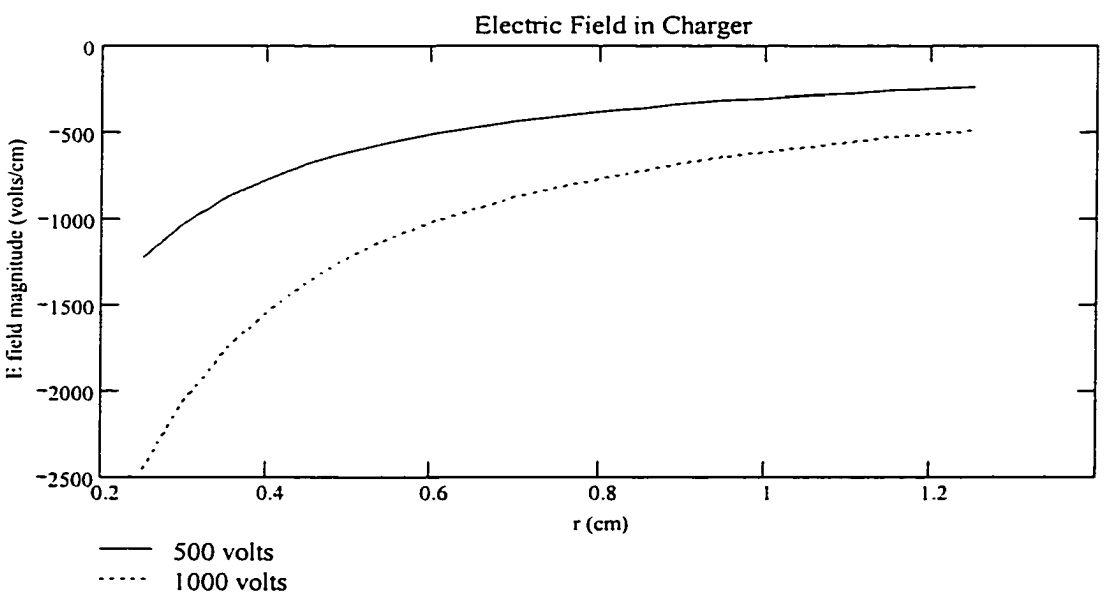

Figure 4.12 Estimated electric field in the radioactive charger. Outer electrode is held at a negative voltage while the inner electrode is grounded.

When the outer electrode is held at a negative voltage and the inner electrode is grounded the result is an electric field that is logarithmic in nature. The field strength is strong at the outer electrode and zero at the inner electrode, with a direction that points radially inward. The field will pull negative ions towards outer cylinder and push positive ions into the charging region. Aerosols traveling through this region will be charged with a magnitude described by equation 4.4. The resultant charged aerosols would be subject to an electric force that pushes them towards the center of the flowtube assembly where they have a greater chance of entering the trap aperture.

Once assembled and tested the charger was inserted into the laboratory flowtube assembly, in a manner similar to that illustrated in figure 4.6. The operating parameters of the flowtube as well as the charger power supply were varied in order optimize the performance of the charger system. The first test to take place was designed to see if the charger could be used in a strict "diffusion" charging method. PSL spheres 3 μm in diameter were seeded into the reservoir and the outer electrode was held at a small voltage (-100V). The probe of the Keithly electrometer was briefly inserted into the charging region between the electrodes to ensure the region was filled with charged ions of the correct sign. Flow rates through the system were varied to give the aerosols a residence time between one and ten seconds. While these parameters were varied, the AC voltage on the trap was kept at a voltage of 700 volts. Three hours of operation in these modes fail to trap a single aerosol. Visual observations of trajectories through the trap indicated that the aerosols were not charged to any degree.

The next set of experiments with the radioactive charger involved applying positive DC voltages of 500V and 1000 V to the outer electrode, while keeping the inner electrode grounded. Again, PSL spheres 3 μm in diameter were seeded into the reservoir. The probe of the Keithly electrometer was briefly inserted into the charging region. The number density of negative ions in the charging region was significantly higher than when 100 volts were placed on the outer

electrode. Flow rates through the system were again varied to give the aerosols a residence time between one and ten seconds. While these parameters were varied, the AC voltage on the trap was kept at a voltage of 700 volts. Several hours of operation in these modes fail to trap a single aerosol. Visual observations of trajectories through the trap indicated that the aerosols were only mildly charged, but not enough to trap. Similar results were obtained when the DC voltages on the outer electrode were changed from positive to negative.

As with the corona charger, this ionization chamber method of placing charge on aerosols was less than successful. It was suspected that if the electric field in the charging region was increased, more charge would be applied to the aerosols, but the force on the aerosol by the electric field would also be larger, resulting in deposition to the grounded electrode in the center of the charger. Suitable operating parameters could not be established for this charging system that would deposit enough charge on an aerosol in the 1 – 5 μm size range in order for it to be trapped. It was thought however, that the charger section could be modified by removing the Polonium and using the section as a "focus electrode" in conjunction with the corona charger. Only preliminary investigations of this idea were carried out however.

4.9. Future experiments

Given the somewhat successful, but not practical results of optimizing the corona charger for use as an element of a field version of the flytrap, it would be prudent to pursue several experiments in the future. It was demonstrated that the 500-microcurie Polonium sources were capable of generating copious amounts of ion pairs in a finite region of space. It may be feasible to use the geometry of the corona charger in conjunction with the Polonium sources as ion generators instead of a discharge. The simplification in the source of ions used in the charger would mean several variables less in parameter space that needed to be optimized in order to make the charger a practicable and reliable device.

In addition to replacing the ion source, it may prove to be fruitful to use the concentric cylinder geometry developed for the radioactive charger as a way to gently but firmly electrically focus charged aerosols back toward the center of the flowtube. Several preliminary investigations were carried out in the efforts to build a "focus electrode" for the flytrap.

The MATLAB software written to model the trajectory of a charged aerosol between the two AC charging plates was modified to estimate the trajectory of a 10-μm latex sphere through a focus electrode. Instead of using an AC potential, a strictly DC potential was used in equation 4.3. The equation was then solved using a Euler-Cromer method. The model results for several voltages on the outer electrode are shown in figure 4.13 below.

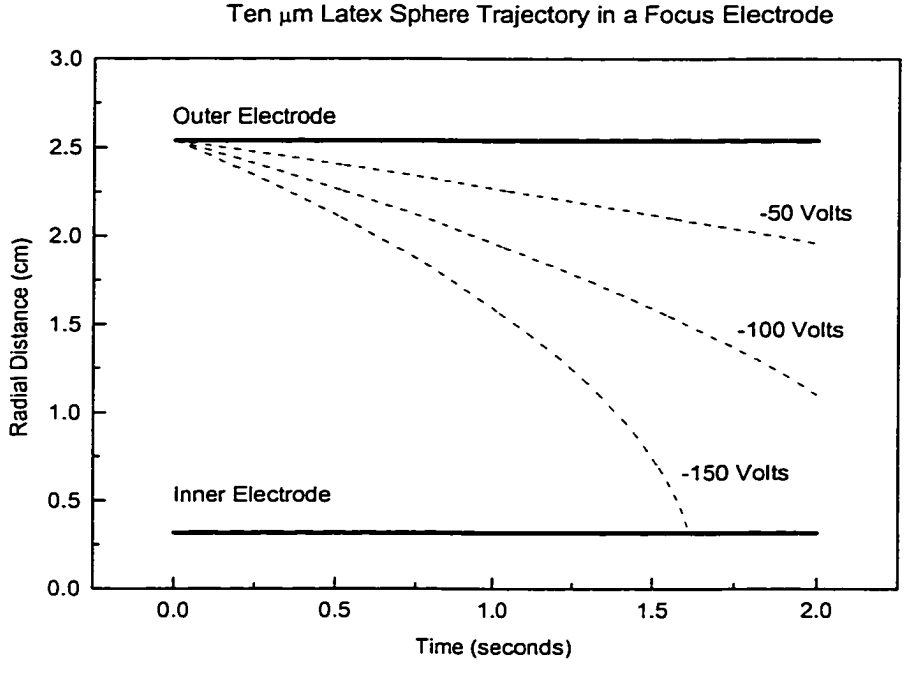

Figure 4.13 Model results for the focus electrode. The inner electrode radius was set to 0.25 cm and the outer electrode radius at 2.5 cm. The plot shows radial distance as a function of time in the focus electrode where drag and electrical forces were the only ones considered. Three different runs at different voltages were made, each with a 10 μm latex sphere with a qsat charge applied.

An analysis of the model results indicate that only a very small voltage (less than 200

volts) is needed to cause the charged latex sphere to impact the inner electrode. The voltage needed to cause this deposition is smaller for aerosols with a higher electrical mobility. These results also indicate why the electrode geometry for the radioactive charger failed to produce aerosols capable of being stopped in the quadrupole trap: The electric fields necessary to cause the ion pairs to separate were large enough to cause deposition to the electrode walls. Using the Polonium "modified" AC charger with a large electric field between the plates (9000 V/cm) in conjunction with the focus electrode may prove to be what is needed to successfully charge and trap aerosols in the 1 – 10 μm size range.

Several tools are available for optimization of the focus electrode. The first of these is the single particle injector described in chapter 1. The microparticle injector is capable of producing a fine, well-directed stream of charge aerosols. The sizes and charges on the aerosols being ejected from this generator can then be directed through the focus electrode. Visual observations of the exit location can be optimized by controlling the voltages on the electrode with the use of the microscope / TV camera assembly in addition to a laser to illuminate the exiting aerosols.

Charges on aerosols exiting both the corona charger and the focus electrode need to be quantified if the flytrap charger is to be made practical and efficient. To this end, another diagnostic tool was constructed to measure charges on small droplets. The device relies on the principle of electrical induction. A charged droplet falling through a small metal cylinder (1" diameter) will momentarily change the electrical potential of the cylinder. A positive charge will raise the potential while a negative on will lower it. The size of the potential change reveals the magnitude of the charge on the droplet according to

$$q = K \times V_{max} \frac{1}{\sqrt{1+\left(\frac{D}{L}\right)^2}} \times 10^{-12}\, coulomb \qquad \text{Equation 4.5}$$

where q is the charge on the droplet, K is an amplifier constant, D is the diameter of the inner cylinder, L is the length of the inner cylinder and V_{max} is the maximum voltage recorded during the particles path through the instrument. The induction apparatus is then placed under a stream of individual charged particles from the particle injector or corona charger and the voltages measured with the following circuit:

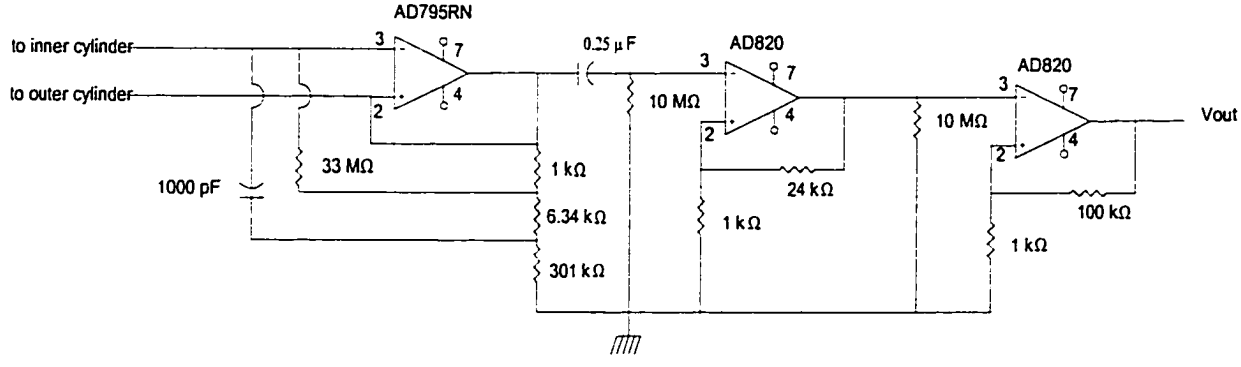

Figure 3.14 A pulse amplifier circuit to emit a voltage pulse when a charged droplet passes through the inner cylinder. The outer cylinder is merely there for electrical shielding.

The output of this pulse amplifier circuit can be read with either a hand held voltmeter or an oscilloscope. This device was constructed and only briefly utilized to ensure that charged droplets were being emitted from the microparticle injector. The validity of equation 4.5 was not tested or verified to any degree of calibration. By using this device without the quadrupole trap to rely on the presence and magnitude of charged aerosols, it may be possible to find a set of suitable operating parameters for a charging mechanism, corona, barrier discharge, radioactive or other type.

It was found that charging micron-sized aerosols to a degree such that they would be caught in the quadrupole trap was an extremely difficult task. Only partial success was achieved trapping latex spheres 13 µm in diameter using the corona discharge as an ion source. It is quite possible that future work done with the corona charger in conjunction with a focus electrode will

produce positive results. If an adequate charging and trapping mechanism can be developed, there is a very good possibility that the flytrap instrument could be used as a field instrument.

CHAPTER 5

SUMMARY

The Flytrap instrument was conceived and developed to meet the demand for simultaneous, in situ, single aerosol physical and chemical analysis. The development of this instrument was motivated by the need to measure aerosols parameters in ambient atmospheric conditions with minimal perturbations to the aerosol physical and chemical characteristics. A tremendous amount of work went into developing, testing and calibrating the Flytrap systems and ancillary controls. Flytrap has been shown to be an extremely versatile instrument, capable of analyzing individually levitated aerosols in an environment where the ambient conditions can be well controlled. Calibration experiments have shown that the suspended aerosols can be maintained in a variety of conditions and studied for time intervals spanning several days.

In addition to development of the Flytrap analysis instrumentation, a substantial portion of this project was directed at developing a suitable aerosol charging apparatus. In order to use Flytrap as a field instrument, the aerosols sampled require a large electric charge in order to be captured by the quadrupole trap. It was found that charging micron-sized aerosols to a degree such that they would be caught in the quadrupole trap was an extremely difficult task. Aerosol charging still remains a daunting and unresolved issue. To this end, it is possible that future work done with the corona charger in conjunction with a focus electrode will produce positive results. If an adequate charging and trapping mechanism can be developed, there is a good possibility that the Flytrap instrument could be used in the field.

Because the Flytrap instrument acts as a wall-less container, it proved to be an ideal lab based platform for obtaining information on chemical and physical characteristics of artificial

sea-salt aerosols. Several sets of heterogeneous chemical interactions were studied using Flytrap. The first set of experiments dealt with the nature of HNO_3 interactions with artificially produced sea-salt aerosols in a variety of conditions. The second set of experiments dealt with looking at the oxidation of SO_2 within artificial sea-salt aerosols when they were exposed to O_3 as well as H_2O_2.

The flytrap instrument proved to be a useful device to explore the nature of coarse mode nitrate formation in sea-salt aerosols. Uptake rates of nitric acid for aerosols of various sizes, nitric acid vapor mixing ratios and alkalinity condition as a function of time were examined. Two separate relative humidity values (0% and 90%) were used in the measurements of uptake rates. It was also demonstrated that $NaNO_3$ in sea-salt aerosols is a permanent removal pathway for nitrate in the atmosphere. The effect of bicarbonate alkalinity on the reactive uptake rates of nitric acid in sea-salt aerosols was also observed. The uptake rates of alkaline spiked sea-salt aerosols were found to be an order of magnitude higher than aerosols without alkalinity.

Several implications can be drawn from these laboratory measurements. One of which relates to whether HNO_3 removal by NaCl aerosols could be significant enough to reduce the HNO_3 / NO_x ratios when included in the global chemistry models. This laboratory study showed that the reaction of HNO_3 with NaCl is not limited to the surface of the aerosol but can react with the bulk of the aerosol in the presence of H_2O vapor. Because the relative humidity of the marine boundary layer is often near 90%, it is possible that the reaction between nitric acid vapor and sea-salt aerosols will provide a large sink for HNO_3, as indicated by the modeling studies of Tabazadeh et al. [1998].

During the course of these experiments, it was demonstrated that sulfate, once present in NaCl aerosols was permanent. No changes in trace gas mixing ratios or changes in relative humidity could cause volatilization of Na_2SO_4. The implication is that oxidation of dissolved SO_2 by any mechanism in sea-salt aerosol represents a permanent removal pathway of sulfur from the atmosphere. No sulfate production was observed when aqueous NaCl aerosols were subject to high mixing ratios sulfur dioxide and ozone. The S(IV)-O_3 reaction was observed to proceed extremely rapidly when carbonate alkalinity was introduced to the aerosols under study. Time dependent measurements of this reaction were made and it was found that the reaction proceeded until the aerosol was depleted of alkalinity. The observed S(IV)-H_2O_2 reaction rates were very rapid with respect to the S(IV)-O_3 rates.

The natural buffering capacity of sea-salt aerosols indicates that the aerosols are capable of sustaining large amounts of sulfate production through the oxidation of sulfate by ozone or hydrogen peroxide. The buffered sea-salt aerosols possess a high pH allowing the reaction to proceed at a substantial rate. The progress of this reaction is apparently limited by the availability of the carbonate buffer, which once overwhelmed, allows the aerosol pH to fall and consequently the rate of sulfate production to slow. The calculations of Chamedies and Stelson (1992) indicate that the rate of removal of SO_2 by sea-salt is quite significant and is roughly equal to the rate of DMS emission from the ocean. In the Flytrap experiments, the S(IV) – O_3 reaction was seen to occur only for high values of aerosol pH. If the sea-salt aerosols are depleted of alkalinity due to interactions with nitric acid (or any other acidic trace gas for that matter) in a polluted air mass, the potential exist to shut down the S(IV) – O_3 reaction in favor of the S(IV) – H_2O_2 reaction.

As with any set of investigations this exploratory in nature, the results presented here lead to entire series of experiments to be conducted in the future. Further experiments remain to be conducted on a suitable charging/trapping mechanism to enable Flytrap to be used as a field instrument. Many laboratory experiments remain to be done as well, including using the Raman system to determine HNO_3 concentrations in aqueous aerosols and not just NO_3^- concentrations.

Doing so will enable measurements of $[NO_3^-]$ / $[HNO_3]$ ratios to be measured and thereby a direct measurement of aerosol pH can be made. Many interesting heterogeneous chemistry problems exist and it has been shown that the Flytrap is a capable and reliable platform for such investigations.

REFERENCES

Andrea, M. O., and P. J. Crutzen, 1997, Atmospheric aerosols: Biogeochemical sources and role in atmospheric chemistry: Science, v. 276, p. 1052 - 1058.

Arnold, S., and L. M. Folan, 1986, Fluorescence spectrometer for a single electrodynamicaly levitated microparticle: Rev. Sci. Inst., v. 57, p. 2250.

Baker, M. B., 1997, Cloud Microphysics and Climate: Science, v. 276, p. 1072 - 1078.

Bierchert, P., B.J. Finlayson-Pitts, 1996, Knudsen Cell studies of the uptake of gaseous HNO_3 and other oxides of nitrogen on solid NaCl: The role of surface adsorbed water., J. Phys. Chem., 100, 21,218 – 15,228

Blanchard, D.C., A.H. Woodcock, 1957, Bubble formation and modification in the sea and its meteorological significance. Tellus 9, 145-158

Brimblecombe, P., S. L. Clegg, 1988, The solubility and behavior of acid gases in the marine aerosol. J. Atmos. Chem., 7, 1-18

Brock, C. A., P. Hamill, J. C. Wilson, H. H. Jonsson, and K. R. Chan, 1995, Particle formation in the upper tropical troposphere: A source of nuclei for the stratospheric aerosol: Science, v. 270, p. 1650-1653.

Butler, J.N., 1982, Carbon Dioxide Equilibria and Their Applications, Addison-Wesley Pub. Co., Reading MA.

Carleton, K. L., D. M. Sonnenfroh, S. J. Davis, and W. T. Rawlins, 1992, Quadrupole Trap for Optical Characterization of Aerosols, Andover, Physical Sciences Inc.

Carleton, K.L., W.T. Rawlins, D.M., Sonnenfroh, D.A. Palambo, M.R. Malonson, A.H. Burbo, K.R. McManus, M.F. Hinds, M.B. Loomis, R.W. Talbot, 1995, Quadrupole Trap Instrument for In Situ Characterization of Atmospheric Aerosols Final Report, NASA CR- PSI-2258/TR-1402

Carleton, K. L., D. M. Sonnenfroh, and W. T. Rawlins, 1997, Freezing behavior of single sulfuric acid aerosols suspended in a quadrupole trap: J. of Geophysical Research, v. 102, p. 6025 - 6033.

Chameides, W. L., and A. Stelson, 1992, Aqueous-phase chemical processes in deliquescent sea-salt aerosols : A mechanism that couples the atmospheric cycles of S and sea salt: J. of Geophysical Research, v. 97, p. 20,565 - 20,580.

Charlson, R. J., J. E. Lovelock, M. O. Andreae, and S. G. Warren, 1987, Oceanic phytoplankton, atmospheric sulfur, cloud albedo and climate: Nature, v. 326, p. 655 - 661.

Charlson, R. J., S. E. Schwartz, J. M. Hales, R. D. Cess, J. A. Coakley, J. E. Hansen, and D. J. Hofmann, 1992, Climate forcing by anthropogenic aerosols: Science, v. 255, p. 423 - 429.

Cofer, W. R., V. G. Collins, and R. W. Talbot, 1985, Improved aqueous scrubber for collection of soluble atmospheric trace gases: Environmental Science and Technology, v. 19, p. 557-560.

Cohen, M. D., R. C. Flagan, and J. H. Seinfeld, 1987, Studies of concentrated electrolyte solutions using the electrodynamic balance. 1. Water activities for single-electrolyte solutions: J. of Physical Chemistry, v. 91, p. 4563 - 4575.

Dawson, B. S. W., D. E. Irish, and G. E. Toogood, 1986, Vibrational spectral studies of solutions at elevated temperatures and pressures. A Raman spectral study of ammonium hydrogen sulfate solutions and the HSO4- - SO4= equilibrium: J. of Physical Chemistry, v. 90, p. 334 - 341.

Davis, E.J.,1983, Transport Phenomena with Single Aerosol Particles, Aeros. Sci. Tech. 2, 121-144

DeBock, L. A., H. VanMalderen, and R. E. VanGieken, 1994, Individual aerosol particle composition variations in air masses crossing the North Sea: Envir. Sci. Technol., v. 28, p. 1513-1520.

Dentener, F. J., G. R. Carmichael, Y. Zhang, J. Lelieveld, and P. J. Crutzen, 1996, Role of mineral aerosol as a reactive surface in the global troposphere: J. of Geophysical Research, v. 101, p. 22869 - 22889.

Duce, R. A., 1969, On the source of gaseous chlorine in the marine atmosphere: J. Geophys. Res., v. 74, p. 4597 - 4599.

Eriksson, E., 1959, The yearly circulation of chlorine and sulfur in nature: Meteorological, geochemical and pedological implications: Tellus, v. 11, p. 375 - 403.

Faust, B. C., 1994, Photochemistry of clouds, fogs, and aerosols: Environmental Science and Technology, v. 28, p. 217 - 222.

Finlayson-Pitts, B. J., and J. N. Pitts, 1986, Atmospheric Chemistry: Fundamentals and Experimental Techniques, 1098 pp., Wiley, New York

Finlayson-Pitts, B. J., and J. N. Pitts, 1997, Tropospheric air pollution: Ozone, airborne toxics, polycyclic aromatic hydrocarbons, and particles: Science, v. 276, p. 1045 - 1051.

Fitzgerald, J.W., 1991, Marine aerosols: A review. Atmospheric Environment, 25A, 533-546

Fung, K. H., and I. N. Tang, 1989, Composition analysis if suspended aerosol particles by Raman spectroscopy: Sulfates and Nitrates: J. Coll. Int. Sci., v. 130, p. 219.

Goodman, A. L., E.T. Bernard and V.H. Grassian, 2001, Spectroscopic Study of Nitric Acid and Water Adsorption on Oxide Particles Enhanced Uptake Kinetics in the Presence of Adsorbed Water: Journal of Physical Chemistry, v. 105 p 6443 – 6457.

Graedel, T. E., and W. C. Keene, 1995, Tropospheric budget of reactive chlorine: Global Biogeochemical Cycles, v. 9, p. 47 - 77.

Gunz, D.W., M.R. Hoffman, 1990, Atmospheric Chemistry of Peroxides: A Review, Atmospheric Environment, v. 24a, p. 1601-1633

Hanson, D. R., A. R. Ravishankara, and S. Solomon, 1994, Heterogeneous reactions in sulfuric acid aerosols: A framework for model calculations: J. of Geophysical Research, v. 99, p. 3615 - 3629.

Harrison, R. M., and C. A. Pio, 1983, Major ion composition and chemical associations of inorganic atmospheric aerosols: Environ. Sci. Technol., v. 17, p. 169 - 174.

Hautanen, J., and M. Kilpelainen, 1995, Electrical agglomeration of aerosol particles in an alternating electric field: Aerosol Science and Technology, v. 22, p. 181-189.

Hightower, R.L., C.B. Richardson, H.B. Lin, J.D. Eversole, A.J. Campillo, 1988, Measurements of Scattering of Light from Layered Microspheres, Opt. Lett., 13, 946

Hoffman, M.R. and Calvert, J.G, 1985, Chemical Transformation Modules for Eularian Acid Deposition Models, Volume 2, The Aqueous Phase Chemistry, EPA/600/3-85/017

Huebert, B. J., Zhuang, L., Howell, S., Noone, K., 1996, Sulfate, nitrate, methanesulfonate, chloride, ammonium and sodium measurements from ship, island and aircraft during the Atlantic Stratocumulus Transition Experiment / Marine Aerosol Gas Exchange, J. Geophys. Res., 101, 4413- 4423

Hutchins, D. K., and J. Holm, 1989, Aerosol charger using sinusoidally driven ion current from a corona discharge: Aerosol Science and Technology, v. 11, p. 244 - 253.

IPCC (1990) Climate Change. In: Intergovernmental Panel on Climate Change: Report by Working Group 1. Cambridge University Press, Cambridge

Jackson, J.D., 1979, Classical Electrodynamics, John Wiley and Sons Inc., New York

Jayne, J. T., P. Davidovits, D. R. Worsnop, M. S. Zahnisner, and C. E. Kolb, 1990, Uptake of SO_2 by aqueous surfaces as a function of pH: The effect of chemical reaction at the interface: J. Phys. Chem, v. 94, p. 6041 - 6048.

Jambers, W., De Bock, L., Van Grieken, R., 1995, *Analyst*, (Cambridge, U.K.) v 120, p. 681

Johnston, M.V., A.S. Wexler, 1995, MS of Individual Aerosol Particles: Analytical Chemistry, v 67 p. 721 – 726.

Jones, A., D. L. Roberts, and A. Slingo, 1994, A climate model study of indirect radiative forcing by anthropogenic sulfate aerosols: Nature, v. 370, p. 450 - 453.

Junge, C.E., 1956, Recent investigations in air chemistry, Tellus, 8, 127-139

Keene, W. C., A. A. P. Pszenny, J. N. Galloway, and M. E. Hawley, 1986, Sea -salt corrections and interpretation of constituent ratios in marine precipitation: J. of Geophysical Research, v. 91, p. 6647-6658.

Keene, W. C., A. P. Pszenny, D. J. Jacob, R. A. Duce, J. N. Galloway, J. J. Schultz-Tokos, H. Sievering, and J. F. Boatman, 1990, The geochemical cycling of reactive chlorine through the marine troposphere: Global Biogeochemical Cycles, v. 4, p. 407 - 430.

Keene, W.C., R Sander, A Pszenny, R. Vogt, P. Crutzen, J. Galloway, 1998, Aerosol pH in the Marine Boundary Layer, A Review and Model Evaluation., Journal of Aerosol Science, 1998

Kelly, T. J., D. H. Stedman, J. A. Ritter, and R. B. Harvey, 1980, Measurements of oxides of nitrogen and nitric acid in clean air: J. of Geophysical Research, v. 85, p. 7417 - 7425.

Kester, D.R., I.W. Duedall, D.N. Connors, R.M. Pytkowicz, 1967, Preparation of artificial seawater, Limnol. Oceanog., 12, 176-179

Klemm, O., and R. W. Talbot, 1991, A sensitive method for measuring atmospheric concentrations of sulfur dioxide: J. of Atmospheric Chemistry, v. 13, p. 325 - 342.

Kley, D., 1997, Tropospheric chemistry and transport: Science, v. 276, p. 1043 - 1044.

Kumar, S., 1989, The characteristic time to achieve interfacial phase equilibrium in cloud drops, Atmos. Environ, 23, 2299-2304

Lagrange, J., Pallares,C., and Lagrange, P. ,1994, Electrolyte effects on aqueous atmospheric oxidation of sulfur dioxide by ozone, J. Geophys. Res., 99, 14595-14600.

Laux, J.M, J.C. Hemminger, B.J. Finlayson-Pitts, 1994, X-ray photoelectron spectroscopic studies of the heterogeneous reaction of gaseous nitric acid with sodium chloride: Kinetics and contribution to the chemistry of the marine troposphere, Geophysical Research Letters, v 21, no 15, 1623-1626

Lee, K.W., M Ramamurthi, 1993, Filter Collection in Aerosol Measurement: Principles Techniques and Applications, John Wiley and Sons, Inc. p. 179 - 205

Leu, M.T., R.S. Timonen, L.F. Keyser, Y.L Yung, 1995, Heterogeneous reactions of $HNO_3(g) + NaCl(s) \Rightarrow HCl(g) + NaNO_3(s)$ and N_2O_5 and $NaCl \Rightarrow ClNO_2(s)$. J. Phys. Chem., 99, 13,203 – 12,212

Libes, S. M., 1992, An Introduction to Marine Biogeochemistry, John Wiley & Sons, Inc. New York

Lipfert, F. W., 1994, Filter artifacts associated with particulate measurements: recent evidence and effects on statistical relationships: Atmospheric Environment, v. 28.

Litton, C. D., and M. Hertzberg, 1977, Principles of ionization smoke detection. Development of a new sensor for combustion-generated submicrometer particulates. United States Dept. of Interior, Bureau of Mines, Report No. 8242

Liu S. C., and Trainer M (1988) Responses of tropospheric ozone and odd hydrogen radicals to column ozone changes, J Atmos. Chem. 6:221-233

Loomis, M. B., 1992, Relativistic Electron Mass Determination, Durham, University of New Hampshire.

Lovejoy, E. R., and D. R. Hanson, 1995, Measurement of the kinetics of reactive uptake by submicron sulfuric acid particles: J. of Physical Chemistry, v. 99, p. 2080 - 2087.

Martens, C.S., J.J. Wesolowski, R.C. Harris, R. Kaifer, 1973, Chlorine loss from Puerto Rican and San Fancisco Bay area marine aerosols. J. Geophys. Res., 78, 8778-8791

McFarland, A. R., C. A. Oritz, M. E. Moore, R. E. DeOtte, and S. Somasundaram, 1989, A shrouded aerosol sampling probe: Environmental Science and Technology, v. 23, p. 1487-1492.

McInnes, L. M., D. S. Covert, P. K. Quinn, and M. S. Germani, 1994, Mearurements of chloride depletion and sulfur enrichment in individual sea-salt particles collected from the remote boundary layer: J. of Geophysical Research, v. 99, p. 8257 - 8268.

Milford, J. B., and C. I. Davidson, 1987, The sizes of particulate sulfate and nitrate in the atmopshere - a review: J. Air Pollution Control Association, v. 37, p. 125 - 133.

Monahan, E.C., 1986, The ocean as a source of atmospheric particles. In The Role of Air-Sea Exchange in Geochemical Cycling (edited by Buat-Menard P) pp. 126-163. Reidel, Dordrecht

Newell, R. E., Y.Zhu, E. V. Browell, W. G. Read, and J. W. Waters, 1996, Walker circulation and tropical upper tropospheric water vapor: J. Geophys. Res., v. 101, p. 1961-1974.

O'Dowd, C. D., M. H. Smith, I. E. Consterdine, and J. A. Lowe, 1996, Marine aerosol, sea-salt, and the marine sulphur cycle: a short review: Atmospheric Environment, v. 31, p. 73 - 80.

Pakkanen, T. A., 1996, Study of coarse particle nitrate aerosol: Atmos. Environ., v. 30, p. 2475 - 2482.

Papenbrock, T. H., F. Stuhl, K. P. Muller, and J. Rudolph, 1992, Measurement of gaseous HNO_3 over the Atlantic ocean: J. of Atmospheric Chemistry, v. 15, p. 369-379.

Penner, J. E., R. E. Dickinson, and C. A. Oneill, 1992, Effects of aerosol from biomass burning on the global radiation budget: Science, v. 256, p. 1432 - 1433.

Pham, M., J. F. Muller, G. P. Brasseur, C. Granier, and G. Megie, 1996, A 3D model study of the global sulfur cycle: Contributions of anthropogenic and biogenic sources: Atmos. Environ., v. 30, p. 1815 - 1822.

Posfai, M, J.R. Anderson, P. Buseck, H. Sievering, 1995, Compositional variations of sea-salt-mode aerosol particles from the North Atlantic, J. Geophys. Res., 100, D11

Quinn, P. K., S. F. Marshall, T. S. Bates, D. S. Covert, and V. N. Kapustin, 1995, Comparison of measured and calculated aerosol properties relevant to the direct radiative forcing of tropospheric sulfate aerosol on climate: J. of Geophysical Research, v. 100, p. 8977-8991.

Ravishankara, A. R., 1997, Heterogeneous and Multiphase Chemistry in the Troposphere: Science, v. 276, p. 1058 - 1065.

Ridley BA, Madronich S, Chatfield RB, Walega JG, Shetter RE, Carroll MA, and Montzka DD (1992) Measurements and model simulations of the photostationary state during MLOPEX: Implications for radical concentrations and ozone production and loss rates. J Geophys Res 97: 10375-10388

Reischl, G., W. John, and W. Devor, 1977, Uniform electrical charging of monodisperse aerosols: J. Aerosol Sci., v. 8, p. 55 - 65.

Richardson, C. B., R. L. Hightower, and A. L. Pigg, 1986, Optical measurement of the evaporation of sulfuric acid droplets: Applied Optics, v. 25, p. 1226-1229.

Ridley BA, Madronich S, Chatfield RB, Walega JG, Shetter RE, Carroll MA, and Montzka DD (1992) Measurements and model simulations of the photostationary state during MLOPEX: Implications for radical concentrations and ozone production and loss rates. J Geophys Res 97: 10375-10388

Rood, J., D. S. Covert, and T. V. Larson, 1987, Hygroscopic properties of atmospheric aerosols in Riverside, California: Tellus, v. 39B, p. 383 - 397.

Roscoe, H. K., and K. C. Clemitshaw, 1997, Measurement Techniques in Gas-Phase Tropospheric Chemistry: A Selective View of the Past, Present and Future: Science, v. 276, p. 1065 - 1072.

Rossi, M. J., F. F. Fenter, K. Tabor, F. Calzor, and L. Gutzwiller, 1996, Heterogeneous Reactions of Nitrogen Oxides (NO2, N2O5, HNO3, ClONO2) with surfaces representative of atmospheric aerosol, *in* P. Warneck, ed., Heterogeneous and Liquid-Phase Processes, Springer, p. 213 - 220.

Sakugawa, H., Kaplan, I.R., Tsai, W., Cohen, Y., 1990, Atmospheric hydrogen peroxide, Env. Sci. Technol., 24, 1452-1462

Sander, R., P.J. Crutzen, 1996, Model study indicating halogen activation and ozone destruction in polluted air masses transported to sea. J. Geophys. Res., 101, 9121-9138

Savoie, D. L., and J. M. Prospero, 1982, Particle size distribution of nitrate and sulfate in the marine atmosphere: Geophysical Research Letters, v. 9, p. 1207-1210.

Seinfeld, J.H., and S.N. Pandis, 1998, Atmospheric Chemistry and Physics: From Air Pollution to Climate Change, John Wiley & Sons, Inc., New York

Sievering, H., J. Boatman, J. Galloway, W. Keene, Y. Kim, M. Luria, and J. Ray, 1991, Heterogeneous sulfur conversion in sea-salt aerosol particles: The role of aerosol water content and size distribution: Atmospheric Environment, v. 25A, p. 1479 - 1487.

Sievering, H., J. Boatman, E. Gorman, Y. Kim, L. Anderson, G. Ennis, M. Luria, and S. Pandis, 1992, Removal of sulphur from the marine boundary layer by ozone oxidation in sea-salt aerosols: Nature, v. 360, p. 571 - 573.

Sievering, H., E. Gorman, T.Ley, A. Pszenny, M. Springer-Young, J. Boatman, Y.Kim, C. Nagamoto, and D. Wellman, 1995, Ozone oxidation of sulfur in sea-salt aerosol particles during the Azores Marine Aerosol and Gas Exchange experiment: J. of Geophysical Research, v. 100, p. 23075 - 23081.

Singh, H. B., M. Kanakidou, P. J. Crutzen, and D. J. Jacob, 1995, High concentrations and photochemical fate of oxygenated hydrocarbons in the global troposphere: Nature, v. 378, p. 50 - 54.

Singh, H. B., and J. F. Kasting, 1988, Chlorine-hydrocarbon photochemistry in the marine troposphere and lower stratosphere: J. Atmos. Chem., v. 7, p. 261 - 285.

Singh, H.B, Herlth, D., Koyler, R., Salas, L., Bradshaw, J.D., Sandholm, S.J., Davis, D.D., Crawford, J., Knodo, Y., Koike, M., Talbot, R., Gregory, G., Sachse, G., Browell, E., Blake, D.R., Rowland, F., Newall, R., Merill, J., Hiekes, B., Liu, S.C., Crutzen, P.J., Kanakidou,M., 1996, Journal of Geophysical Research, , 101, 1793.

Talbot, R. W., A. S. Vijgen, and R. C. Harriss, 1990, Measuring tropospheric HNO_3: Problems and prospects for nylon filter and mist chamber techniques: J. of Geophysical Research, v. 95, p. 7553 - 7561.

Tang, I. N., 1997, Thermodynamic and optical properties of mixed-salt aerosols of Atmospheric importance: J. of Geophysical Research, v. 102, p. 1883 - 1893.

Tabazadeh, A., M.Z. Jacobson, H.B. Singh, O.B. Toon, J.S. Lin, R.B. Chatfield, A.N. Thakur, R.W. Talbot, J.E. Dibb, 1998, Nitric acid scavenging by mineral and biomass burning aerosols, Geophys. Res Lett., 25, 4185-4188

Thakur, A.N., Signh, H.B., Mariani, P., Chen, Y., Wang, Y., Jacob, D.J., Brasseur, G., Muller, J., Lawerence, M., Atmospheric Environment, 1999, 33, 1403

Underwood, G.M., P. Li, C.R. Usher and V.H. Grassian, 2000, Determining accurate kinetic parameters of potentially important heterogeneous atmospheric reactions on solid particle surfaces using a Knudsen cell reactor, J. Phys Chem A, 104, 819-829, 2000a.

Van Doren, J. M., L. R. Watson, P. Davidovits, D. R. Worsnop, M. S. Zahniser, and C. E. Kolb, 1990, Temperature dependence of the uptake coefficients of HNO_3, HCl, N_2O_5 by water droplets: J. of Physical Chemistry, v. 94, p. 3265 - 3269.

Van de Hulst, H.C., 1981, Light Scattering by Small Particles, Dover Publications, New York

Van Duyne, R.P., Laser Excitation of Raman Scattering from Adsorbed Molecules on Electrode Surfaces, in Chemical and Biochemical Applications of Lasers, vol IV, C.B. Moore, ed., Academic Press, New York, 1979

Vogt, R., P. J. Crutzen, and R. Sander, 1996, A mechanism for halogen release from sea-salt aerosol in the remote marine boundary layer: Nature, v. 383, p. 327 - 330.

Vogt, R., C. Elliott, H. C. Allen, J. M. Laux, J. C. Hemminger, and B. J. Finlayson-Pitts, 1996, Some new laboratory approaches to studying tropospheric heterogeneous reactions: Atmospheric Environment, v. 30, p. 1729 - 1737.

Wang, Y., J. A. Logan, D. J. Jacob, 1998, Global simulation of tropospheric O3-NOx-hydrocarbon chemistry, 2. Model evaluation and global ozone budget, J. Geophys. Res., 102, 10.727-10,755

Warneck, P., 1988, Chemistry of the Natural Atmosphere, Int. Geophys. Series, vol. 41, Academic Press, Inc., New York

White, H.J., 1954, Industrial Electrostatic Precipitation., Addison Wesley, Reading MA

Wielicki, B., D. Cess, M. D. King, D. A. Randall, and E. F. Harrison, 1995, Mission to Planet Earth : Role of clouds and radiation in climate: Bulletin of the American Meteorological Society, v. 76, p. 2125-2153.

Williamson, C.F., J.P. Boujot, H Picard, 1996 : Tables of Range and Stopping Power of Chemical Elements for Charged Particles of Energy 0.5 to 500 MeV, CEQ-R_3042. Clearinghouse for Federal Scientific and Technical Information, Springfield, Virginia

Willeke,K, P.A. Baron, 1993, Aerosol Measurement: Principles Techniques and Applications, John Wiley and Sons, Inc.

Wilson, W. E., and P. C. Reist, 1994, A PC-based mie scattering program for theoretical investigations of the optical properties of atmospheric aerosols as a function of composition and relative humidity: Atmospheric Environment, v. 28, p. 803-809.

Woodcock, A. H., 1953, Salt nuclei in marine air as a function of altitude and wind force: J. Meteorol, v. 10, p. 362.

Worsnop, D. R., M. S. Zahniser, and C. E. Kolb, 1989, Temperature dependence of mass accommodation of SO2 and H2O2 on aqueous surfaces: J. of Physical Chemistry, v. 93, p. 1159 - 1172.

Wurzler, S., A. I. Flossmann, H. R. Pruppacher, and S. E. Schwartz, 1995, The scavenging of nitrate by clouds and precipitation: J. of Atmospheric Chemistry, v. 20, p. 259 - 280.

WMO (1991) Scientific Assessment of Ozone Depletion: 1991. World Meteorological Organization Global Ozone Research and Monitoring Project Report No 25, Geneva

Xiaohong, Y., Ming Fang, Chan, C., 2001, Experimental Study of the Sampling Artifact of Chloride Depletion from Collected Sea Salt Aerosols, *Environ. Sci. Technol.*, 35 (3), 600 –605

Yeh, H., 1993, *Electrical Techniques* from Aerosol Measurement: Principles, Techniques and Applications, John Wiley and Sons, Inc., New York

Yoshizumi, K., A. Hoshi, 1985, Size distributions of ammonium nitrate and sodium nitrate in atmospheric aerosols, Envir. Sci. Technology, 19, 258-261

APPENDIX

The following pages list MATLAB code as well as MathCAD worksheets that were used extensively during the course of analyzing data and performing calculations for this work.

```
% Program Charger : This routine uses a Euler - Cromer method to predict the
% trajectory of a micron sized latex sphere in a sinusoidally varying electric
% field.
%
%
%
        clear
        help charger
%
%
%
% specifiy some parameters about the particle
        radius = input('Particle radius (microns) ...');
        radius = radius*10^(-6);    % meters
        density = 1050;             % kg per cubic meter
        volume = (4/3)*pi*(radius)^3;
        mass = density*volume;
%
%
%
% specify some electrode voltage and geometry (volts and meters)
        phinot = input('Peak plate voltage (volts)...');
        frequency = input('AC voltage frequency (Hz)...');
%
%
%
%
% initialize some timing parameters and fill out the time array
        period = (2*pi)/frequency;
        tau = period / 500;
        cycles = 4;
        maxstep = round(period*cycles / tau);
        for i = 1: maxstep
                time(i) = (i-1)*tau;
        end
%
%
%
% fill out the Electric field vs time array
        Eamp = phinot * 100;        % will put efield in terms of volts per meter
        for i = 1:maxstep
                Efield(i) = 2*Eamp * cos( (time(i)/period)*2*pi );
        end
%
%
%
% initial velocities radial and downward velocities (meters / sec)
```

```
        velx(1) = 0;
%
%
% initial vertical postiion (meters - top and to side of electrode)
        posx(1) = 0;
%
%
% initial accelerations
        xaccel(1) = 0;
        xacceldrag(1) = 0;
        xaccelelec(1) = 0;
%
%
% calculate the Knudsen number for the particle
        lamda = 0.0665;
        Kn = 2*lamda / (2*radius*10^6);
%
%
% calculate the cunningham slip factor for a particle of this size
        rhogas = 1.192;
        chi = 1;
        alpha = 1.207;
        beta = 0.440;
        gamma = 0.596;
        Cc = 1 + Kn*(alpha+beta*exp(-1*gamma / Kn));
%
%
%
% calculate the saturation charge
        [charge] = sat(radius,phinot);
        charge = charge*(1);        % (electrons you know)
%
%
%
% ================start the main loop=============================
%
        for istep = 2:maxstep
%
%
% calculate the force and acceleration due to electric field
                Felec = charge*Efield(istep-1);
                xaccelelec(istep) = Felec / mass;
%
%
% calculate the force and acceleration on the particle due to drag
                eta = 1.833*10^(-5);
                velocity = velx(istep-1);
                Fdrag = (-1)*3*pi*eta*velocity*2*radius / Cc;
                xacceldrag(istep) = Fdrag / mass;
%
%
% update the acceleration vectors
                xaccel(istep) = xaccelelec(istep) + xacceldrag(istep);
%
%
% update the velocity vectors
```

```
                velx(istep) = velx(istep-1) + xaccel(istep)*tau;
%
%
% update the position  vectors (make sure the particles stay in the electrode)
                posx(istep) = posx(istep -1) + velx(istep)*tau;
%
%
%
        end
% ==========end the main loop==========
%
%
% plot out some cools stuff
        posx = posx * 100;
        amplitude = max(posx) - min(posx)
        subplot(2,1,1)
        plot(time,posx,'k.')
%
        subplot(2,1,2)
        plot(time,xaccel,'k', time,xaccelelec,'r', time,xacceldrag,'g')
%



function [qsat] = sat(radius,phinot)
% MATLAB function used to calculate the saturation charge on a particle
% of a given radius.  The theory of field charging is given by White et. al.
% The electric field units are in volts per meter in order to have the saturation
% charge come out in coulombs.
%
%
% find out the magnitude of the electric field
        Enot = 2*phinot * 100;     %volts per meter
%
%
%
% permitivity of free space
        etanot = 8.85*10^(-12);
%
%
% dielectric constant of latex ( 3*die / (die +2) )
        ksee = 1.681;
%
%
% calculate the saturation charge - in coulombs
        qsat = ( 4*pi*etanot*ksee*Enot*(radius)^2 );
        electrons = qsat / (1.6*10^(-19))
%
%
%
```

```
% program ccd
% quick routine to bin up a slice of a CCD image
%
        clear
        help ccd
%
%
% load in an image
        load source.255
        [numy numx] = size(source)
%
%
%
%
% initialize the strip vector
        for i = 1:numx
                sourcesum(i) = 0;
                backsum(i) = 0;
        end
%
%
% begin the summing
        for i = 1:numx
                for j = 1: 40
                        sourcesum(i) = sourcesum(i) + source(j,i);
                end
        end
%
%
%
%
% find the average superpixel value (subsum / # row)
        avg = sourcesum / 40;
%
%
% perform smoothing operations (using 3 point algorithm)
        smooth(1) = avg(1);
        smooth(2) = avg(2);
        smooth(159) = avg(159);
        smooth(160) = avg(160);
        for i = 3:158
                smooth(i)=(avg(i-2)+avg(i-1)+avg(i)+avg(i+1)+avg(i+2))/5;
        end
%
%
% plot out the sum vs pixel number
        pixel = 1:numx;
        plot(pixel,smooth,'k')
%
%
%
%look at the peaks with the crosshair program
crsshair
%
%
%
```

```
% Program to calculate the radius of an aerosol using the Mie Scattering System and Sytem calibration
%information
%clear everything
        clear
%
%
% create the correction factors for the distortion filter
% (based on empiracal data)
        for i = 1:160
                pixel(i) = i;
        end
        for i = 1:160
                corfac(i) = 33.86 - (0.412866*pixel(i)) +      (0.0028979*pixel(i)*pixel(i));
        corfac(i) = corfac(i) / 19.15874;
                corfac(i) = 1;
        end
%
%
%
% find the number of degrees per oscillation
        degperpix = 0.065;
        startpix = input('Start pixcel...');
        stoppix = input('End pixcel...');
        numcycle = input('Number of oscillations...');
        sum = 0;
        for i = startpix:stoppix
                sum = sum + (1/corfac(i));
        end
        degpercycle = (degperpix*(sum))/numcycle;
        xi = degpercycle;
%
%
% input the model data
        meas(1) = 24.9;
        meas(2) = 10.5;
        meas(3) = 7.05;
        meas(4) = 5.33;
        meas(5) = 4.27;
        meas(6) = 3.525;
        meas(7) = 3.00;
        meas(8) = 2.63;
        meas(9) = 2.34;
        meas(10) = 2.125;
        meas(11) = 1.922;
        meas(12) = 1.76;
        meas(13) = 1.627;
        meas(14) = 1.5120;
        meas(15) = 1.415;
        for i = 1:15
                rad(i) = i*1.0;
        end
%
%
% find the "nearest' three degree per cycle measurement, be careful near
% the first and last measurements
```

```
        dist = 1000;
        index = 1;
        for i = 1:15;
                workdist = abs(meas(i) - xi);
                if (workdist <= dist);
                        index = i;
                        dist = workdist;
                end
        end
        if (index == 1)
                index = 2;
        end
        if (index == 15)
                index = 14;
        end
%
%
%
% pass the nearest three measurements to the interpolation routine
        x(1) = meas(index - 1);
        x(2) = meas(index);
        x(3) = meas(index+1);
        y(1) = rad(index-1);
        y(2) = rad(index);
        y(3) = rad(index +1);
        yi = intrpf(xi,x,y);
        diameter = 2*yi
%
%
%
% plot some cool stuff
        plot(rad,meas,'r+', yi,xi,'k+')
        xlabel('Particle Radius - microns')
%
%
%
```

Worksheet to calculate the charge on a latex sphere injected tribologically into the trap. Followir equations from pg 35 in phase 1 proposal.

$V_{dc} := 10.42 \cdot volt$ Is the dc balance voltage

$r := 8.7 \cdot 10^{-6} \cdot m$ particle radius (see radius code)

$C_0 := 0.907$ Co is the levetation constant based on geometry

$g := 9.8 \cdot \frac{m}{sec^2}$ gravitational acceleration constant

$z_0 := 0.25 \cdot in$ radius of the trap

$v := \frac{4}{3} \cdot \pi \cdot r^3$ $v = 2.758 \times 10^{-9} cm^3$ calculated particle volume

$\rho := 1.05 \cdot \frac{gm}{cm^3}$ estimated particle density

$mass := \rho \cdot v$ $mass = 2.896 \times 10^{-9} gm$ particle mass

$q := \frac{mass \cdot g \cdot z_0}{C_0 \cdot V_{dc}}$ $q = 1.907 \times 10^{-14} coul$ $electron := 1.60 \cdot 10^{-19} \cdot coul$

$q = 119190\, electron$

$\frac{q}{mass} = 6.585 \times 10^{-6} \frac{coul}{gm}$ charge to mass ratio

Worksheet for the analysis of NaCl particles in the trap. First determine the charge on the particle estimating the density and volume of a fully hydrated NaCl / Water droplet in the trap.

$V_{dc} := 10.23 \cdot volt$ Is the dc balance voltage

$r := 10.5 \cdot 10^{-6} \cdot m$ particle radius (see radius code) $rerr := r \cdot 0.05$

$C_0 := 0.907$ Co is the levetation constant based on geometry $\frac{27.7}{2} = 13.85$

$g := 9.8 \cdot \frac{m}{sec^2}$ gravitational acceleration constant

$z_0 := 0.25 \cdot in$ radius of the trap

$v := \frac{4}{3} \cdot \pi \cdot r^3$ calculated particle volume $\rho := 1.05 \cdot \frac{gm}{cm^3}$ estimated particle density

$mass := \rho \cdot v$ $mass = 5.092 \times 10^{-9} gm$ particle mass

$mass = 5.092 \times 10^{-12} kg$

$q := \frac{mass \cdot g \cdot z_0}{C_0 \cdot V_{dc}}$ $q = 3.415 \times 10^{-14} coul$ $electron := 1.60 \cdot 10^{-19} \cdot coul$ $q = 213424\, electron$

With the assumption that the charge on the particle remains constant, what is the mass of the initial dry particle - all you need to know is the balance volatge of the initial (dry) particle

$V_{dry} := 5.06 \cdot volt$

$mass_{dry} := \frac{q \cdot C_0 \cdot V_{dry}}{g \cdot z_0}$ $picomole := 1 \cdot 10^{-12} \cdot mole$

$mass_{dry} = 2.518 \times 10^{-9} gm$

how many moles of NaCl does this represent?

$moles_{nacl} := \frac{mass_{dry}}{(22.9898 + 35.453) \cdot \frac{gm}{mole}}$ $moles_{nacl} = 43.091\, picomole$

what kind of "chlorine molarity" does this represent? $molerr_{nacl} := \frac{3 \cdot rerr}{r} \cdot moles_{nacl}$

$molarity := \frac{moles_{nacl}}{v}$ $molerr_{nacl} = 6.464\, picomole$

[redacted] this is the chlorine molarity,
expect the nitrate molarity to be the same plus a little bit more?

What is the radius of the dry salt particle?

$$\frac{43}{5} \cdot \frac{1}{2} = 4.3$$

$$\text{density\_salt} := 2.165 \cdot \frac{\text{gm}}{\text{cm}^3}$$

$$\text{dry\_volume} := \frac{\text{mass}_{\text{dry}}}{\text{density\_salt}}$$

$$\text{dry\_radius} := \left(\frac{3 \cdot \text{dry\_volume}}{4 \cdot \pi}\right)^{\frac{1}{3}}$$

$$\text{dry\_radius} = 6.524 \times 10^{-6}\,\text{m}$$

Sulfate / Peroxide / Ozone Prototype Model : This worksheet is used to determine the initial S(IV) concetration and pH of an aoersol based on the thermodynmamics of dissolved SO2 in water.

$ppbv := 1 \cdot 10^{-9}$ $\quad M := \frac{mole}{liter}$

set the mixing ratios of the trace gasess

$p_{so2} := 64 \cdot 10^{-9}$

$p_{o3} := 350 \cdot 10^{-9}$

set the Henry's law constants

$H_{so2} := 1.23$

$H_{o3} := 1.13 \cdot 10^{-2}$

set the dissociation constants

$k_w := 1.0 \cdot 10^{-14}$

$k_{s1} := 1.3 \cdot 10^{-2}$

$k_{s2} := 6.6 \cdot 10^{-8}$

Solve the electroneutrality equation to determine the H+ concentration

$a := 1$

$b := 0$

$c := \left(H_{so2} \cdot k_{s1} \cdot p_{so2} + k_w\right) \cdot -1$

$d := \left(H_{so2} \cdot k_{s1} \cdot k_{s2} \cdot p_{so2}\right) \cdot -2$

$$v := \begin{pmatrix} d \\ c \\ b \\ a \end{pmatrix} \qquad \text{polyroots}(v) = \begin{pmatrix} -3.192 \times 10^{-5} \\ -1.32 \times 10^{-7} \\ 3.206 \times 10^{-5} \end{pmatrix} \qquad \text{lola} := \text{polyroots}(v)$$

$$\text{lola}_{2,0} = 3.206 \times 10^{-5}$$

$H_{conc} := \text{lola}_{2,0}$

$H_{conc} = 3.206 \times 10^{-5}$

$pH := -1 \cdot \log(\text{lola}_{2,0})$

[redacted] this is the initial pH of the droplet (supposedly)

Find the "initial" concentration of S(IV) in the droplet

$$SIV_{conc} := H_{so2} \cdot p_{so2} \cdot \left(1 + \frac{k_{s1}}{H_{conc}} + \frac{k_{s1} \cdot k_{s2}}{H_{conc}^{2}}\right)$$

$SIV_{conc} = 3.207 \times 10^{-5}$ moles per liter

Model Prototype of nitric acid and ammonia mixture...

$M := \frac{mole}{liter}$

$k_w := 1.0 \cdot 10^{-14} \cdot M^2$ $k_{a1} := 1.7 \cdot 10^{-5} \cdot M$ $k_{n1} := 15.4 \cdot M$ dissociation constants

$H_{nh3} := 62 \cdot \frac{M}{atm}$ $H_{hno3} := 2.1 \cdot 10^{5} \cdot \frac{M}{atm}$ henrys' law constants

$i := 1 .. 100$

array dimensions

$j := 1 .. 3$

$phno3_i := i \cdot 10^{-9} \cdot atm$ partial pressure of nitric acid

$pnh3_1 := 0 \cdot 10^{-9} \cdot atm$ partial pressure of ammonia

$pnh3_2 := 1 \cdot 10^{-9} \cdot atm$

$pnh3_3 := 10 \cdot 10^{-9} \cdot atm$

determine what the equilibrium hydrogen ion concentration is

$$H_{i,j} := \sqrt{\frac{k_w + H_{hno3} \cdot k_{n1} \cdot phno3_i}{\left(1 + \frac{H_{nh3} \cdot k_{a1} \cdot pnh3_j}{k_w}\right)}}$$

$pH_{i,j} := -\log\left(\frac{H_{i,j}}{M}\right)$ $pH_{100,1} = 0.245$ $pH_{100,2} = 1.259$ $pH_{100,3} = 1.757$

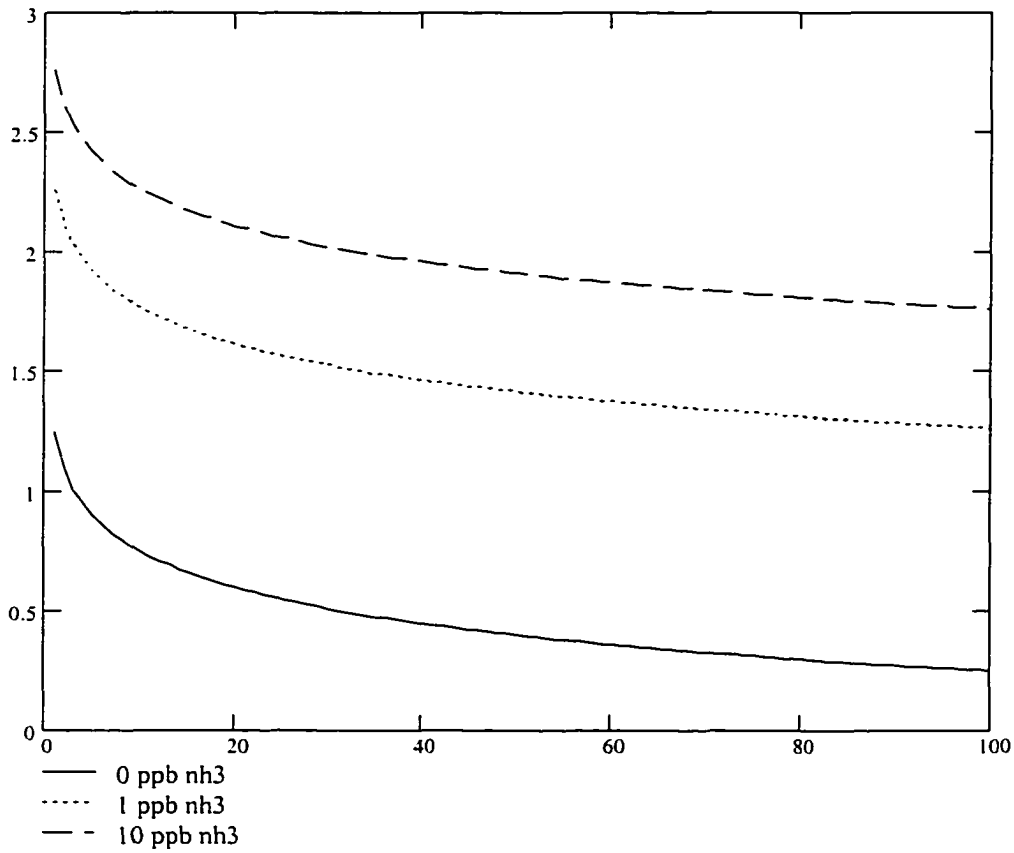

determine what the total amounts of nitrate and ammonia are in the droplet...

$$nh3total_{i,j} := H_{nh3} \cdot pnh3_j \cdot \left(1 + \frac{k_{a1} \cdot H_{i,j}}{k_w}\right)$$

$nh3total_{0,1} = 0\,M$

$nh3total_{0,2} = 1.838\,M$

$nh3total_{0,3} = 5.836\,M$

$$hno3total_{i,j} := H_{hno3} \cdot phno3_i \cdot \left(1 + \frac{k_{n1}}{H_{i,j}}\right)$$

$hno3total_{0,1} = 0.182\,M$

$hno3total_{0,2} = 1.857\,M$

$hno3total_{0,3} = 5.843\,M$

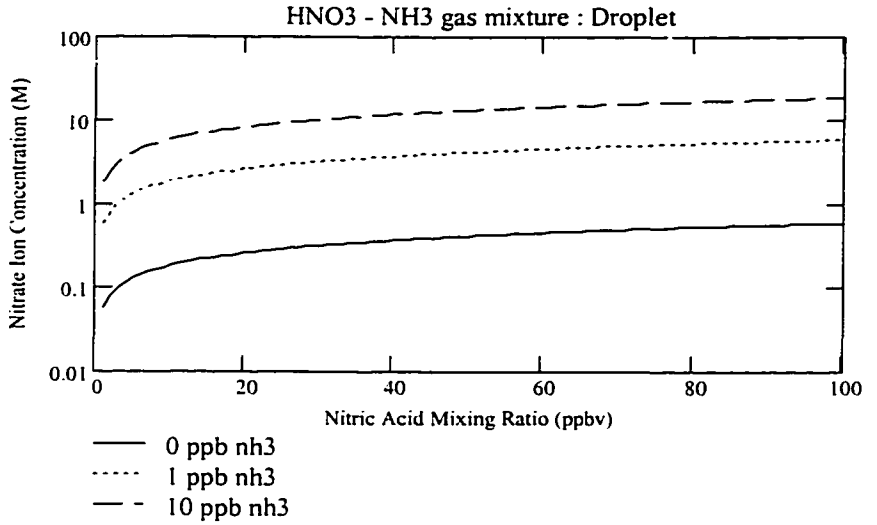

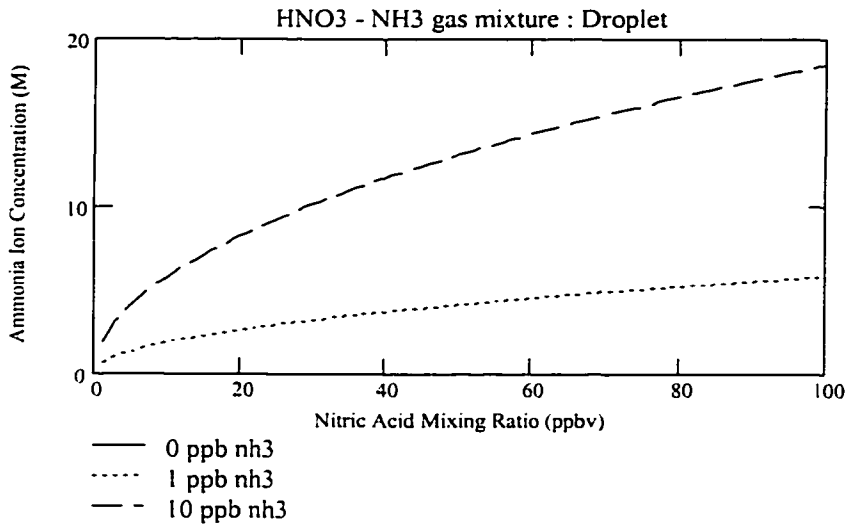

worksheet to determine the mixing ratio of SO2 and O3 in the trap subject to saturated air flow (wate

$P := 1 \cdot atm \quad T := 298 \cdot K \quad R := 8.314510 \cdot \frac{joule}{mole \cdot K} \quad ppbv := 10^{-9}$

$frsat := 82.5 \cdot \frac{cm^3}{min} \quad frso2 := 4.3 \cdot \frac{cm^3}{min} \quad frO3 := 10.2 \cdot \frac{cm^3}{min}$ the flow rates

$mr\_SO2\_tank := 1.2 \cdot 10^{-6} \quad mr\_O3\_gen := 500 \cdot 10^{-9}$

$moles\_air := \frac{P \cdot frsat}{R \cdot T} \quad moles\_air = 3.374 \times 10^{-3} \frac{mole}{min}$

$moles\_SO2 := \frac{P \cdot frso2}{R \cdot T} \cdot mr\_SO2\_tank \quad moles\_SO2 = 2.11 \times 10^{-10} \frac{mole}{min}$

$mr\_SO2\_trap := \frac{moles\_SO2}{moles\_air}$

[redacted]

$moles\_O3 := \frac{P \cdot frO3}{R \cdot T} \cdot mr\_O3\_gen \quad moles\_O3 = 2.086 \times 10^{-10} \frac{mole}{min}$

$mr\_O3\_trap := \frac{moles\_O3}{moles\_air}$

$mr\_O3\_trap = 62\,ppbv$

$RH := \frac{0.93 \cdot frsat}{frsat + frso2 + frO3}$

[redacted]

Calculation of latex and water droplet saturation charge based on White theory of aerosol charging. T following calculation is for field charging only in the limit that time for charging approaches infinity.

$\varepsilon_{water} := 78$

$\varepsilon_{latex} := 2.55$

$e := 4.8 \cdot 10^{-10}$

$i := 0..49$

$dp_i := (i + 1)$

$E := 1.667$

$$nwater_i := \frac{3 \cdot \varepsilon_{water}}{2 + \varepsilon_{water}} \cdot E \cdot \frac{\left(dp_i \cdot 1 \cdot 10^{-4}\right)^2}{4 \cdot e} \qquad nlatex_i := \frac{3 \cdot \varepsilon_{latex}}{2 + \varepsilon_{latex}} \cdot E \cdot \frac{\left(dp_i \cdot 1 \cdot 10^{-4}\right)^2}{4 \cdot e}$$

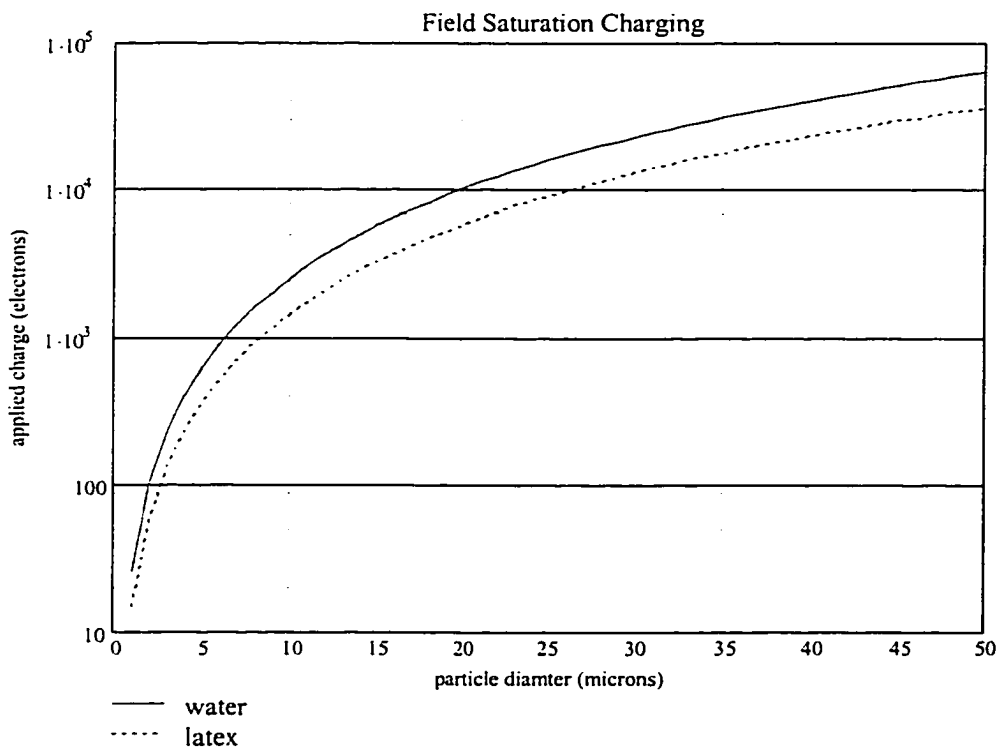

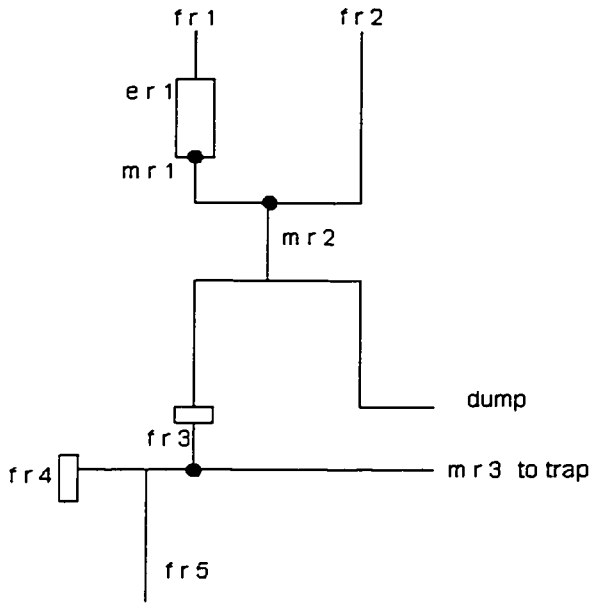

Worksheet to determine mixing ratio of nitric acid in the trap chamber based flow rates and perm tube emission rates - see diagram

$fr1 := 150 \cdot \frac{cm^3}{min}$ perm chamber flow

$fr2 := 00 \cdot \frac{cm^3}{min}$ dilution flow

$fr3 := 4.3 \cdot \frac{cm^3}{min}$ choke flow

$fr4 := 67.0 \cdot \frac{cm^3}{min}$ humidity sat flow

$fr5 := 00 \cdot \frac{cm^3}{min}$ humidity dry flov

$P := 1 \cdot atm$

$T := 298 \cdot K$ some gas stuff

$R := 8.314510 \cdot \frac{joule}{mole \cdot K}$

Determine what mixing ratio 1 (mr1) is...

$er1 := 3.679 \cdot 10^{-9} \cdot \frac{mole}{min}$ emission rate of perm tube : from oven calibration

$$mr1 := \frac{er1}{\left(\frac{P \cdot fr1}{R \cdot T}\right)}$$

$mr1 = 5.998 \times 10^{-7}$ meaning the mixing ratio of nitric acid flowing out of the permeation chamb is on the order of parts per million (based on 100 cm3 / min chamber flow)

Calculate mixing ratio 2 (mr2) ...

$$mr2 := \frac{er1}{\left[\frac{P \cdot (fr1 + fr2)}{R \cdot T}\right]}$$

$mr2 = 599.756\,10^{-9}$

Calculate mxing ratio 3 (mr3) ...

$$n3_{air} := \frac{P \cdot fr3}{R \cdot T}$$

$$n3_{air} = 1.758 \times 10^{-4} \frac{mole}{min}$$

$n3_{hno3} := n3_{air} \cdot mr2$

$$n3_{hno3} = 1.055 \times 10^{-10} \frac{mole}{min}$$

$$ntrap_{air} := \frac{P \cdot (fr3 + fr4 + fr5)}{R \cdot T}$$

$$ntrap_{air} = 2.916 \times 10^{-3} \frac{mole}{min}$$

$$mrtrap := \frac{n3_{hno3}}{ntrap_{air}}$$

$mrtrap = 36.17\,10^{-9}$

$ppb := mrtrap \cdot 10^{9}$

$ppb = 36.17$

Determine what the relative humidity in the trap chamber is ...

$$rh := \frac{0.93 \cdot fr4}{(fr4 + fr3 + fr5)}$$

$rh = 87\%$